Dissertation

Second-Harmonic Phonon Spectroscopy Using an Infrared Free-Electron Laser

Im

Fachbereich Physik
der Freien Universität Berlin

eingereichte Dissertation zur Erlangung des akademischen Grades
Doktor der Naturwissenschaften
(Dr. rer. nat.)
von

Christopher J. Winta

Berlin, Oktober 2020

Erstgutachter:

Prof. Dr. Martin Wolf
Fritz-Haber-Institut der Max-Planck-Gesellschaft
Abteilung Physikalische Chemie

Zweitgutachter:

Prof. Dr. Wolfgang Kuch
Freie Universität Berlin
Fachbereich Physik

Arbeitsgruppenleiter:

Dr. Alexander Paarmann
Fritz-Haber-Institut der Max-Planck-Gesellschaft
Abteilung Physikalische Chemie – Lattice Dynamics Group

Tag der Disputation: **17. Dezember 2020**

FRITZ-HABER-INSTITUT
MAX-PLANCK-GESELLSCHAFT

This work has been performed in the Lattice Dynamics Group
at the Department of Physical Chemistry
at the Fritz Haber Institute of the Max Planck Society.

Abstract

Nonlinear optical spectroscopy has emerged as a powerful tool for the investigation of crystalline solids. Compared to linear approaches, it offers additional experimental degrees of freedom which grant access to the sample's symmetry properties and can provide unique insight into its crystallographic and electronic structure. Moreover, owing to their higher-order field dependence, nonlinear techniques often feature improved contrast and sensitivity. These qualities are particularly useful in the infrared (IR) spectral region as it contains optical phonon resonances which carry symmetry information themselves and play a key role in determining a material's thermal, IR optical, and phase transition properties.

Among nonlinear optical techniques, second-harmonic generation (SHG) takes on a prominent role as the simplest even-order process and, while widely employed in the visible, has so far not been fully exploited in the IR—mainly due to the scarcity of suitable laser sources. With access to an IR free-electron laser (FEL), however, it becomes feasible to employ IR SHG as a phonon spectroscopy.

This work explores the potential of second-harmonic phonon spectroscopy as an alternative to more established even-order techniques. To this end, a comprehensive IR SHG study of the well-known model system α-quartz is performed, presenting the technique as a highly sensitive tool to study optical phonons in noncentrosymmetric polar crystals. Through these vibrational resonances, IR SHG can also aptly probe and characterize symmetry changes in a material which is demonstrated in a temperature-dependent study of quartz's α–β phase transition. The implementation of a cryogenic IR SHG setup extends the temperature range of second-harmonic phonon spectroscopy and enables phase transition studies at low temperatures where it also benefits from decreased phonon damping rates.

Further, second-harmonic phonon spectroscopy was successfully employed in the characterization of the unique phonon modes emerging in atomic-scale superlattices which cause a distinct dielectric response, highly suitable for nanophotonic device applications.

An attempt to exploit the technique's sensitivity to structural phase transitions in multiferroic thin films, revealed fundamental limitations of IR SHG posed by the relatively large IR FEL spot sizes and low sensitivity of available IR detectors. A proof-of-principle FEL-based IR-visible sum-frequency generation experiment shows how these limitations can be lifted while maintaining nonlinear optical and IR-resonant capabilities.

Overall, this work comprehensively explores the potential of IR SHG as a phonon spectroscopy, showcasing its unique capabilities and identifying its limitations. Perspectives are presented on how to further develop FEL-based nonlinear optical approaches to which the present work constitutes important groundwork.

Deutsche Kurzfassung

Die nichtlineare optische Spektroskopie stellt ein mächtiges Werkzeug zur Untersuchung kristalliner Festkörper dar. Ihre zusätzlichen experimentellen Freiheitsgrade im Vergleich zu linearen Ansätzen gewähren Zugriff auf Symmetrieeigenschaften und geben damit einen tiefen Einblick in die kristallographische und elektronische Struktur der Probe. Aufgrund ihrer starken Feldabhängigkeit haben nichtlineare Techniken außerdem oft erhöhte Sensitivität. Diese Eigenschaften sind besonders im infraroten (IR) Spektralbereich nützlich, da dort optische Phononenresonanzen liegen, die ihrerseits Symmetrieinformationen enthalten und entscheidend für die thermischen, IR-optischen und Phasenübergangseigenschaften eines Materials sind.

Als einfachstem nichtlinearem Prozess gerader Ordnung kommt der Frequenzverdopplung (SHG) eine besondere Rolle zu. Obwohl sie im sichtbaren Spektralbereich weit verbreitet ist, wurde sie im IR bisher nicht vollständig erforscht, was hauptsächlich auf den Mangel geeigneter Laserquellen zurückzuführen ist. Mithilfe eines IR Freie-Elektronen-Lasers (FELs) ist es jedoch möglich, IR-SHG als Phononenspektroskopie anzuwenden.

In dieser Arbeit wird das Potential der SHG-Phononenspektroskopie als Alternative zu etablierten Techniken gerader Ordnung untersucht. Dazu wird eine umfassende IR-SHG-Studie des bekannten Modellsystems α-Quarz durchgeführt, die die Technik als hochempfindliche Methode zur Untersuchung optischer Phononen in nichtzentrosymmetrischen polaren Kristallen präsentiert. Darüber hinaus ist IR-SHG gut zur Erfassung und Charakterisierung von Symmetrieänderungen anhand von Schwingungsresonanzen geeignet, was in einer temperaturabhängigen Studie des α-β-Phasenübergangs von Quarz gezeigt wird. Die Realisierung eines kryogenen IR-SHG-Aufbaus erweitert den Temperaturbereich der SHG-Phononenspektroskopie und erlaubt somit Tieftemperatur-Phasenübergangsstudien, wo sie zudem von verringerter Phononendämpfung profitiert.

Ferner wurde SHG-Phononenspektroskopie erfolgreich zur Charakterisierung hybrider Phononenmoden in Heterostrukturen auf Atomskala eingesetzt. Diese hybriden Moden rufen eine spezifische dielektrische Respons hervor, die für nanophotonische Bauelemente von großem Interesse ist.

Ein Experiment zur Untersuchung von Phasenübergängen in multiferroischen Dünnfilmen offenbarte grundlegende Limitierungen von IR-SHG, die auf die relativ großen IR-Fokusgrößen und die geringe Sensitivität aktueller IR-Detektoren zurückzuführen sind. Eine Machbarkeitsstudie zur FEL-basierten IR-sichtbaren Summenfrequenzerzeugung zeigt, wie diese Limitierungen überwunden und nichtlineare sowie IR-resonante Eigenschaften beibehalten werden können.

Diese Arbeit stellt eine umfassende Untersuchung über das Potential von IR SHG als Phononenspektroskopie dar und zeigt ihre Vorteile und Einschränkungen auf. Es werden darüber hinaus Perspektiven skizziert, wie FEL-basierte nichtlineare optische Ansätze weiterentwickelt werden können, für die diese Arbeit eine wichtige Grundlage darstellt.

Table of Contents

Chapter 1.

Introduction

The year of writing this thesis, 2020, marks the 60th anniversary of the invention of the laser—one of the most important landmark discoveries in modern science. These coherent light sources paved the way for a plethora of technological and scientific advancements which are now an integral part of everyday life. In the realm of fundamental research, their unprecedented light intensities famously enabled the study of nonlinear light-matter interactions, a development from which the condensed matter branch of physics, but also neighboring fields such as materials science and surface chemistry benefited greatly.

Especially the emergence of lasers covering infrared (IR) and terahertz wavelengths spurred condensed matter research as the characteristic vibrational modes of molecules, clusters, and solids fall into this spectral range. It is thus often referred to as the molecular fingerprint region. For crystalline solids, for instance, collective lattice vibrations, so-called phonons, play a central role in shaping their thermal, IR optical as well as phase transition properties and are therefore of vital interest.

For the study of vibrational modes, the qualities of nonlinear optical techniques can be immensely useful. Their enhanced field dependence as well as inherent sensitivity to symmetry can provide valuable information in characterizing the fundamental vibrational properties of the studied material itself, but also in investigating the underlying principles of light-matter interactions. Here, the unique properties of IR free-electron lasers (FELs) open up possibilities inaccessible by any other coherent light source: Their broad wavelength tunability and narrow bandwidth make them excellent spectroscopic tools while their high peak power is extremely well-suited for the employment of nonlinear optical approaches.

This work focuses on the exploration of FEL-based nonlinear optical techniques in the mid- to far-IR spectral region for the investigation of polar dielectrics. In particular, second-harmonic generation (SHG)—despite being well-studied and widely applied in the visible range—has so far not been fully explored in the IR, mostly due to the scarcity of adequate IR laser sources. Having access to the FHI FEL, however, employing IR SHG as a phonon spectroscopy becomes feasible and could even pose a viable alternative or complement to already established

techniques, such as Raman scattering or vibrational sum-frequency generation (SFG) spectroscopy. In this work, the capabilities of second-harmonic phonon spectroscopy are assessed in a comprehensive study of a well-known model system before it is applied to study material systems with a high potential for technological applications: nanophotonic metamaterials and multiferroic films.

The field of nanophotonics, for instance, focuses on the confinement of light to subdiffractional length scales, circumventing Abbe's fundamental limit and thereby enabling novel functionalities like super-resolution imaging or photonic circuitry. One particularly promising avenue towards these technologies lies in the coupling of IR light to lattice vibrational modes. The resulting quasiparticle— the phonon polariton—has recently attracted considerable research interest due to its intriguing physics and high potential for technological applications.

Multiferroics, on the other hand, exhibit two or more ferroic orders, e.g., ferromagnetism and ferroelectricity, in one material. Individually, these material properties are already widely used in data storage devices as well as in sensors and actuators. Combining multiple ferroic orders in a single phase, however, opens up technological opportunities for multifunctional, miniaturized, or more energy-efficient devices. Here, the underlying symmetries which vibrational modes are highly sensitive to, play a crucial role in determining their functionalities. In this sense, the present work positions itself at the intersection between the development of novel nonlinear optical approaches with an IR FEL and the investigation of highly relevant materials in today's research landscape.

In order to provide the necessary background, this introductory chapter (Ch. 1) is followed by a brief historical and conceptual overview of second-order nonlinear phenomena and techniques (Ch. 2). Here, three prominent studies are presented, each highlighting a specific aspect of nonlinear optical spectroscopy and the unique insights it can provide. Moreover, two specific examples of nonlinear IR spectroscopy are shown which are of particular relevance to the present work.

In Ch. 3, a theoretical framework for the description of nonlinear light-matter interactions is established with a particular focus on second-order effects, described by means of the second-order nonlinear susceptibility tensor, $\chi^{(2)}$. Most nonlinear techniques, however, are also strongly affected by *linear* effects. For this reason, Sec. 3.2 is dedicated to the description of the linear dielectric function, $\varepsilon(\omega)$, and specifically to its dispersive behavior at and around phonon resonances in the IR spectral region. In anisotropic materials, this resonant behavior can give rise to hyperbolicity, a currently very actively investigated phenomenon in the field of nanophotonics which is also discussed in this section. Lastly, the IR resonant behavior in second-order nonlinearities is described in Sec. 3.3. Here, the

involvement of anharmonic lattice parameters is explicitly discussed as they grant quantitative access to phonon-phonon interactions.

The experimental realization of spectroscopic ɪʀ sʜɢ as well as ɪʀ-visible sꜰɢ is described in Ch. 4, starting with the working principle of ꜰᴇʟs as well as the specifics of the facility used in this work, the ꜰʜɪ ꜰᴇʟ (Sec. 4.1). Secs. 4.2 and 4.3 deal with the experimental setups themselves. Lastly, technical details on sample temperature control for both, high- and low-temperature measurements are given, facilitating phase transition studies.

In Ch. 5, a comprehensive ɪʀ sʜɢ study of the model oxide α-quartz is presented. This first demonstration of second-harmonic phonon spectroscopy in a multimode system comprises a thorough analysis of ɪʀ sʜɢ spectra and azimuthal dependencies at room temperature as well as a study of quartz's α–β phase transition and its signatures in the temperature-dependent ɪʀ second-harmonic response. Moreover, sʜɢ spectra have been obtained at cryogenic temperatures, showcasing the benefits, but also technical limitations of low-temperature second-harmonic phonon spectroscopy. For an accurate analysis of the low-temperature spectra, the ɪʀ dielectric function of α-quartz between 1.2 K and 200 K was determined using ɪʀ reflectance spectroscopy. Notably, its low-temperature ɪʀ dielectric function has not been published in the literature prior to this work, but revealed remarkably small damping rates in α-quartz's hyperbolic bands, presenting it as an attractive material system for nanophotonic applications.

The aspect of hyperbolicity is again picked up in Ch. 6 where second-harmonic phonon spectroscopy is employed for the characterization of a novel nanophotonic metamerial. These so-called crystalline hybrids are composed of atomically thin layers of standard semiconductor materials and exhibit unique vibrational properties through the emergence of *hybrid* phonon modes. Those are aptly characterized using ɪʀ sʜɢ and exhibit a strong dependence on the semiconductors' layer thicknesses, resulting in a tunable dielectric response and pronounced hyperbolic bands. Overall, crystalline hybrids are presented as a versatile platform for engineered nanophotonic metamaterials.

Attempting to exploit the intrinsic symmetry sensitivity of ɪʀ sʜɢ, Ch. 7 presents a study of structural phase transitions in multiferroic thin films. These experiments, however, reveal a fundamental disadvantage of second-harmonic phonon spectroscopy as an all-ɪʀ technique, namely the relatively large laser spot sizes which become a limiting factor when investigating sub-micrometer structures, such as multiferroic domains. To overcome this limitation, Ch. 8 discusses a proof-of-principle ꜰᴇʟ-based ɪʀ-visible sꜰɢ generation experiment. Here, it is the visible component limiting the spatial resolution while the ɪʀ-resonant behavior is maintained. Lastly, an outlook towards future ɪʀ-visible sꜰɢ experiments is given, including an imaging microscopy approach.

Chapter 2.

Second-Order Nonlinear Optics
Concept

> "Physics would be dull and life most unfulfilling if all physical phenomena around us were linear. Fortunately, we are living in a nonlinear world. While linearization beautifies physics, nonlinearity provides excitement in physics."
>
> Yuen-Ron Shen, *The Principles of Nonlinear Optics*

This introductory chapter discusses the concepts and ideas behind nonlinear spectroscopy on a fundamental level. This includes a brief history of the field of nonlinear optics as well as examples of how spectroscopists harness its capabilities in different areas of scientific research today. In order to put the present work into its scientific context, an emphasis is put on second-order processes which—as the lowest-order nonlinearities—take on a prominent role in nonlinear spectroscopy due to their relative simplicity and useful symmetry properties. Exploiting these features is a central aspect of the research presented in this thesis.

2.1. A Brief Introduction to Nonlinear Optics

Spectroscopy is the study of the interaction between light and matter. Under low-light conditions, such interactions scale linearly with intensity. One macroscopic physical quantity essential to light-matter interaction is the electric polarization induced in the medium, $\mathbf{P}$, which in linear optics is assumed to be proportional to the electric field strength of the applied light, $\mathbf{E}$ [1]:

$$\mathbf{P} = \varepsilon_0 \chi \mathbf{E}, \tag{2.1.1}$$

where ε_0 is the free-space permittivity and χ the medium's electric susceptibility. As light intensity increases, however, a plethora of new optical phenomena arise which no longer depend linearly on the intensity of light. These *nonlinear* optical effects—caused by the interplay of *intense* light with matter—form the basis of nonlinear spectroscopy.
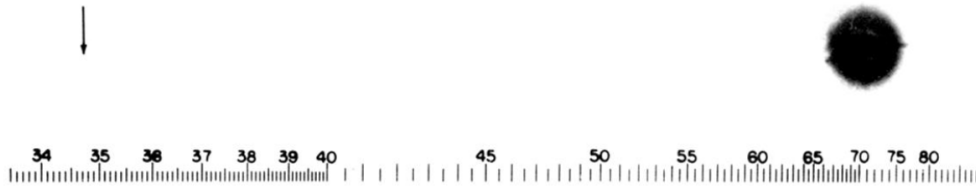
FIG. 1. A direct reproduction of the first plate in which there was an indication of second harmonic. The wavelength scale is in units of 100 A. The arrow at 3472 A indicates the small but dense image produced by the second harmonic. The image of the primary beam at 6943 A is very large due to halation.

Figure 2.1. First demonstration of optical second-harmonic generation. In 1961, Franken et al. let a ruby laser beam at 6942 Å propagate through a quartz crystal and observed ultraviolet radiation at 3471 Å [4]. In the original publication, however, no dot at the second-harmonic frequency was visible as it was erased by a journal technician who mistook it for a dust spot [10]. Reproduced from Ref. 4.

In 1960, Theodore H. Maiman demonstrated the first working laser [2] (based on theoretical groundwork laid out by Arthur L. Schawlow and Charles H. Townes two years earlier [3]) and thereby provided a light source of unprecedented intensity, triggering a series of landmark discoveries: In 1961, Peter A. Franken et al. famously reported the first optical SHG in quartz (see Fig. 2.1) [4], giving birth to the field of nonlinear optics. Shortly after—within less than two years—first demonstrations of optical SFG [5], third-harmonic generation [6], optical rectification [7], and difference-frequency generation [8, 9] followed.

These newly discovered nonlinear phenomena could no longer be described by the linear nature of Eq. 2.1.1 and required an adjustment in form of a power series expansion which allowed higher-order momenta of the electric field, **E**, to be taken into account [11, 12]:

$$\mathbf{P} = \varepsilon_0 \left(\chi^{(1)} \cdot \mathbf{E} + \chi^{(2)} : \mathbf{EE} + \chi^{(3)} : \mathbf{EEE} + \cdots \right). \tag{2.1.2}$$

Here, $\chi^{(n)}$ denotes the nth-order electric susceptibility and is a $(n + 1)$th order tensor. The essence of nonlinear optics is well captured by the tensorial character of $\chi^{(n)}$ as it represents the involvement of multiple light fields for $n \geq 2$ and reflects symmetry properties of the nonlinear medium. This enables nonlinear processes to reveal additional information about the medium's electronic structure, inaccessible by means of linear optics.

Early applications of nonlinear optics include frequency-doubling, mode-locking [13], and Q-switching [14] which fueled the development of tunable and pulsed narrow-linewidth lasers in the 1970s [15]. This, in turn, provided spectroscopists with the necessary tools to benefit from the possibilities that nonlinear optics offers to various scientific disciplines, including physics, chemistry, biology, and material science.

2.2. Second-Order Microscopy and Spectroscopy

Today's scientific landscape exhibits a wide range of highly relevant use cases for nonlinear optical techniques. Prominent examples include second-harmonic imaging of biological tissue [16–18], surface-specific IR microscopy using SFG [19, 20] as well as the generation of terahertz transients—a process based on optical rectification [21]. In the following, we shall showcase three example studies which take advantage of key concepts in nonlinear optics, such as symmetry sensitivity and resonant enhancement.
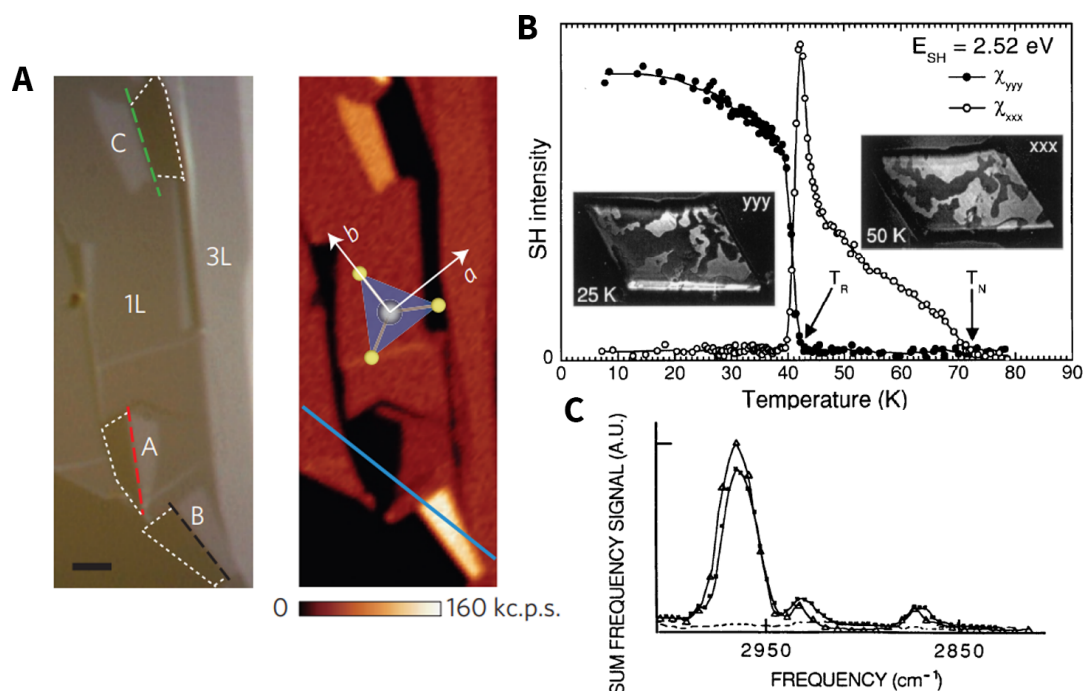
Figure 2.2. Second-order microscopy and spectroscopy. A: A whitelight (left) and SHG microscopy image (right) of a MoS_2 sample exhibiting monolayers (1L), trilayers (3L), and folded bilayers (A, B, C). The SHG microscopy image can distinguish between the different stacking orders associated with the three folding orientations A, B, and C. **B:** Temperature-dependence of two $\chi^{(2)}$ tensor elements and topography of the antiferromagnetic spin structures (insets), indicating phase transitions at T_N and T_R. **C:** IR-visible SFG spectra of a CCl_4/OTS/quartz (squares), a hexadecane/OTS/quartz (triangles), and a bare hexadecane/quartz interface (dashed line), showcasing surface-specific SFG vibrational spectroscopy. Reproduced from Refs. 22–24, respectively.

In their 2014 study, Jiang et al. investigated molybdenum disulfide (MoS_2) bilayers by folding exfoliated monolayers in an origami-like fashion [22]. Depending on the folding orientation, the MoS_2 bilayers take on various stacking orders which—due to their different symmetry structures—cause contrasting nonlinear responses as revealed by optical SHG microscopy (Fig. 2.2A). Here, the authors exploited the second-order technique's intrinsic sensitivity to symmetry

to monitor the folded bilayers' various stacking orders which, interestingly, lead to strongly modified and tunable band structures [22].

In general, the behavior and performance of functional materials are often closely linked to their symmetry properties, promoting second-order techniques to be valuable tools to assess their properties and capabilities. In this context, Fiebig et al. famously introduced visible SHG microscopy as a potent tool to study complex magnetic structures using hexagonal manganites as an example [23]. These compounds enter an antiferromagnetic phase at their magnetic ordering (Néel) temperature, T_N, which is always accompanied by a violation of time-reversal symmetry, leading to a nonzero second-order susceptibility, $\chi^{(2)}$. Utilizing SHG microscopy, Fiebig et al. were able to determine the Néel temperature of HoMnO$_3$ to be $T_N = 72\,K$ due to an onset of the integrated SHG signal as shown in Fig. 2.2B. Moreover, by purposefully choosing an appropriate measurement geometry, the authors could infer the specific spin structure in HoMnO$_3$'s antiferromagnetic phase [23]. In doing so, they also revealed a second phase transition at $T_R = 41\,K$, involving a spin reorientation—as indicated by a change in the contributing $\chi^{(2)}$ tensor element—as well as a topographical change in the antiferromagnetic domain structure (see insets of Fig. 2.2B).

Moreover, second-order optical techniques' sensitivity to symmetry—and in particular to symmetry *breaking*—allows to selectively interrogate surfaces and interfaces where the inversion symmetry is inevitably violated. This has been demonstrated by the group of Yuen-Ron Shen who employed IR-visible SFG vibrational spectroscopy to investigate octadecyltrichlorosilane (OTS) surfactant monolayers at buried interfaces [24].[1] Fig. 2.2C shows the vibrational SFG spectra of CCl$_4$/OTS/(amorphous) quartz, hexadecane/OTS/quartz as well as bare hexadecane/quartz (without an OTS layer) interfaces. Despite hexadecane's strong bulk absorption in this spectral range, the SFG spectra at the hexadecane and CCl$_4$ interfaces appear nearly identical. This indicates that, in fact, only the interface is probed and that the bulk contribution of hexadecane is negligible. Additionally, SFG from the bare hexadecane/quartz interface without an OTS layer has been measured, showing no significant spectral features. These results confirm that the SFG signal originates exclusively from the OTS monolayer and demonstrates the technique's surface specificity.

Notably, this demonstration triggered a great number of follow-up studies, making IR-visible SFG one of the most well-established surface spectroscopies to date with a wide scope of applications. These include, for instance, probing of liquid/liquid interfaces [27], chemical imaging [28], following ultrafast vibrational dynamics at aqueous interfaces [29] as well as surface phonon probes in

---

1 The SFG study of OTS was preceded by two studies on C–H stretch modes in methanol and pentadecanoic acid, also performed by the Shen group [25, 26]. These studies were, in fact, the *first* demonstrations of SFG vibrational spectroscopy.

polar dielectrics [30, 31]. Furthermore, second-order techniques also present a powerful tool for studying the *bulk* properties in polar dielectrics. Thereto, the following section highlights two important examples, highly relevant to the work presented in this thesis.

2.3. Infrared Second-Order Spectroscopy of Polar Dielectrics

Here, two case studies of IR second-order nonlinear spectroscopy are presented. They generally aim to acknowledge the importance to their respective fields, but also constitute important pioneer work for this thesis.

Sum-Frequency Phonon Spectroscopy of α-Quartz

In 2008—20 years after their often-cited study on buried OTS monolayers (see Fig. 2.2c)—the research group of Yuen-Ron Shen published two back-to-back articles in which the authors promote IR-vis SFG spectroscopy to investigate vibrational modes in the inversion-broken single crystal α-quartz. While one study utilized the experimental degrees of freedom provided by the second-order technique to isolate the SFG signal originating from the *surface* of the polar dielectric [30], the other comprehensively explores SFG vibrational spectroscopy as a probe of its *bulk* phonon properties [32].
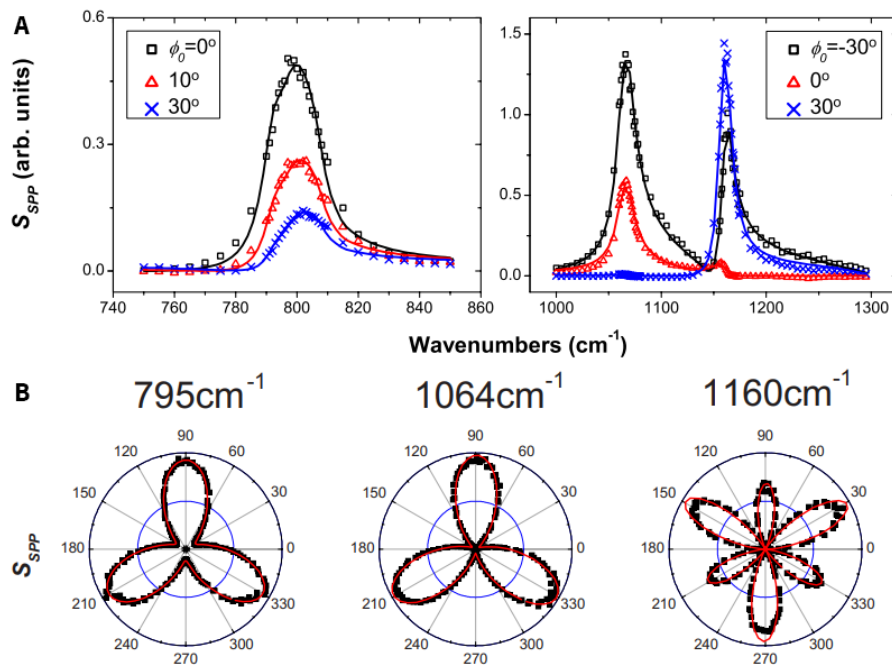
Figure 2.3. **IR-visible SFG phonon spectroscopy of α-quartz. A:** SFG phonon spectra in the spp polarization geometry at various azimuthal angles, ϕ_0. **B:** Azimuthal dependence of the SFG signal in the same polarization geometry at the three observed resonance frequencies. Reproduced from Ref. 32.

In the latter, the authors present IR-vis SFG spectra in α-quartz's Reststrahlen region [32]. Fig. 2.3A shows the *spp* spectra (denoting *s*-, *p*-, and *p*-polarized SFG output, visible input, and IR input, respectively) which feature three clear peaks at zone-center transversal optical (TO) phonon frequencies. Furthermore, by measuring the SFG signal as a function of the sample's azimuthal angle, a distinct anisotropy pattern—closely linked to the crystal symmetry—is revealed (Fig. 2.3B). With the aid of a theoretical model, the authors fit both, the spectral and azimuthal dependencies of the SFG intensities, and extract resonant characteristics of the observed phonon modes, such as resonant amplitudes and damping rates [32]. Overall, the work presents the second-order nonlinear optical technique as a capable tool to study the vibrational as well as symmetry properties of polar dielectrics with broken inversion symmetry. This thesis largely focuses on the investigation of this material class by means of the closely related technique IR SHG. The following example deals with the latter in particular.

Infrared Second-Harmonic Generation Spectroscopy

Notably, IR second-order spectroscopies have largely focused on SFG rather than SHG, despite the fact that both techniques access very similar symmetry and resonance properties. In fact, the very first demonstration of IR second-order spectroscopy used SHG [33]. However, it was soon realized that SFG holds several technical advantages over SHG, such as detector sensitivity and availability of suitable IR lasers. As a consequence, IR SHG received considerably less attention in the scientific community during the past two decades. However, one important IR SHG study of GaAs by Fritz Keilmann's group [34] showed that IR SHG can access additional information which link back to fundamental properties of the crystal and higher-order lattice forces.

Fig. 2.4 shows the experimental data. The spectrum exhibits a clear maximum around 4.5 THz—close to half the TO phonon frequency of GaAs. The minimum at approximately 5.3 THz marks the zero-crossing of the second-order susceptibility, $\chi^{(2)}(\omega)$, and indicates a cancellation of its ionic and electronic contributions. Based on these results and through appropriate modeling of the $\chi^{(2)}(\omega)$ dispersion as well as linear dispersion effects,[2] the authors were able to infer relative weights of the contributing mechanisms to the second-order susceptibility [34]. In particular, the results indicate a significantly larger relative contribution from a third-order lattice potential anharmonicity compared to a second-order lattice dipole moment than previously predicted by theory [35].

It is clear that the full potential of IR SHG has never been exploited—mainly due to the restricted access to suitable laser sources. It is one major goal of this work to

---

2 Model descriptions for both, linear and second-order nonlinear optical effects—specifically, the $\chi^{(2)}$ dispersion model applied here—will be discussed in further detail in Ch. 3 of this thesis.
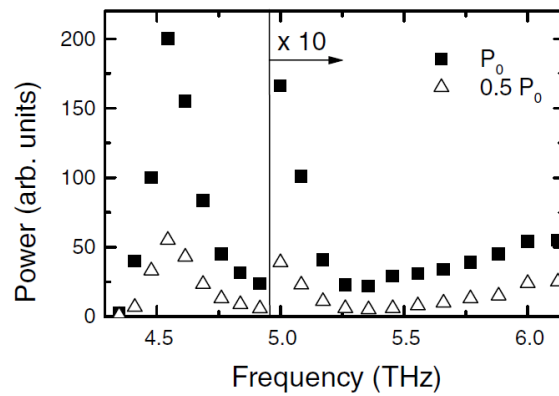
Figure 2.4. **Terahertz SHG spectrum of GaAs.** The second-harmonic signal is resonantly enhanced at half the TO phonon frequency of GaAs. A minimum is observed at 5.3 THz and marks the zero-crossing of $\chi^{(2)}(\omega)$. Reproduced from Ref. 34.

fully explore its capabilities and limitations, using α-quartz as the primary model system. For a proper theoretical framework, the following chapter will lay out the theoretical descriptions of linear and nonlinear optical effects, specifically for polar dielectrics in the IR spectral range.

Chapter 3.

Infrared Second-Order Spectroscopy
Theory

This chapter lays out the theoretical framework for describing second-order non-linear optical effects. This involves linear and nonlinear processes, both of which play a significant role in nonlinear spectroscopy. A particular focus is put on polar dielectrics in the mid-infrared (MIR) wavelength region where optical phonon resonances dominate all optical phenomena.

Sec. 3.1 establishes a general theoretical framework for nonlinear optics. Here, the interaction of light with matter is divided into two basic processes. First, an external electric field, $\mathbf{E}$, induces an electric polarization, $\mathbf{P}$, in the medium. This is described by the so-called *constitutive equation*, relating $\mathbf{E}$ to $\mathbf{P}$ (Sec. 3.1.1) via the nonlinear susceptibility (Sec. 3.1.2). Secondly, the induced polarization itself—now acting as a source—causes the emission of a secondary electric field, $\mathbf{E}^{em}$, following Maxwell's electromagnetic theory (Sec. 3.1.3).

Sec. 3.2 covers optical effects within the linear response limit. Those are fully described by the medium's complex dielectric function, ε, which directly relates to $\chi^{(1)}$ (Sec. 3.2.1). The dielectric function governs all linear optical effects, such as absorption, transmission, and reflection. Also, in anisotropic media, the interplay of different dielectric responses can cause unusual phenomena, such as hyperbolicity which is discussed in Sec. 3.2.2. A complete derivation of Fresnel's transmission and reflection tensors for uniaxial crystals is given in Sec. 3.2.3.

Finally, in Sec. 3.3, the second-order nonlinear response of a medium in the proximity of resonances is discussed. To illustrate the origin of resonantly enhanced nonlinearities—leading to, e.g., enhanced SHG and SFG—the classical anharmonic oscillator is introduced as a simple, yet instructive, microscopic model (Sec. 3.3.1). Secondly, and more concretely, Sec. 3.3.2 treats the dispersion of the second-order nonlinear susceptibility, $\chi^{(2)}$, at and around optical phonon resonances.

3.1. Basics of Nonlinear Optics

A large number of nonlinear optical phenomena—including optical harmonic generation and wave mixing—can be conveniently and accurately described within the theoretical framework of a semi-classical approach where the medium, composed of atoms and molecules, is treated in a quantum mechanical fashion, whereas the optical fields are described by Maxwell's classical theory [1]. In this section, we introduce the tensor formalism of multiple orders of electrical susceptibilities as well as the nonlinear coupled wave equations.

The theoretical groundwork that follows, largely draws from Guang S. He's and Song H. Liu's "*Physics of Nonlinear Optics*" [1] and Yuen-Ron Shen's "*The Principles of Nonlinear Optics*" [36] as well as the author's master's thesis [37].

3.1.1. Optical Field-Induced Electric Polarization

The action of an external electric field, e.g., by means of laser radiation, on a dielectric medium causes a separation of its bound electric charges with respect to the equilibrium state. These charge separations—on a microscopic level—can be expressed in terms of the induced electric dipole moments, $\mathbf{p}$, which collectively form a macroscopic polarization, $\mathbf{P}$:

$$\mathbf{P}(t) = \sum_{i=1}^{N} \mathbf{p}_i(t), \tag{3.1.1}$$

where N denotes the number of microscopic dipoles per unit volume. If the external electric field is that of an electromagnetic wave, $\mathbf{E}(\mathbf{r}, t)$, both, $\mathbf{p}_i$ and $\mathbf{P}$, are generally also functions of position and time. Under the electric dipole approximation, however, i.e., assuming that the wavelength of $\mathbf{E}(\mathbf{r}, t)$ is much larger than the atomic radii in the medium, we can neglect the spatial dependence, thus $\mathbf{E}(\mathbf{r}, t) = \mathbf{E}(t)$ and $\mathbf{P}(\mathbf{r}, t) = \mathbf{P}(t)$. By the principle of causality, $\mathbf{P}(t)$ must be a function of $\mathbf{E}(t)$. In order to establish this relationship, we can express $\mathbf{P}(t)$ as a power series:

$$\mathbf{P}(t) = \mathbf{P}^{(1)}(t) + \mathbf{P}^{(2)}(t) + \mathbf{P}^{(3)}(t) + \cdots + \mathbf{P}^{(n)}(t) + \cdots, \tag{3.1.2}$$

where the nth-order term is assumed to be a function of the nth power of $\mathbf{E}(t)$ and reads [1, 38]:

$$\mathbf{P}^{(n)}(t) = \varepsilon_0 \int_{-\infty}^{\infty} dt_1 \int_{-\infty}^{\infty} dt_2 \cdots \int_{-\infty}^{\infty} dt_n \, R^{(n)}(t_1, t_2, \cdots, t_n) : \mathbf{E}(t - t_1)\mathbf{E}(t - t_2) \cdots \mathbf{E}(t - t_n).$$

$$\tag{3.1.3}$$

Here, $R^{(n)}(t_1, t_2, \cdots t_n)$ represents the nth-order polarization response function of the medium and a tensor of rank $(n+1)$. The time dependence of $\mathbf{E}(t-t_1)$ to $\mathbf{E}(t-t_n)$ is due to the fact that the medium's response is generally not instantaneous and depends on the *relative* timing with respect to the applied field and not on the *absolute* time. Also, per causality principle, $R^{(n)}$ must be zero for t_1 to $t_n < 0$.

If we assume our external light field to be a monochromatic plane wave at frequency ω, the Fourier transform of $\mathbf{E}(t)$ and $\mathbf{P}(t)$, respectively, simplifies to:

$$\mathbf{E}(t) = \int_{-\infty}^{\infty} d\omega' \mathbf{E}(\omega') e^{-i\omega' t} \delta(\omega - \omega') = \mathbf{E}(\omega) e^{-i\omega t}, \tag{3.1.4a}$$

$$\mathbf{P}^{(n)}(t) = \int_{-\infty}^{\infty} d\omega' \mathbf{P}^{(n)}(\omega') e^{-i\omega' t} \delta(\omega - \omega') = \mathbf{P}^{(n)}(\omega) e^{-i\omega t}. \tag{3.1.4b}$$

Applying Eqs. 3.1.4a and 3.1.4b to 3.1.2 and 3.1.3 then leads to:

$$\begin{aligned}
\mathbf{P}(\omega) = \varepsilon_0 \big[&\chi^{(1)}(\omega_1) \cdot \mathbf{E}(\omega_1) \\
&+ \chi^{(2)}(\omega_1, \omega_2) : \mathbf{E}(\omega_1)\mathbf{E}(\omega_2) + \cdots \\
&+ \chi^{(n)}(\omega_1, \omega_2, \cdots, \omega_n) : \mathbf{E}(\omega_1)\mathbf{E}(\omega_2) \cdots \mathbf{E}(\omega_n) + \cdots \big]
\end{aligned} \tag{3.1.5}$$

Here, $\chi^{(n)}(\omega_1, \omega_2, \cdots, \omega_n)$ is the nth-order electric susceptibility tensor and establishes the fundamental relation between the nth-order induced polarization and the electric field components, ω_n, in the frequency domain. Notably, in an experimental context, $\mathbf{E}(\omega_1), \cdots, \mathbf{E}(\omega_n)$ represent the *local* fields which are subject to transmission from air into the medium. This linear process is described by the Fresnel transmission tensor which will be derived and discussed in Sec. 3.2.3.

Like the time domain response function, $R^{(n)}$, $\chi^{(n)}$ is a rank $(n + 1)$ tensor. Some general symmetry properties, specific to second-order susceptibilities, $\chi^{(2)}$, are discussed in the upcoming section. Generally, time and frequency domain descriptions of optical nonlinearities are equivalent. However, using time-dependent response functions can be more convenient for certain types of problems, e.g., those involving short laser pulses or a non-instantaneous response of the medium. Frequency-dependent susceptibility tensors, on the other side, are particularly useful when describing instantaneous processes far from atomic and molecular transitions with quasi-monochromatic light [39]. Within the semi-classical framework, the essential issue in both pictures is to find an expression for the nonlinear polarization in the form of the so-called constitutive equation, e.g., Eq. 3.1.5, which, in turn, acts as a source term for the re-emitted light field, following Maxwell's equations.

3.1.2. Second-Order Nonlinear Susceptibility Tensor

As stated by the frequency-domain constituitive equation (Eq. 3.1.5), the non-linear susceptibility, $\chi^{(n)}$, connects the external electric fields with the induced polarization. Here, we shall take a particular interest in the lowest-order nonlinearity, described by $\chi^{(2)}$. This second-order susceptibility mathematically takes the form of a third-rank tensor, comprising $3^3 = 27$ elements. The tensor product in the second-order nonlinear polarization term, $\mathbf{P}^{(2)}(\omega)$, then yields the following components which in summation form read:

$$P_i^{(2)}(\omega = \omega_1 + \omega_2) = \varepsilon_0 \sum_{jk} \chi_{ijk}^{(2)}(\omega_1, \omega_2)\, E_j(\omega_1)\, E_k(\omega_2) \qquad (3.1.6)$$

where indeces i, j, k denote the Cartesian coordinates, x, y, z. In the following, some basic properties of second-order susceptibilities are discussed.

Spatial Symmetry

As an optical property of the medium, the susceptibility tensor should also reflect the medium's structural symmetry. Specifically, if a medium, e.g., a crystal, is invariant under a certain set of symmetry operations, $\{\mathbf{S}\}$, its $\chi^{(2)}$ tensor should consequently also remain unchanged under these operations. Each symmetry operation, $\mathbf{S}$, then yields the expression [36]:

$$\left(\hat{\mathbf{i}} \cdot \mathbf{S}^\dagger\right) \cdot \chi^{(2)} : \left(\mathbf{S} \cdot \hat{\mathbf{j}}\right)\left(\mathbf{S} \cdot \hat{\mathbf{k}}\right) = \chi_{ijk}^{(2)}, \qquad (3.1.7)$$

where $\hat{\mathbf{i}}, \hat{\mathbf{j}}, \hat{\mathbf{k}}$ denote unit vectors along the Cartesian coordinates. Such symmetry considerations can greatly simplify the $\chi^{(2)}$ tensor. For instance, in the case of inversion symmetry, i.e., the highest symmetry operation, with $\mathbf{S} \cdot \hat{\mathbf{e}} = -\hat{\mathbf{e}}$, it is apparent from Eq. 3.1.7 that $\chi_{ijk}^{(2)} = -\chi_{ijk}^{(2)} = 0$ [36]. This implies that under the electric dipole approximation, no second-order—or, in fact, any even-order—optical effect can occur in centrosymmetric media. However, even for inversion-broken crystals, often only few non-zero tensor elements remain. A (nearly) complete list of symmetry classes and their corresponding independent, non-zero $\chi^{(2)}$ tensor elements can, e.g., be found in Ref. 36.

Permutation Symmetry

A general symmetry relation for $\chi_{ijk}^{(2)}$ can be directly drawn from Eq. 3.1.6. As the order in which the product of the electric fields, $E_j(\omega_1)E_k(\omega_2)$, is carried out does not physically affect the induced polarization, we can deduce the so-called *intrinsic* permutation symmetry: $\chi_{ijk}^{(2)}$ remains unchanged under permutation of the

indeces j, k if the respective frequency arguments are interchanged accordingly:

$$\chi_{ijk}^{(2)}(\omega_1, \omega_2) = \chi_{ikj}^{(2)}(\omega_2, \omega_1). \tag{3.1.8}$$

This permutation invariance can be generalized to any higher-order susceptibility [38]. In the special case of SHG where the electric fields are indistinguishable ($\omega_1 = \omega_2$), the more general equality $\chi_{ijk}^{(2)} = \chi_{ikj}^{(2)}$ holds true and can heighten symmetry in the $\chi^{(2)}$ tensor, thus further reducing the number of independent entries.

3.1.3. Maxwell's Equations in Nonlinear Media

While the induced polarization is determined by the nonlinear susceptibility, the subsequent formation of electromagnetic fields is governed by Maxwell's famous set of differential equations. For non-magnetic and dielectric media, they read [40]:

$$\nabla \times \mathbf{E}(\mathbf{r}, t) = -\mu_0 \frac{\partial \mathbf{H}(\mathbf{r}, t)}{\partial t}, \qquad \text{(Faradays's law)} \tag{3.1.9a}$$

$$\nabla \times \mathbf{H}(\mathbf{r}, t) = \varepsilon_0 \frac{\partial \mathbf{E}(\mathbf{r}, t)}{\partial t} + \frac{\partial \mathbf{P}(\mathbf{r}, t)}{\partial t}. \quad \text{(Ampére's law)} \tag{3.1.9b}$$

Here, $\mathbf{H}(\mathbf{r}, t)$ denotes the magnetic field intensity, μ_0 and ε_0 the free-space permeability and permittivity, respectively. Applying a Fourier transform, and the $\nabla \times$ operation on both sides, Eq. 3.1.9a gives:

$$\nabla \times \nabla \times \mathbf{E}(\mathbf{r}, \omega) = \nabla \times [i\omega \mathbf{H}(\mathbf{r}, \omega)]. \tag{3.1.10}$$

Substituting Eq. 3.1.9b then leads to:

$$\nabla \times \nabla \times \mathbf{E}(\mathbf{r}, \omega) = \omega^2 \mu_0 [\varepsilon_0 \mathbf{E}(\mathbf{r}, \omega) + \mathbf{P}(\mathbf{r}, \omega)]. \tag{3.1.11}$$

In this equation, $\mathbf{P}(\mathbf{r}, \omega)$ can be understood as a source term for the emission of an electric field, $\mathbf{E}^{\text{em}}(\mathbf{r}, \omega)$, and can be split into its linear and nonlinear components, $\mathbf{P}^{(1)}(\omega)$ and $\mathbf{P}^{\text{NL}}(\omega)$, respectively (cf. Eq. 3.1.5):

$$\mathbf{P}(\omega) = \mathbf{P}^{(1)}(\omega) + \mathbf{P}^{\text{NL}}(\omega). \tag{3.1.12}$$

For the linear component, depending on $\chi^{(1)}(\omega)$ only, we invoke the dielectric function, $\varepsilon(\omega)$:

$$\varepsilon(\omega) = \varepsilon_0 \left[1 + \chi^{(1)}(\omega)\right], \tag{3.1.13}$$

which then leads to the so-called nonlinear wave equation:

$$\nabla \times \nabla \times \mathbf{E}(\omega) - \mu_0 \omega^2 \varepsilon(\omega)\mathbf{E}(\omega) = \mu_0 \omega^2 \mathbf{P}^{\text{NL}}(\omega). \tag{3.1.14}$$

In the linear regime, i.e. for sufficiently weak incident fields, we can assume the nonlinear contribution to be negligible: $\mathbf{P}^{\text{NL}}(\omega) \approx 0$. In this case, Eq. 3.1.14 reduces to a *linear* wave equation and the optical response of the medium is fully described by its dielectric function, $\varepsilon(\omega)$. The following section (Sec. 3.2) further discusses the linear response regime.

If, on the other hand, the incident field is that of an intense light source, such as that of a laser, $\mathbf{P}^{\text{NL}}(\omega)$ must be considered and Eq. 3.1.14 becomes a nonlinear differential equation. Here, the higher-order terms in $\mathbf{P}^{\text{NL}}(\omega)$—involving multiple **E**-fields—introduce new frequency components. For example, a second-order nonlinear process caused by two external fields, $\mathbf{E}(\omega_1)$ and $\mathbf{E}(\omega_2)$, which can be expressed through their inverse Fourier transform (cf. Eq. 3.1.4a) [1]:

$$\mathbf{E}(\omega) = \frac{1}{2\pi} \int_{-\omega}^{\infty} dt\, \mathbf{E}(t)e^{i\omega t}, \tag{3.1.15}$$

creates additional frequency components at $\omega = \omega_1 + \omega_2$, $\omega_1 = \omega - \omega_2$, and $\omega_2 = \omega - \omega_1$:

$$\mathbf{P}^{(2)}(\omega = \omega_1 + \omega_2) = \varepsilon_0 \chi^{(2)}(\omega_1, \ \ \omega_2)\mathbf{E}(\omega_1)\mathbf{E}(\omega_2), \tag{3.1.16a}$$

$$\mathbf{P}^{(2)}(\omega_1 = \omega - \omega_2) = \varepsilon_0 \chi^{(2)}(\omega \ , -\omega_2)\mathbf{E}(\omega)\mathbf{E}^*(\omega_2), \tag{3.1.16b}$$

$$\mathbf{P}^{(2)}(\omega_2 = \omega - \omega_1) = \varepsilon_0 \chi^{(2)}(\omega \ , -\omega_1)\mathbf{E}(\omega)\mathbf{E}^*(\omega_1). \tag{3.1.16c}$$

Here, the complex conjugate of $\mathbf{E}(\omega) = \mathbf{E}^*(-\omega)$ has been used [1]. Substituting Eqs. 3.1.16a–3.1.16c into the nonlinear wave equation 3.1.14 creates a set of three coupled differential equations that can, in principle, be solved for $\mathbf{E}(\omega)$, $\mathbf{E}(\omega_1)$, and $\mathbf{E}(\omega_2)$.

3.2. Infrared Linear Optical Response

In section 3.1.3, we have introduced the dielectric function, $\varepsilon(\omega)$, as the physical quantity that governs all linear phenomena in an optical medium, such as refraction, reflection, and absorption. This section specifically deals with the dielectric response of a solid in the IR spectral region where optical phonon resonances dominate its dispersion (Sec. 3.2.1). Anisotropic materials combine different dielectric responses along the principal axes which may lead to remarkable material properties such as hyperbolicity (Sec. 3.2.2). Finally, a complete derivation of reflection and transmission coefficients for uniaxial crystals is given (Sec. 3.2.3), allowing

the calculation of local fields. These—as further discussed in Sec. 3.2.3—play a significant role in both, linear and nonlinear optical experiments.

3.2.1. Infrared Dielectric Function

The dielectric function describes a medium's linear response to an external electric field and is defined by Eq. 3.1.13. More specifically, $\varepsilon(\omega)$ acts as a proportionality factor, connecting the external electric field, $\mathbf{E}(\omega)$, with an electric displacement in the medium, $\mathbf{D}(\omega) = \mathbf{E}(\omega) + \mathbf{P}(\omega) = \varepsilon(\omega)\mathbf{E}(\omega)$. For nonresonant interactions, $\varepsilon(\omega)$ is a purely real quantity and relates to the refractive index via $n^2 = \varepsilon$. In the presence of material resonances, however, an imaginary component arises, representing absorption losses [41]:

$$\varepsilon(\omega) = \varepsilon_1 + i\varepsilon_2. \tag{3.2.1}$$

Here, ε_1 and ε_2 denote the real and imaginary part of the dielectric function, respectively. In this section, we discuss the dispersion of $\varepsilon(\omega)$ in the so-called *Reststrahlen region* of polar crystals, i.e., the MIR spectral range where optic phonon resonances determine the dielectric response.

Generally, the dielectric response is determined by resonant excitations in the material. These resonant contributions can range from lattice vibrations in the MIR ($\sim 10^{13}$ Hz) to electronic resonances in the visible range ($\sim 10^{15}$ Hz). When considering the MIR spectral range—well below any electronic resonances—$\varepsilon(\omega)$ can be expressed as:

$$\varepsilon(\omega) = 1 + \chi_\infty + \chi_{\text{ion}}(\omega), \tag{3.2.2}$$

where χ_∞ contains the non-resonant electronic and $\chi_{\text{ion}}(\omega)$ the resonant ionic, i.e., optical phonon contributions. An expression for the latter can be derived from a simple one-dimensional damped oscillator model [42]. Here, a harmonic electric field, $E(t)$, excites a harmonic oscillator with mass m, charge e, damping γ, and resonance frequency ω_{TO}. The equation of motion then reads [42]:

$$m\ddot{x} + m\gamma\dot{x} + m\omega_{\text{TO}}^2 x = eE_1\,e^{-i\omega t}. \tag{3.2.3}$$

The subscript TO indicates the transversal optical mode which can couple to a transverse electric field. Solving Eq. 3.2.3 with the standard Ansatz $x = x_0\,e^{-i\omega t}$ yields [42]:

$$x = \frac{e}{m}\frac{E_1 e^{-i\omega t}}{\omega_{\text{TO}}^2 - \omega^2 - i\gamma\omega}. \tag{3.2.4}$$

With the induced polarization written as:

$$P = Nex, \tag{3.2.5}$$

where N denotes the number of harmonic oscillators per unit volume, and Eqs. 2.1.1 and 3.2.2, we can express $\varepsilon(\omega)$ as [42]:

$$\varepsilon(\omega) = \varepsilon_\infty + \underbrace{\left(\frac{Ne^2}{m\varepsilon_0}\right)}_{\equiv S} \frac{1}{\left(\omega_{\mathrm{TO}}^2 - \omega^2 - i\gamma\omega\right)}, \tag{3.2.6}$$

where $\varepsilon_\infty = 1 + \chi_\infty$. As indicated in Eq. 3.2.6, it is often useful to replace the term $Ne^2/m\varepsilon_0$—acting as a response strength in a microscopic picture—by a generalized macroscopic oscillator strength, S. This oscillator strength, in turn, can be treated as a dimensionless parameter, e.g., when fitting experimental data, or calculated using a quantum mechanical model. According to Maxwell's equations, longitudinal modes mark the zero-crossings of the dielectric function [43]. Therefore, if we consider the real part of Eq. 3.2.6, we can identify the zero-crossing of $\mathrm{Re}\,\varepsilon(\omega)$ at ω_{LO} as the longitudinal optical (LO) mode frequency [42]:

$$\omega_{\mathrm{LO}}^2 = \omega_{\mathrm{TO}}^2 + \frac{S}{\varepsilon_\infty}. \tag{3.2.7}$$

Solving the above expression for S and substituting into Eq. 3.2.6 then yields the classical Lorentz model of the dielectric function:

$$\varepsilon(\omega) = \varepsilon_\infty \left(1 + \frac{\omega_{\mathrm{LO}}^2 - \omega_{\mathrm{TO}}^2}{\omega_{\mathrm{TO}}^2 - \omega^2 - i\gamma\omega}\right). \tag{3.2.8}$$

Evaluating the low-frequency limit, $\varepsilon(0)$, of Eq. 3.2.8 directly leads to the well-known Lydanne-Sachs-Teller relation [44]:

$$\frac{\varepsilon(0)}{\varepsilon_\infty} = \frac{\omega_{\mathrm{LO}}^2}{\omega_{\mathrm{TO}}^2}. \tag{3.2.9}$$

Fig. 3.1 shows real and imaginary parts of the dielectric function of a single-mode polar crystal with finite damping in the Reststrahlen region (Eq. 3.2.8) together with its reflectivity, R, under normal incidence which reads:

$$R = \left|\frac{\sqrt{\varepsilon(\omega)} - 1}{\sqrt{\varepsilon(\omega)} + 1}\right|^2. \tag{3.2.10}$$

Upon inspection of Eq. 3.2.8 and Fig. 3.1A, it is apparent that $\mathrm{Re}\,[\varepsilon(\omega)]$ takes on negative values for $\omega_{\mathrm{TO}} < \omega < \omega_{\mathrm{LO}}$. This spectral region—often referred to as the *Reststrahlen band*—plays a particular role in the field of IR spectroscopy [45, 46]. Here, the polarization in the crystal is in antiphase with the driving field, causing a screening of the radiation. As a result, light propagation in the crystal is strongly

suppressed and reflectivity close to unity (see Fig. 3.1B). $\text{Im}[\varepsilon(\omega)]$ peaks at ω_{TO} where light couples to the TO mode and is absorbed. At the low-frequency limit ($\omega = 0$), and the high-frequency limit ($\omega \rightarrow \infty$), $\varepsilon(\omega)$ converges towards $\varepsilon(0)$ and ε_∞, respectively.
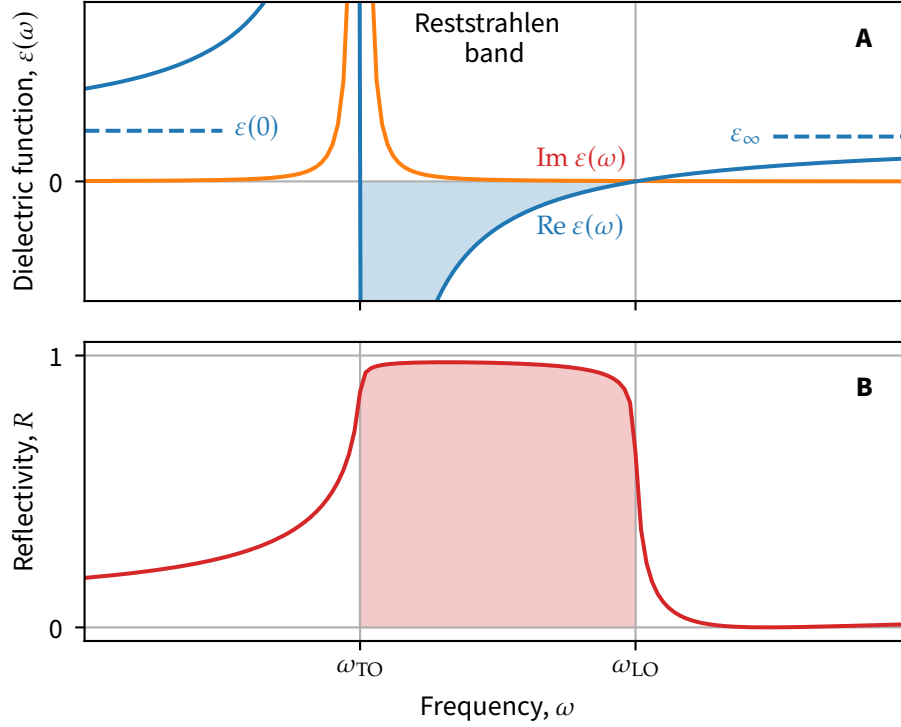
Figure 3.1. **Dielectric function near an optical phonon resonance. A:** Between corresponding TO and LO phonon frequencies, ω_{TO} and ω_{LO}, respectively, the real part of the dielectric function, ε_1, is negative (blue shade), leading to a strongly attenuated wave inside the material. **B:** This results in a region of near-perfect reflectance, the so-called Reststrahlen band (red shade).

A common generalization of the classical oscillator dispersion (Eq. 3.2.8) is the summation over an arbitrary number of oscillator modes [42]:

$$\varepsilon(\omega) = \varepsilon_\infty \left(1 + \sum_j \frac{\omega_{\text{LO}j}^2 - \omega_{\text{TO}j}^2}{\omega_{\text{TO}j}^2 - \omega^2 - i\gamma_j\omega} \right), \tag{3.2.11}$$

where the index j labels the jth oscillator mode. If we consider the undamped case, $\gamma = 0$, it is clear that the dielectric response in Eq. 3.2.11 has poles at all $\omega_{\text{TO}j}$, and—as per definition—crosses zero at all $\omega_{\text{LO}j}$.

For this reason, it is suitable to use a factorized form of the dielectric function [47]. Such a formula is given by the four-parameter semiquantum (FPSQ) model [48–51] which adjusts for zero-crossings (poles) of each mode by zeros in its

respective factor's numerator (denominator). It reads:

$$\varepsilon(\omega) = \varepsilon_\infty \prod_j \frac{\omega_{\mathrm{LO}j}^2 - \omega^2 + i\gamma_{\mathrm{LO}j}\omega}{\omega_{\mathrm{TO}j}^2 - \omega^2 - i\gamma_{\mathrm{TO}j}\omega}. \tag{3.2.12}$$

Notably, this formula accounts for independent damping rates for TO and LO oscillation modes, $\gamma_{\mathrm{TO}j}$ and $\gamma_{\mathrm{LO}j}$, respectively, whereas the classical dispersion assumes a single shared γ. In fact, for a single vibrational mode ($j = 1$), the identity of Eqs. 3.2.8 and 3.2.12 yields $\gamma_{\mathrm{TO}} = \gamma_{\mathrm{LO}}$ [43].

With the aid of either the classical oscillator (Eq. 3.2.11) or the FPSQ model (Eq. 3.2.12), it is in principle possible to predict all linear optical effects in the Reststrahlen region for multimode systems. In anisotropic crystals, the dielectric function mostly takes the form of a diagonal second-rank tensor—exceptions being the monoclinic and triclinic crystal families—with generally independent entries along all three principal axes, each of which yields a different dispersion behavior:

$$\varepsilon(\omega) = \begin{pmatrix} \varepsilon_{xx}(\omega) & 0 & 0 \\ 0 & \varepsilon_{yy}(\omega) & 0 \\ 0 & 0 & \varepsilon_{zz}(\omega) \end{pmatrix}. \tag{3.2.13}$$

The interplay of multiple independent dielectric components may give rise to intriguing effects and phenomena. One that has recently attracted particular interest in the photonics community [52] is discussed in the following section.

3.2.2. Hyperbolicity

Hyperbolicity describes the joint occurrence of both, positive and negative real parts of the principal dielectric components in a given material and spectral range. For the sake of simplicity, we here consider uniaxial crystals which reduces the dielectric tensor to its in-plane and out-of-plane components, $\varepsilon_\perp = \varepsilon_{xx} = \varepsilon_{yy}$ and $\varepsilon_\parallel = \varepsilon_{zz}$, respectively (cf. Eq. 3.2.13). The hyperbolicity condition then reads:

$$\mathrm{Re}\,\varepsilon_\perp \cdot \mathrm{Re}\,\varepsilon_\parallel < 0. \tag{3.2.14}$$

An intuitive understanding of the properties of hyperbolic materials is most easily gained by picturing isofrequency surfaces in momentum space. These are given by:

$$\frac{k_x^2 + k_y^2}{\varepsilon_\perp} + \frac{k_z^2}{\varepsilon_\parallel} = \left(\frac{\omega}{c}\right)^2, \tag{3.2.15}$$

where k denotes the wave vector, ω the frequency, and c the speed of light. For hyperbolic materials, Eq. 3.2.15 describes an open hyperboloid as opposed to
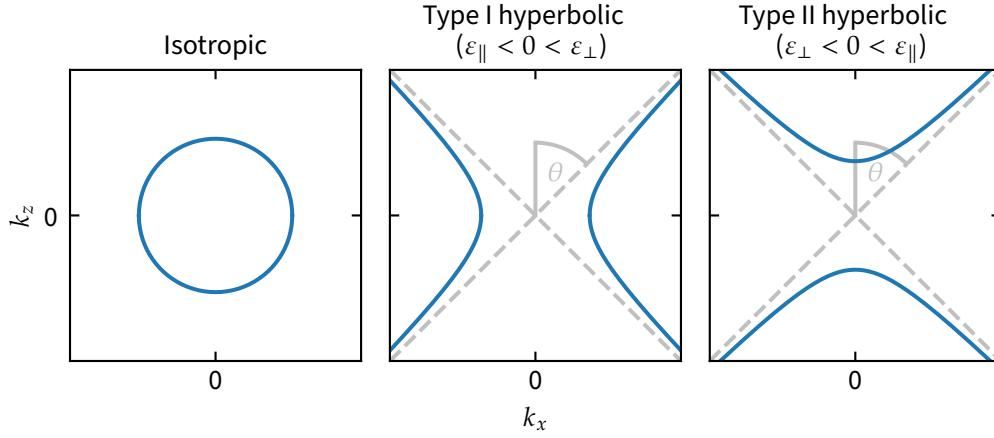
Figure 3.2. Isofrequency contours in momentum space for isotropic and hyperbolic materials. The $k_y = 0$ cuts show that, unlike isotropic materials, hyperbolic materials sustain open isofrequency surfaces, giving rise to highly directional large-momentum modes. Asymptotes under the hyperbolic angle θ (dashed lines) mark the hyperboloids' directionality at high momenta.

isotropic materials whose isofrequency surfaces resemble closed spheres. Generally, the hyperbolicity condition (Eq. 3.2.14) gives rise to two types of hyperbolicity, depending on whether one ($\varepsilon_\parallel$) or two ($\varepsilon_\perp$) dielectric components are negative. Fig. 3.2 shows cuts at $k_y = 0$ through the isofrequency surfaces in k-space of an isotropic material as well as type i and type ii hyperbolic materials. Most notably, the k-space topologies in hyperbolic materials—unlike their isotropic counterparts—support unbound wave vector states which, for large k, are well-described by the hyperboloids' asymptotes with slope [53]:

$$\tan\theta = \mathrm{i}\sqrt{\varepsilon_\perp/\varepsilon_\parallel}. \tag{3.2.16}$$

Here, θ denotes the so-called hyperbolic propagation angle. One immediate physical consequence is that these large-k states sustain an exceedingly high spatial frequency which—combined with their rigid directionality—is very well-suited for subdiffractional imaging and nanolithography applications. In fact, several efforts in this field have been made recently, based on both, naturally hyperbolic materials as well as metamaterial approaches [52–54]. Examples for both will be discussed in Chapters 5 and 6 of this work, respectively.

3.2.3. Fresnel Reflection and Transmission Tensors

Once the dielectric tensor of a material is known, it is possible to predict all linear optical phenomena. For instance, the relation between an external electric field and the local electric fields inside the material as well as the electric field of the reflected beam are determined by the Fresnel tensors of transmission and reflec-

tion, respectively. These solely depend on the material's dielectric tensor and—for anisotropic media—take the form of diagonal, second-rank tensors themselves [55].

In the IR spectral region, these local field corrections, like the dielectric function itself, are highly dispersive and play a significant role not only in linear measurements, but also in nonlinear spectroscopies. For instance, the second-order nonlinear polarization in an SHG process generally reads:

$$\mathbf{P}_{SHG}(2\omega) \propto \chi^{(2)}(\omega, \omega) : [L_1(\omega)\,\mathbf{E}_1(\omega)]\,[L_2(\omega)\,\mathbf{E}_2(\omega)]\,, \qquad (3.2.17)$$

where $L_{1(2)}(\omega)$ is the local field correction, i.e., Fresnel transmission tensor element, to the first (second) incident beam, described by its incident electric field vector, $\mathbf{E}_{1(2)}(\omega)$.

Here, we will derive the elements of the Fresnel transmission tensor of a c-cut uniaxial crystal, i.e., the optic axis is perpendicular to the interface. Other cases, such as that of an a-cut crystal whose optic axis is oriented either perpendicular or parallel with respect to an incoming s-polarized light field, can be derived analogously. A full treatment of the latter can be found in Appx. A, along with a full derivation of the corresponding Fresnel reflection coefficients. A summary of all Fresnel elements as well as a discussion of their behavior in the Reststrahlen region is presented at the end of this section.
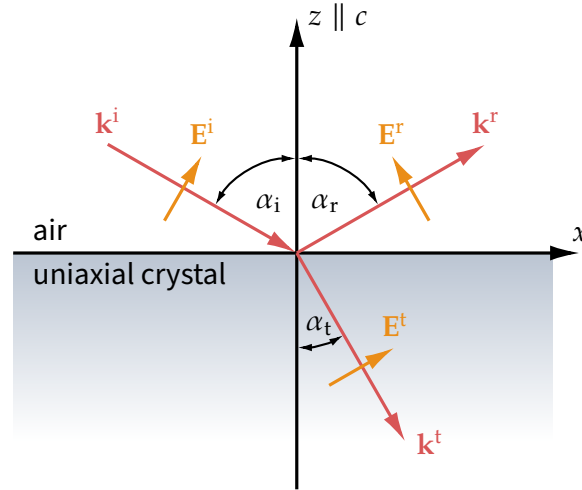
Figure 3.3.   Reflection and transmission: wave vector scheme. Wave vectors, **k**, and electric fields, **E**, for reflection (transmission) of p-polarized light at (through) a c-cut uniaxial crystal. Superscripts i, r, and t mark, respectively, incoming, reflected and transmitted beams.

In the following, **k** denotes the complex wave vector, **E** and **H** its electric and magnetic field vectors, respectively, ε and μ the dielectric function and the magnetic permeability, respectively, and α_i the angle of incidence. Also—without

loss of generality—the interface between air and the uniaxial crystal is set to be the xy-plane of the laboratory coordinate system and the plane of incidence to be the xz-plane as schematically shown in Fig. 3.3.

Transmission Coefficients in *c*-Cut Uniaxial Crystals

The derivation of the Fresnel transmission coefficients will be carried out for a p-polarized external field (polarization *parallel* to the plane of incidence, i.e. $E_y = 0$) first. The analogous case of s-polarized incoming light with the polarization perpendicular to the plane of incidence (from German *"senkrecht":* perpendicular), i.e., $E_x = E_z = 0$, is treated subsequently.

In order to calculate diagonal elements of the Fresnel transmission tensor, we invoke Maxwell's equations in the following way:

$$\underbrace{\nabla \times \mathbf{H} = \varepsilon \frac{\partial \mathbf{E}}{\partial t}}_{\text{(Ampére's law)}} \overset{p\text{-pol.}}{\Longrightarrow} \begin{cases} E_x = \dfrac{k_z}{2\pi\omega\varepsilon_x} H_y \\[2mm] E_z = \dfrac{-k_x}{2\pi\omega\varepsilon_z} H_y \end{cases}, \tag{3.2.18a}$$

$$\underbrace{\nabla \times \mathbf{E} = -\mu \frac{\partial \mathbf{H}}{\partial t}}_{\text{(Faraday's law)}} \overset{p\text{-pol.}}{\Longrightarrow} H_y = \frac{-1}{2\pi\omega\mu}\left(k_x E_z - k_z E_x\right), \tag{3.2.18b}$$

where $\mathbf{E}$ and $\mathbf{H}$ are each proportional to $e^{i(\mathbf{kr}-\omega t)}$. Making use of the conservation of tangential field components at the interface for p-polarized light results in these boundary conditions:

$$E_x^i + E_x^r = E_x^t, \tag{3.2.19a}$$

$$H_y^i + H_y^r = H_y^t \quad \Leftrightarrow \quad H_y^r - H_y^i = H_y^t - 2H_y^i, \tag{3.2.19b}$$

where the superscripts i, r, and t denote, respectively, the incident, reflected, and transmitted beams. Since the electric fields of a p-polarized beam do not have a component along the y-axis, Eqs. 3.2.19a–3.2.19b solely include the x-components of $\mathbf{E}$ and the y-components of $\mathbf{H}$.

Using the boundary condition for E_x (Eq. 3.2.19a) and plugging in the corresponding $\mathbf{E}$-field components as given by Eq. 3.2.18a as well as $k_z^i = -k_z^r$ (see Fig. 3.3), and the boundary condition for H_y (Eq. 3.2.19b), then yields:

$$H_y^t = \underbrace{\frac{2\varepsilon_\perp k_z^i}{\varepsilon_\perp k_z^i + \varepsilon_0 k_z^t}}_{\equiv F} H_y^i, \tag{3.2.20}$$

where $\varepsilon_\perp = \varepsilon_x = \varepsilon_y$ and $\varepsilon_\parallel = \varepsilon_z$ denote the ordinary and extraordinary components of the uniaxial medium's dielectric function, respectively, and $\varepsilon_0 \approx 1$ the

dielectric constant of air. Using Eq. 3.2.20 and inserting it back into Eq. 3.2.18a gives:

$$E_x^t = \frac{k_z^t}{(2\pi\omega)^2 \varepsilon_\perp} F\left(k_z^i E_x^i - k_x^i E_z^i\right),$$ (3.2.21a)

$$E_z^t = \frac{-k_x^t}{(2\pi\omega)^2 \varepsilon_\parallel} F\left(k_z^i E_x^i - k_x^i E_z^i\right).$$ (3.2.21b)

Geometrical relations ($k_x^i = 2\pi\omega \sin\alpha_i$, $k_z^i = 2\pi\omega \cos\alpha_i$, $E_x^i = E^i \cos\alpha_i$ and $E_z^i = -E^i \sin\alpha_i$, see Fig. 3.3) and the definition of F then lead to:

$$E_x^t = \frac{k_z^t}{2\pi\omega\varepsilon_\perp} \frac{\varepsilon_\perp 2k_z^i}{\varepsilon_0 k_z^i + \varepsilon_\perp k_z^t} E^i,$$ (3.2.22a)

$$E_z^t = \frac{k_z^t}{2\pi\omega\varepsilon_\parallel} \frac{\varepsilon_\perp 2k_z^i}{\varepsilon_0 k_z^i + \varepsilon_\perp k_z^t} E^i.$$ (3.2.22b)

With $k_z^i E^i = 2\pi\omega E_x^i$ and $k_x^i E^i = -2\pi\omega E_z^i$, we finally get [56]:

$$E_x^t = \underbrace{\frac{\varepsilon_\perp}{\varepsilon_\perp} \frac{2k_z^t}{\varepsilon_\perp k_z^i + \varepsilon_0 k_z^t}}_{\equiv L_{xx}} E_x^i,$$ (3.2.23a)

$$E_z^t = \underbrace{\frac{\varepsilon_\perp}{\varepsilon_\parallel} \frac{2k_z^i}{\varepsilon_\perp k_z^i + \varepsilon_0 k_z^t}}_{\equiv L_{zz}} E_z^i,$$ (3.2.23b)

(c-cut)

where L_{xx} and L_{zz} are the Fresnel transmission coefficients and $\frac{\varepsilon_\perp}{\varepsilon_\parallel} \equiv \zeta$ is defined as the anisotropy factor [57]. In order to explicitly calculate these transmission coefficients, an expression for the complex wave vector k_z^t is required. This expression has been derived by Mosteller and Wooten based on trigonometrical considerations and Snell's law of refraction and reads [58]:

$$k_z^{t,e} = 2\pi\omega \sqrt{\varepsilon_\perp - \frac{\varepsilon_\perp}{\varepsilon_\parallel} \sin^2\alpha_i}, \quad \text{(c-cut)}$$ (3.2.24)

where the additional superscript e stands for *extraordinary* (polarization parallel to the optic axis *c*) which is a property of *p*-polarized electromagnetic waves traveling along the *z*-direction as opposed to *ordinary* *s*-polarized electromagnetic waves (polarization perpendicular to optic axis *c*, superscript o).

To derive the remaining Fresnel transmission coefficient L_{yy}, we consider an s-polarized wave for which Maxwell's equations—analogous to Eqs. 3.2.18a and

3.2.18b—give:

$$\nabla \times \mathbf{H} = \varepsilon \frac{\partial \mathbf{E}}{\partial t} \quad \overset{s\text{-pol.}}{\Rightarrow} \quad E_y = \frac{-1}{2\pi\omega\varepsilon}\left(k_x H_z - k_z H_x\right), \tag{3.2.25a}$$

(Ampére's law)

$$\nabla \times \mathbf{E} = -\mu \frac{\partial \mathbf{H}}{\partial t} \quad \overset{s\text{-pol.}}{\Rightarrow} \quad \begin{cases} H_x = \dfrac{-k_z}{2\pi\omega\mu} E_y \\[2mm] H_z = \dfrac{k_x}{2\pi\omega\mu} E_y \end{cases}. \tag{3.2.25b}$$

(Faraday's law)

For an s-polarized beam, the conservation of tangential field components reads:

$$E_y^i + E_y^r = E_y^t \quad \Leftrightarrow \quad E_y^r - E_y^i = E_y^t - 2E_y^i, \tag{3.2.26a}$$

$$H_x^i + H_x^r = H_x^t. \tag{3.2.26b}$$

Plugging Eq. 3.2.25b into Eq. 3.2.26b and using Eq. 3.2.26a finally gives an expression for the Fresnel transmission coefficient L_{yy}:

$$E_y^t = \underbrace{\frac{2k_z^i}{k_z^t + k_z^i}}_{\equiv L_{yy}} E_y^i, \quad (c\text{-cut}) \tag{3.2.27}$$

where k_z^t takes the form of $k_z^{t,o}$ for an s-polarized beam and reads [58]:

$$k_z^{t,o} = 2\pi\omega\sqrt{\varepsilon_\perp - \sin^2\alpha_i}. \quad (c\text{-cut}) \tag{3.2.28}$$

For a treatment of a-cut uniaxial crystals as well as the Fresnel reflection coefficients, the reader is referred to Appx. A. The following section summarizes the results and gives a short discussion of the Fresnel coefficients' dispersive behavior in the vicinity of phonon resonances.

Fresnel Coefficients in the Reststrahlen Region

Tab. 3.1 presents an overview of all Fresnel transmission and reflection coefficients derived here and in Appx. A. It will be referred to in later chapters. All Fresnel coefficients can be explicitly calculated if the ordinary and extraordinary components of the dielectric tensor, $\varepsilon_\perp$ and $\varepsilon_\parallel$, respectively, are known. In the vicinity of optic phonon resonances, these are highly dispersive but well-described by the FPSQ model discussed in Sec. 3.2.1 and—in knowledge of the phonon parameters—fully determine the dispersion of reflection and transmission at the interface.

Table 3.1. Fresnel transmission and reflection coefficients for uniaxial crystals.

	c-cut	a-cut ($c \parallel x$)	a-cut ($c \parallel y$)
L_{xx}	$\dfrac{2k_z^{\mathrm{t,e}}}{\varepsilon_\perp k_z^{\mathrm{i}} + \varepsilon_0 k_z^{\mathrm{t,e}}}$	$\dfrac{2k_z^{\mathrm{t,o}}}{\varepsilon_\parallel k_z^{\mathrm{i}} + \varepsilon_0 k_z^{\mathrm{t,o}}}$	$\dfrac{2k_z^{\mathrm{t,o}}}{\varepsilon_\perp k_z^{\mathrm{i}} + \varepsilon_0 k_z^{\mathrm{t,o}}}$
L_{zz}	$\dfrac{\varepsilon_\perp}{\varepsilon_\parallel}\dfrac{2k_z^{\mathrm{i}}}{\varepsilon_\perp k_z^{\mathrm{i}} + \varepsilon_0 k_z^{\mathrm{t,e}}}$	$\dfrac{\varepsilon_\parallel}{\varepsilon_\perp}\dfrac{2k_z^{\mathrm{i}}}{\varepsilon_\parallel k_z^{\mathrm{i}} + \varepsilon_0 k_z^{\mathrm{t,e}}}$	$\dfrac{2k_z^{\mathrm{i}}}{\varepsilon_\perp k_z^{\mathrm{i}} + \varepsilon_0 k_z^{\mathrm{t,o}}}$
L_{yy}	$\dfrac{2k_z^{\mathrm{i}}}{k_z^{\mathrm{t,o}} + k_z^{\mathrm{i}}}$	$\dfrac{2k_z^{\mathrm{i}}}{k_z^{\mathrm{t,o}} + k_z^{\mathrm{i}}}$	$\dfrac{2k_z^{\mathrm{i}}}{k_z^{\mathrm{t,e}} + k_z^{\mathrm{i}}}$
R_{xx}	$-\dfrac{\varepsilon_\perp k_z^{\mathrm{i}} - k_z^{\mathrm{t,e}}}{\varepsilon_\perp k_z^{\mathrm{i}} + k_z^{\mathrm{t,e}}}$	$-\dfrac{\varepsilon_\parallel k_z^{\mathrm{i}} - k_z^{\mathrm{t,e}}}{\varepsilon_\parallel k_z^{\mathrm{i}} + k_z^{\mathrm{t,e}}}$	$-\dfrac{\varepsilon_\perp k_z^{\mathrm{i}} - k_z^{\mathrm{t,o}}}{\varepsilon_\perp k_z^{\mathrm{i}} + k_z^{\mathrm{t,o}}}$
R_{zz}	$\dfrac{\varepsilon_\perp k_z^{\mathrm{i}} - k_z^{\mathrm{t,e}}}{\varepsilon_\perp k_z^{\mathrm{i}} + k_z^{\mathrm{t,e}}}$	$\dfrac{\varepsilon_\parallel k_z^{\mathrm{i}} - k_z^{\mathrm{t,e}}}{\varepsilon_\parallel k_z^{\mathrm{i}} + k_z^{\mathrm{t,e}}}$	$\dfrac{\varepsilon_\perp k_z^{\mathrm{i}} - k_z^{\mathrm{t,o}}}{\varepsilon_\perp k_z^{\mathrm{i}} + k_z^{\mathrm{t,o}}}$
R_{yy}	$\dfrac{k_z^{\mathrm{i}} - k_z^{\mathrm{t,o}}}{k_z^{\mathrm{i}} + k_z^{\mathrm{t,o}}}$	$\dfrac{k_z^{\mathrm{i}} - k_z^{\mathrm{t,o}}}{k_z^{\mathrm{i}} + k_z^{\mathrm{t,o}}}$	$\dfrac{k_z^{\mathrm{i}} - k_z^{\mathrm{t,e}}}{k_z^{\mathrm{i}} + k_z^{\mathrm{t,e}}}$
$k_z^{\mathrm{t,o}}$		$2\pi\omega\sqrt{\varepsilon_\perp - \sin^2\alpha_{\mathrm{i}}}$	
$k_z^{\mathrm{t,e}}$	$2\pi\omega\sqrt{\varepsilon_\perp - \dfrac{\varepsilon_\perp}{\varepsilon_\parallel}\sin^2\alpha_{\mathrm{i}}}$	$2\pi\omega\sqrt{\varepsilon_\parallel - \dfrac{\varepsilon_\parallel}{\varepsilon_\perp}\sin^2\alpha_{\mathrm{i}}}$	$2\pi\omega\sqrt{\varepsilon_\parallel - \sin^2\alpha_{\mathrm{i}}}$

Fig. 3.4 exemplarily shows the calculated dispersions of the reflection and transmission coefficients of a generic single-mode crystal in its Reststrahlen region. For simplicity, the crystal is assumed to be isotropic, i.e., $\varepsilon_\perp = \varepsilon_\parallel$. Prominently, all three transmission coefficients (Fig. 3.4A) exhibit a minimum at the TO phonon frequency, generally causing a suppression of the local fields on resonance. At the upper Reststrahlen edge, on the other hand, local fields along the z and y directions are resonantly enhanced while the x-component is suppressed. Notably, the features at the upper Reststrahlen limit are blue-shifted with respect to the LO phonon frequency. This effect scales with larger incidence angles and is also visible in the reflection coefficients (Fig. 3.4B) where the upper Reststrahlen edge is equally shifted towards higher frequencies as compared to the $\alpha_{\mathrm{i}} = 0°$ case shown in Fig. 3.1.
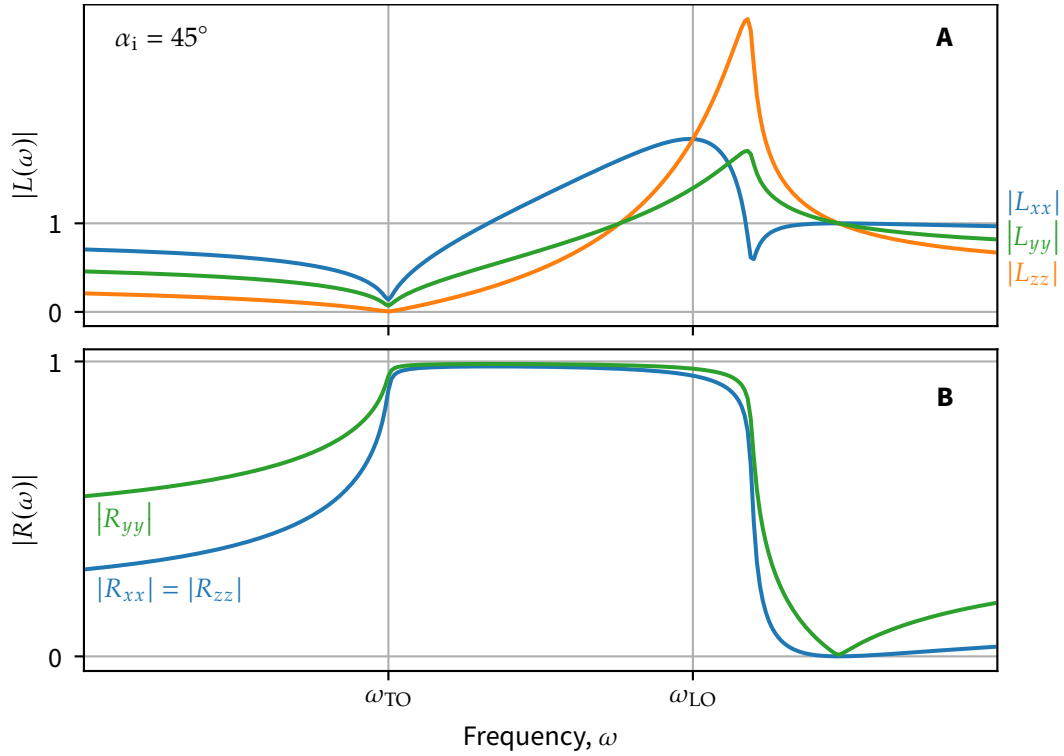
Figure 3.4. **Fresnel coefficients in a single-mode isotropic crystal around phonon resonances. A:** Transmitted fields are suppressed at the TO phonon frequency. **B:** The upper Reststrahlen edge shifts towards higher frequencies for larger incidence angles, α_i.

3.3. Second-Order Nonlinearities at Resonance

While Sec. 3.2 dealt with the description of linear optical phenomena in the spectral vicinity of phonon resonances, this section extends to the nonlinear regime—focusing on second-order effects, such as SHG and SFG. To this end, the anharmonic oscillator model is introduced as an intuitive illustration of optical nonlinearity. Furthermore, a model description for the dispersion of $\chi^{(2)}(\omega)$ in the Reststrahlen region is discussed.

3.3.1. Anharmonic Oscillator Model

The classical anharmonic oscillator model constitutes an instructive way to illustrate the origin of higher-order optical effects in nonlinear media and will be discussed here to provide a microscopic view on nonlinear and, in particular, resonant second-order phenomena. The discussion largely follows that of Refs. 36 and 37.

We consider N classical anharmonic oscillators per unit volume, representing, e.g., core-bound electrons or IR-active molecular vibrations [36]. Under the

influence of a driving force, F, their equation of motion reads:

$$\frac{d^2x}{dt^2} + \gamma \frac{dx}{dt} + \omega_0^2 x + ax^2 = F. \tag{3.3.1}$$

Here, x denotes the spatial coordinate, γ the damping rate, ω_0 the oscillators' resonance frequency, and a an anharmonicity coefficient. We assume the driving force, F, to originate from two applied electric fields, $\mathbf{E}_1$ and $\mathbf{E}_2$, at frequencies $\pm\omega_1$ and $\pm\omega_2$, respectively, acting on the electrons with charge e and mass m:

$$F = \frac{e}{m} \left[E_1 \left(e^{-i\omega_1 t} + e^{i\omega_1 t} \right) + E_2 \left(e^{-i\omega_2 t} + e^{i\omega_2 t} \right) \right]. \tag{3.3.2}$$

For small anharmonicities, a, we can utilize a perturbation approach to describe the solution for x [36]:

$$x = x^{(1)} + x^{(2)} + x^{(3)} + \cdots \tag{3.3.3}$$

In this approximation, the first-order solution, $x^{(1)}$, is then obtained by disabling the anharmonicity, i.e., setting $a = 0$, reducing the solution to that of a damped harmonic oscillator (cf. Sec. 3.2.1) [36]:

$$x^{(1)} = \frac{e}{m} \left[\frac{E_1}{\omega_0^2 - \omega_1^2 - i\gamma\omega_1} e^{i\omega_1 t} + \frac{E_2}{\omega_0^2 - \omega_2^2 - i\gamma\omega_2} e^{i\omega_2 t} \right] + \text{c.c.}, \tag{3.3.4}$$

where c.c. denotes the complex conjugate of the prior terms.

After extending the perturbation to the second order and approximating the second-order term, $ax^2 \approx ax^{(1)^2}$, we obtain from Eq. 3.3.1 [36]:

$$x^{(2)} = x^{(2)}(\omega_1 + \omega_2) + x^{(2)}(\omega_1 - \omega_2) + x^{(2)}(2\omega_1) + x^{(2)}(2\omega_2) + x^{(2)}(0) + \text{c.c.} \tag{3.3.5}$$

Here, the frequency components of $x^{(2)}$ read [36]:

$$x^{(2)}(\omega_1 \pm \omega_2) = \frac{-2a(e/m)^2 E_1 E_2}{\left(\omega_0^2 - \omega_1^2 - i\gamma\omega_1 \right) \left(\omega_0^2 - \omega_2^2 \mp i\gamma\omega_2 \right)}$$
$$\times \frac{1}{\omega_0^2 - (\omega_1 \pm \omega_2)^2 - i\gamma(\omega_1 \pm \omega_2)} e^{-i(\omega_1 \pm \omega_2)t}, \tag{3.3.6a}$$

$$x^{(2)}(2\omega_i) = \frac{-a(e/m)^2 E_i^2}{\left(\omega_0^2 - \omega_i^2 - i\gamma\omega_i \right)^2 \left(\omega_0^2 - 4\omega_i^2 - 2i\gamma\omega_i \right)} e^{-2i\omega_i t}, \tag{3.3.6b}$$

$$x^{(2)}(0) = -a \left(\frac{e}{m} \right)^2 \frac{1}{\omega_0^2} \left(\frac{1}{\omega_0^2 - \omega_1^2 - i\gamma\omega_1} + \frac{1}{\omega_0^2 - \omega_2^2 - i\gamma\omega_2} \right). \tag{3.3.6c}$$

with $i = 1, 2$. Assuming that the induced polarization can be written as $\mathbf{P} = Nex$ (see Eq. 3.2.5), Eqs. 3.3.6a–3.3.6c clearly show the occurrence of new frequency components of $\mathbf{P}$ at $\omega_1 \pm \omega_2$, $2\omega_{1,2}$, and 0, due to the anharmonic interaction of the electric fields with the oscillator [36]. The strength of this nonlinear interaction is given by the anharmonicity, a.

The anharmonic oscillator model readily predicts second-order optical effects, namely sum- and difference-frequency generation ($\omega = \omega_1 \pm \omega_2$), second-harmonic generation ($\omega = 2\omega_i$), as well as optical rectification ($\omega = 0$). Higher-order terms in x (see Eq. 3.3.3) can be calculated iteratively following the perturbation approach and give rise to additional frequency components at $\omega = n_1\omega_1 + n_2\omega_2$ with $n_1, n_2 \in \mathbb{N}$.

3.3.2. Resonant Enhancement

In the previous section, the anharmonic oscillator was introduced as an intuitive example for the nonlinear interaction of two electric fields. Within this picture, the strength of nonlinear interactions scales linearly with the anharmonicity, a, in the oscillator potential. In an optical medium, the anharmonicity of the electric potential is quantified through higher-order terms in the electric susceptibility, $\chi^{(n)}$ (cf. Eqs. 3.1.16a–3.1.16c). In the vicinity of material resonances, $\chi^{(n)}$ behaves highly dispersive, often causing a strong enhancement of nonlinear optical effects at the resonance frequencies.

In the case of dielectric crystals, the eigenstates of low-frequency lattice vibrations are energetically well-separated from high-frequency electronic transitions. The IR dispersion of $\chi^{(2)}(\omega)$ in the vicinity of optic phonon resonances, but far below any electronic transitions, has been investigated by Christos Flytzanis for the simplest class of nonlinear crystals, namely the III-V compounds. These have the cubic $\bar{4}3m$ (or zincblende) symmetry, only one independent nonvanishing element, $\chi^{(2)}_{xyz}$, and one phonon mode [35]. In his comprehensive study, Flytzanis—building on previous works [59–61]—considers three mechanisms leading to nonlinear polarizations in the crystal:

1. Lattice-induced nonlinear polarization expressed in terms of Raman polarizability, first observed by Faust and Henry [61],

2. Phonon interaction through a second-order anharmonic electric potential,

3. Phonon interaction through a third-order mechanical anharmonicity.

His expression reads:

$$\chi^{(2)}(\omega_1, \omega_2) = \chi^{(2)}_{\infty} + \chi^{(2)}_{\text{FH}}(\omega_1, \omega_2) + \chi^{(2)}_{\text{E}}(\omega_1, \omega_2) + \chi^{(2)}_{\text{M}}(\omega_1, \omega_2), \tag{3.3.7}$$

where $\chi_\infty^{(2)}$ is the high-frequency second-order susceptibility and $\chi_{\mathrm{FH}}^{(2)}$, $\chi_{\mathrm{E}}^{(2)}$, and $\chi_{\mathrm{M}}^{(2)}$ represent the contributions listed above. Flytzanis derives their frequency dependence using a semiclassical approach [35]:

$$\chi_{\mathrm{FH}}^{(2)}(\omega_1, \omega_2) = \chi_\infty^{(2)} C_1 \left(\frac{1}{D(\omega_1)} + \frac{1}{D(\omega_2)} + \frac{1}{D(\omega_1 + \omega_2)} \right), \qquad (3.3.8a)$$

$$\chi_{\mathrm{E}}^{(2)}(\omega_1, \omega_2) = \chi_\infty^{(2)} C_2 \left(\frac{1}{D(\omega_1)D(\omega_2)} + \frac{1}{D(\omega_2)D(\omega_1 + \omega_2)} \right.$$
$$\left. + \frac{1}{D(\omega_1 + \omega_2)D(\omega_1)} \right), \qquad (3.3.8b)$$

$$\chi_{\mathrm{M}}^{(2)}(\omega_1, \omega_2) = \chi_\infty^{(2)} C_3 \left(\frac{1}{D(\omega_1)D(\omega_2)D(\omega_1 + \omega_2)} \right). \qquad (3.3.8c)$$

Here, $D(\omega) = 1 - \omega^2/\omega_{\mathrm{TO}}^2 - i\gamma\omega/\omega_{\mathrm{TO}}^2$ is the damped resonant denominator, causing a steep $\chi^{(2)}(\omega)$ enhancement at $\omega = \omega_{\mathrm{TO}}$. The three anharmonic contributions in Eqs. 3.3.8a–3.3.8c depend on the coefficients C_1, C_2, and C_3. These dimensionless parameters are introduced as [35]:

$$C_1 = \frac{\alpha_{\mathrm{TO}}}{2v} \left(\frac{Z^*}{M\omega_{\mathrm{TO}}^2} \right), \qquad (3.3.9a)$$

$$C_2 = \frac{\mu^{(2)}}{2v} \left(\frac{Z^*}{M\omega_{\mathrm{TO}}^2} \right)^2, \qquad (3.3.9b)$$

$$C_3 = -\frac{\phi^{(3)}}{2v} \left(\frac{Z^*}{M\omega_{\mathrm{TO}}^2} \right)^3, \qquad (3.3.9c)$$

where v denotes the volume of the primitive cell, M the reduced mass, and Z^* the effective charge. Further, α_{TO} is the TO Raman polarizability, $\mu^{(2)}$ the second-order dipole moment, and $\phi^{(3)}$ a third-order lattice potential. It has been demonstrated by Eric Roman et al. through ab initio calculations that for III-V Zincblende semiconductors, the contribution from the third-order lattice potential dominates over that of the second-order lattice dipole moment: $|C_2/C_3| \ll 1$ [62].

One goal of this thesis is to explore the ability of SHG spectroscopy to experimentally access the anharmonic lattice parameters described above. As will be discussed in Ch. 5, this is exceedingly difficult in complex crystals like α-quartz due to multiple contributing tensor elements and the strong impact of linear optical effects.

Chapter 4.

Second-Harmonic and Sum-Frequency Generation Spectroscopy
Experiment

This chapter lays out the technical details of the experiments conducted in the scope of this work. In large part, second-harmonic phonon spectroscopy has been employed to study vibrational modes in crystalline solids. This nonlinear optical technique requires a light source that provides sufficiently large IR fields while being tunable and narrowband. An IR FEL meets these requirements and serves as the primary spectroscopic tool. To this end, Sec. 4.1 gives a brief review of the Fritz Haber Institute (FHI) FEL, its working principle, and specifications.

Sec. 4.2 discusses the implementation of IR SHG as a spectroscopic method in a noncollinear, reflective geometry and describes its experimental apparatus. Sec. 4.3 briefly summarizes the realization of an IR-visible SFG experiment which includes an FEL-synchronized table-top laser system. This setup has been implemented by Riko Kießling and technical details can be found in his doctoral thesis [63]. Finally, details on sample temperature control, specifically sample heating and liquid helium cooling, are given in Sec. 4.4.
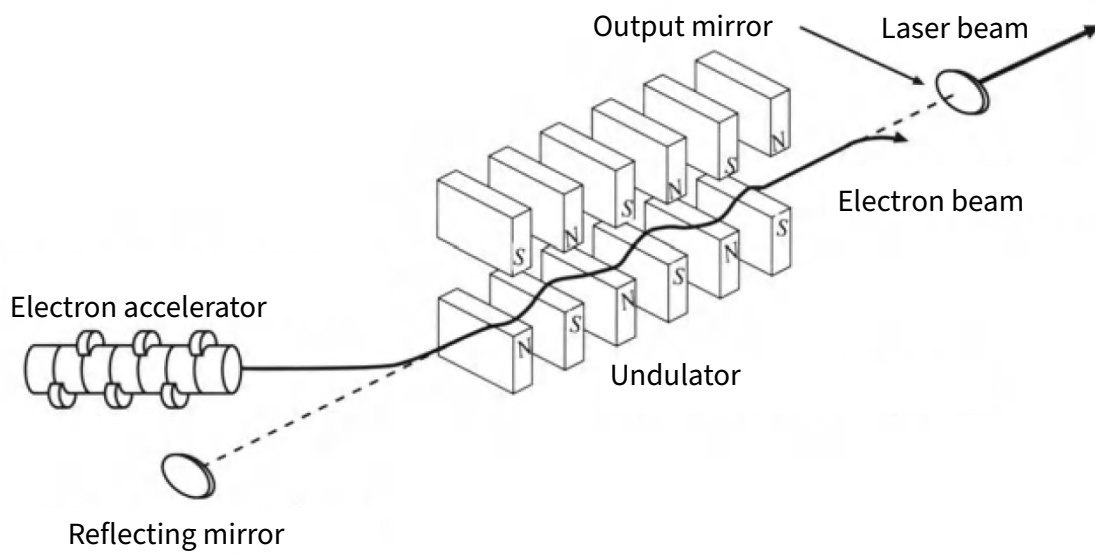
4.1. The FHI Free-Electron Laser

The FEL at the FHI in Berlin started operation in 2013 [64] and has been continuously running user experiments since. This section provides an overview of its basic working principles as well as spectroscopically relevant information about this unconventional light source. Parts of this section are taken from the author's master's thesis [37].

4.1.1. Working Principle

Conventional lasers utilize electronic transitions in the gain medium—usually gases, liquids, or solids—to achieve a population inversion which then enables light amplification through stimulated emission [65]. FELs, in contrast, utilize the

emission of synchrotron radiation from relativistic electrons in a strong periodic magnetic field. The basic setup of an FEL is schematically shown in Fig. 4.1. In this simplified picture, an electron accelerator produces a beam of relativistic electrons which is then injected into an undulator, i.e., periodically arranged pairs of strong permanent magnets with alternating polarities. Here, the electrons experience a Lorentz force induced by the magnetic fields in the undulator, resulting in a wiggling motion with the same spatial periodicity, λ_U, as the permanent magnets. At each bend of the relativistic electrons' trajectory, the accelerated motion causes the additional kinetic energy to be emitted in form of electromagnetic waves, i.e., synchrotron radiation.


Figure 4.1. **Basic setup of a free-electron laser.** Relativistic electrons are injected into the undulator using bending magnets where synchrotron radiation is generated. From reference [66].

In order for the synchrotron wave pulses from each turn to interfere constructively, the following condition must be met [66]:

$$n\lambda = c\,\frac{\lambda_\mathrm{U}}{\bar{v}_z} - \lambda_\mathrm{U}\cos\theta. \qquad (4.1.1)$$

Here, λ denotes the optical wavelength of the synchrotron wave pulses, $\bar{v}_z$ the average velocity of the electron beam along the undulator axis, z, and θ the angle of the synchrotron pulse propagation with respect to z. The integer n represents the interference order where $n = 1$ corresponds to the fundamental wavelength and $n > 1$ to higher harmonics. A schematic of the electrons' trajectory through the undulator is shown in Fig. 4.2. The constructive interference of synchrotron

radiation can be understood as an FEL's equivalent of a conventional laser's spontaneous emission process.
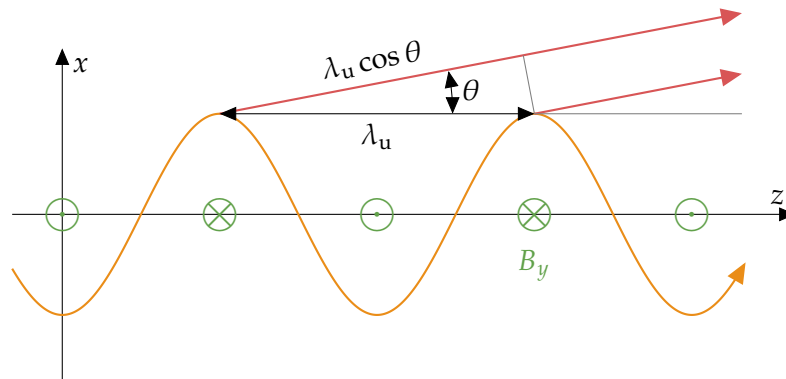
Figure 4.2. **Schematic of an electron beam's trajectory in the undulator.** Due to the magnetic field (green), B_y, the electrons (orange) experience a Lorentz force, forcing them onto an oscillatory trajectory. For the synchrotron pulses (red) to interfere constructively, the phase advance must be a multiple integer of their wavelength, λ [67].

Consequently, the emitted light field now interacts with the electron beam, resulting in a modulation of the spatial distribution of electrons along their propagation direction—a process referred to as *microbunching* [68]. This feedback mechanism causes an energy transfer either from the electron beam to the light field (gain) or vice versa (loss), depending on their relative phase advance. If the interference condition of Eq. 4.1.1 is met exactly, the phase advance is zero and no net energy transfer occurs as absorption and gain compensate each other. This situation is depicted in Fig. 4.3A. If, however, the electron energy is set slightly above resonance as shown in Fig. 4.3B, a net amount of energy is transferred from the electron beam into the light field, i.e., a gain state is reached and lasing sets in. If the undulator is built inside an optical cavity, the light field does multiple roundtrips, thus interacting repeatedly with the electron beam before being outcoupled, resulting in strongly increased gain.

In practice, the electron energy is set such that the lasing regime falls in a wavelength region of the synchrotron spectrum that corresponds to the desired scan range. Variation of the magnetic field strength, B_y, at a fixed electron energy then allows to finely tune the amplified output wavelength while maintaining the lasing state. This is achieved by controlling the undulator gap. During a wavelength scan, the cavity length, L, is adjusted to match the expression:

$$L = L_0 - q\lambda, \tag{4.1.2}$$

where L_0 is the nominal cavity length, λ the output wavelength, and q a user-defined value—the cavity detuning. Keeping q constant over a wavelength scan increases the accessible spectral range and maintains the emitted radiation's rela-
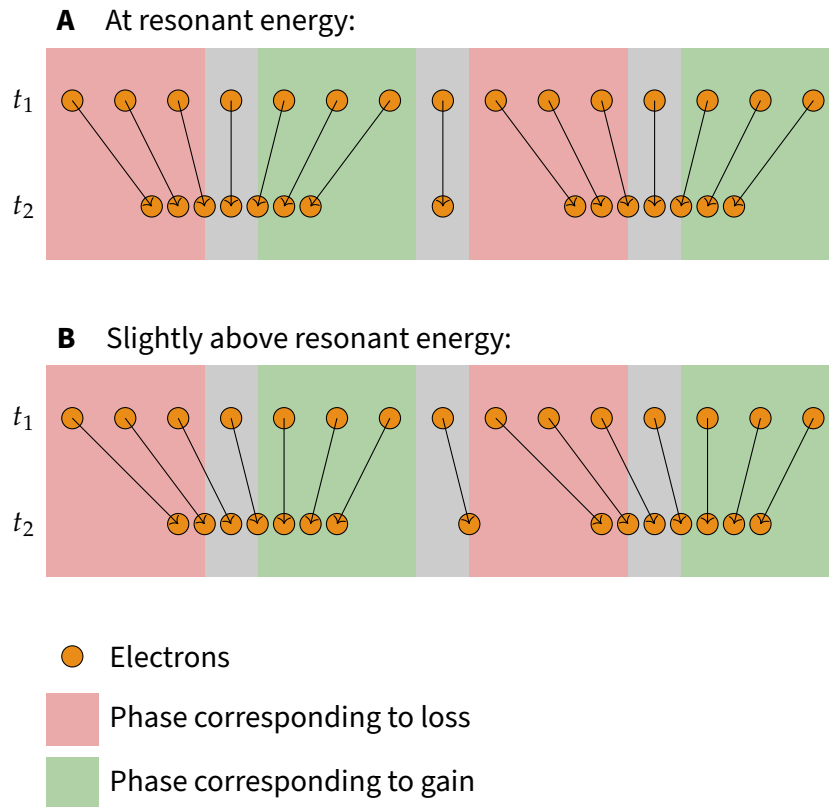
Figure 4.3. **Microbunching in phase space.** The spatial distribution of a homogeneous electron beam at time t_1 is modulated by the optical field. Depending on the relative phase advance of the electron beam and the light field, de- and acceleration of electrons cause net energy absorption (red) or gain (green) at t_2. **A:** The resonant case results in zero net gain. **B:** An electron energy slightly above resonance leads to a positive net gain [67].

tive bandwidth [37, 64]—an oftentimes important experimental parameter. Control over q allows adjustment of the spectral bandwidth which directly relates to the achievable pulse duration via the time-bandwidth product.

In nonlinear spectroscopy, short pulses are often advantageous as they yield higher peak intensities and thus larger nonlinear signals. On the other hand, shorter pulses come at the cost of a broader bandwidth and therefore reduced spectral resolution. The optimal choice of q therefore depends on the width of the spectral features to be studied as well as the general signal levels in the system at hand.

4.1.2. Specifications

This section summarizes the experimentally relevant specifications of the FHI FEL which are largely taken from Ref. 64. A schematic of its layout is depicted in Fig. 4.4. A thermionic gridded electron gun emits electron pulses at 1 GHz which are subsequently compressed in a buncher cavity and captured by an accelerator
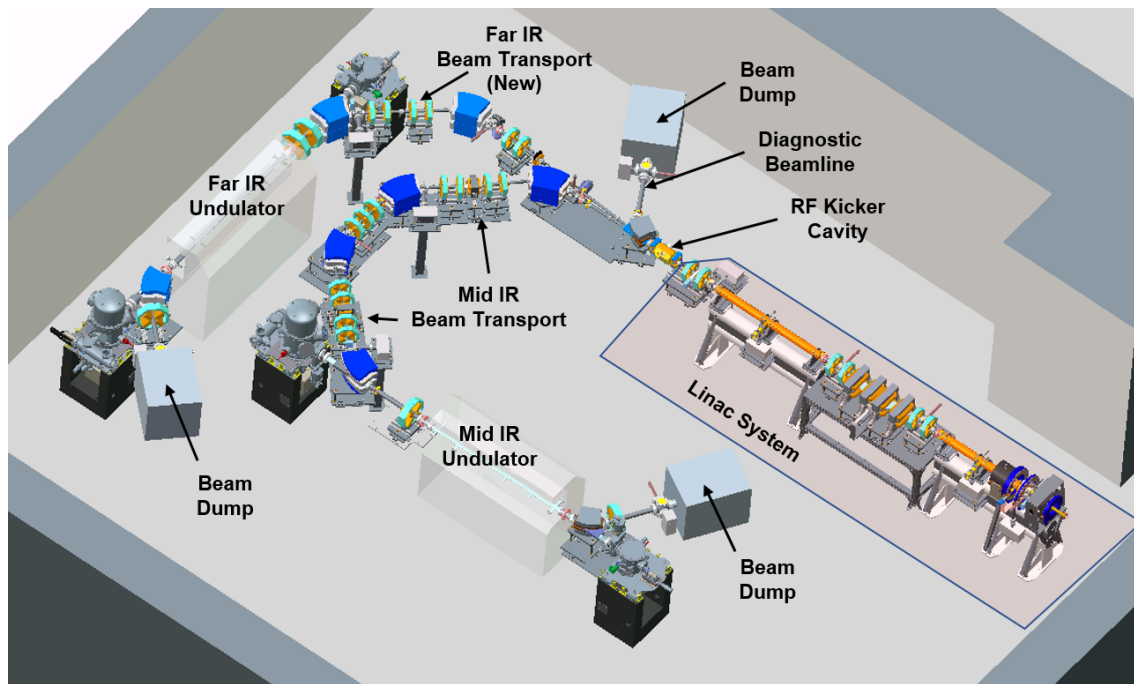
Figure 4.4. **FHI FEL layout.** Two linear accelerators (linacs) generate relativistic electrons with energies ranging from 15 MeV to 50 MeV. These are then, via isochronous bends, injected into the undulator cavity where coherent IR radiation is generated.

system (Advanced Energy Systems), comprising two linear accelerators (linac 1 and 2). Linac 1 accelerates the electron bunches to a constant energy of 20 MeV. Linac 2 then accelerates or decelerates the electrons to any final energy between 15 and 50 MeV before two isochronous achromats inject the electron beam into a MIR undulator [64]. Usually, the electron accelerator is operated at a micro-bunch length of ~1 ps at 1 GHz repetition rate delivered in 10 μs long macro-pulses at 10 Hz.

The 2.0 m long MIR undulator (STI Optronics) comprises 100 pairs (50 periods) of NdFeB permanent magnets with a minimum gap of 16.5 mm. It is built inside the MIR optical cavity, bound by two concave gold-plated copper mirrors—one end mirror and one hole-outcoupling mirror. For optimal performance at a specific wavelength range, the latter can be any of five mirrors with different hole diameters, 0.75, 1.00, 1.50, 2.50, and 3.50 mm, put in position by a motorized mirror changer. The entire tuning range of the MIR beamline extends from 3 to 50 μm. Its essential specifications are summarized in Tab. 4.1.

Currently, an extension of the FEL setup is under construction. This upgrade involves a second beamline with a far-infrared (FIR)/THz undulator which extends the accessible wavelength range to 400 μm and can be run alongside the MIR beamline in a two-color-IR operation mode in which electron bunches are alternatingly injected into the MIR and FIR/THz undulator.

Table 4.1. Specifications of the MIR beamline at the FHI FEL.

	Parameter	Value
λ_{U}	Undulator period	40 mm
	Number of periods	50
	Undulator length	2.0 m
L_0	Cavity length	5.4 m
	Electron energy	15 to 50 MeV
λ	Output wavelength	3 to 50 μm
	Micropulse length	1 to 5 ps
	Micropulse repetition rate	1 GHz
	Macropulse length	1 to 15 μs
	Macropulse repetition rate	10 Hz

4.2. Infrared Second-Harmonic Generation Spectroscopy

Employing IR SHG as a spectroscopic technique requires an optical arrangement that facilitates the separation of the generated second-harmonic signal from the fundamental excitation beams. To this end, a noncollinear excitation scheme provides an elegant method as the SHG light inherently emerges spatially separated from the fundamental beams. A possible implementation is shown in Fig. 4.5.
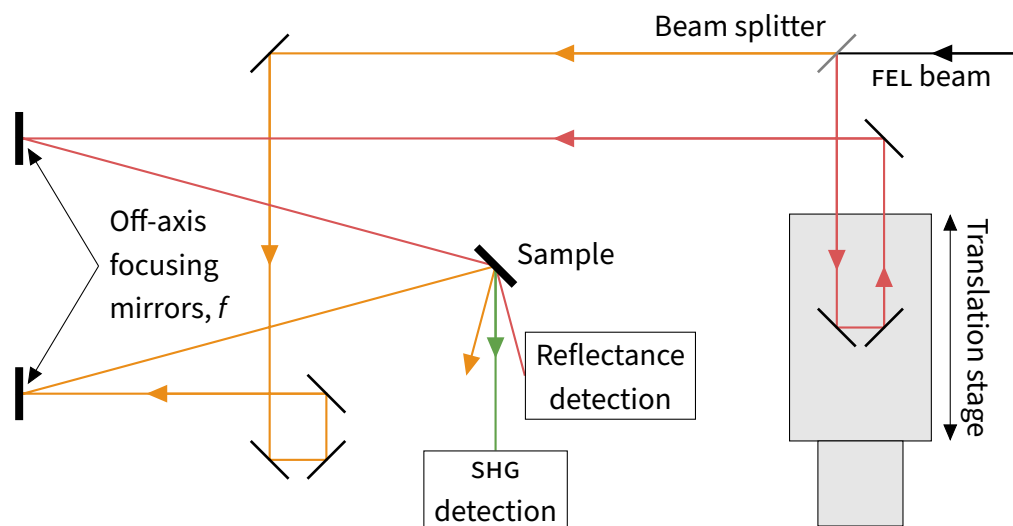
Figure 4.5. Schematic of the SHG setup. A linear translation stage ensures temporal overlap between both excitation arms. The generated second-harmonic signal is captured by an MCT detector. Simultaneously, the linear reflectance signal is measured by a pyroelectric detector.

Here, the FEL beam enters the setup and is split into two excitation arms. A rectangular gold mirror with a sharp upper edge serves as a beam splitter by

geometrically separating the upper and lower halves of the FEL beam, allowing a wavelength-independent 50:50 split in the entire IR spectral range. The first (unreflected) beam path leads to a 15° off-axis parabolic focusing gold mirror (Edmund Optics) which then focuses the beam onto the sample. Meanwhile, the second (reflected) beam—before being focused—is led through a motorized linear translation stage (Newport) to adjust its relative path length with respect to the first excitation beam. This is necessary to achieve temporal overlap of the FEL pulses. In both beam paths, the number of reflective optics has been deliberately chosen to be even in order to minimize the impact of possible FEL pointing drifts on the spatial overlap of the two foci on the sample.

The sample itself is positioned at a 45° angle, resulting in incidence angles $\alpha_1^i = 30°$ and $\alpha_2^i = 60°$ of the first and second excitation beam, respectively, in a reflective geometry. With spatially and temporally overlapping FEL pulses on the sample, the SHG signal emerges between both reflected fundamental beams under $\alpha_{\text{SHG}}^r = \arcsin\left[\left(\sin\alpha_1^i + \sin\alpha_2^i\right)/2\right] \approx 43°$. Another two off-axis focusing mirrors recollimate and refocus the signal beam onto a liquid nitrogen-cooled mercury cadmium telluride (MCT) detector (InfraRed Associates). Simultaneously, the intensity of one (or both) reflected fundamental beams is measured by a pyroelectric photodetector (home-built), providing linear reflectance spectra alongside the nonlinear SHG spectra.

In addition to spatially separating fundamental and nonlinear beams, a selection of spectral long-pass (LP) and short-pass (SP) edge filters are used for spectral separation. This serves two purposes: First, LP filters placed in the incoming fundamental beam prevent FEL-intrinsic higher harmonics (cf. Eq. 4.1.1 for $n > 1$) from being scattered and unintendedly detected by the MCT. Secondly, SP filters are positioned directly in front of the MCT to keep stray fundamental light from influencing the detected signal.

Polarization control of the IR is achieved through a set of wire grid polarizers (Thorlabs) which only transmit the IR radiation's polarization component perpendicular to the wires' orientation. By using two wire grid polarizers in sequence—oriented at 45° and 90°, respectively, with respect to the incoming polarization—the polarization state can be changed from p to s (and vice versa). With a third polarizer, analyzing the detected SHG beam, all possible polarization configurations in a two-beam SHG experiment can be achieved.

4.3. Infrared-Visible Sum-Frequency Generation Spectroscopy

Infrared-visible (IR-vis) SFG spectroscopy constitutes an attractive alternative to IR SHG as the generated nonlinear signal lies in the visible spectral range, enabling the detection of individual photons, e.g., by means of highly sensitive photo-

multiplier tubes (PMTs). As a second light source alongside the FEL, a table-top high-power Tb-doped fiber oscillator (FO) (Onefive) has been employed, providing near-infrared ($\lambda = 1052$ nm), ~100 fs long pulses of 50 nJ at a repetition rate of 55.5 MHz [69]. Combining the IR FEL with the table-top FO, however, requires the pulses of both light sources to be in temporal synchronization. This is achieved using a time-stabilized 2.99 GHz radio frequency fiber link, connecting the FEL vault with the FO over a distance of ~100 m. The implementation of the synchronization unit and the optical setup has been done by Riko Kießling. This section only gives a short summary and full technical details are found in Refs. 69 and 63.

The experimental setup is schematically shown in Fig. 4.6. Here, the FO beam is frequency-doubled to 526 nm using a barium borate (BBO) crystal. The relative timing between the synchronized FEL and FO pulses is set by adjusting the FO beam's optical path length with a linear translation stage (Newport). Then, both, the IR and visible beams are focused onto the sample in spatial and temporal overlap. The generated SFG signal is spectrally separated from the visible excitation beam using a spectral filter and detected by a PMT (Thorlabs). The reflected IR beam is refocused onto a pyroelectric detector (self-built), providing linear reflectance spectra.
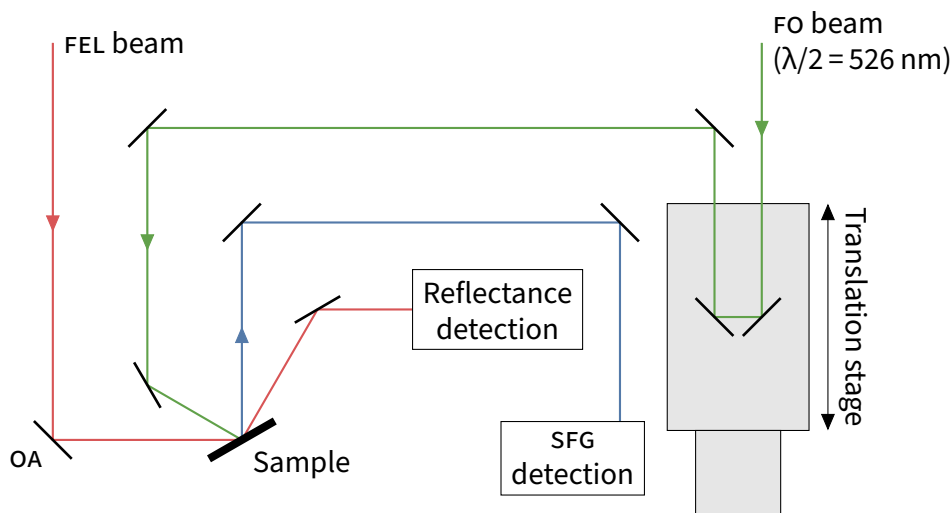
Figure 4.6. IR-vis SFG excitation scheme. The SFG setup comprises an FEL-synchronized, frequency-doubled table-top FO. The relative time delay between both excitation beams is adjusted via a linear translation stage. The SFG signal is spectrally separated from the visible excitation beam and detected by a PMT. Simultaneously, the IR reflectance is captured by a pyroelectric detector.

Beam handling of the FEL is done in analogy to the SHG setup, comprising polarization control using two consecutive wire grid polarizers (Thorlabs) and spectral LP filtering for isolation of the fundamental wavelength. For the visible excitation beam, on the other hand, the polarization is rotated using a $\lambda/2$

waveplate while the detected sfg polarization is analyzed using a polarization filter.

4.4. Sample Temperature Control

Studying a material's temperature-dependent properties or phase transitions requires precise control over the sample temperature. To this end, both, sample heating and cryogenic cooling have been employed. In the following, technical details on both implementations are given.

4.4.1. Sample Heating

In order to raise the sample's temperature in a controlled manner, a probe heater has been built, allowing to adjust the sample temperature to any value between room temperature and 1025 K. Fig. 4.7 shows a schematic of the construction. A heating wire is coiled around a molybdenum sample holder and capped by a stainless steel cover. Here, molybdenum has been chosen due to its high melting point and small thermal expansion. The sample itself is glued to the sample holder using a ceramic adhesive. The actual temperature is measured by two feeler gauges close to the sample and provides feedback to a proportional–integral–derivative (pid) controller (Schneider Electric Systems) which, in turn, adjust the heating current to keep the temperature stable at a set target value within an error margin of <2 K.
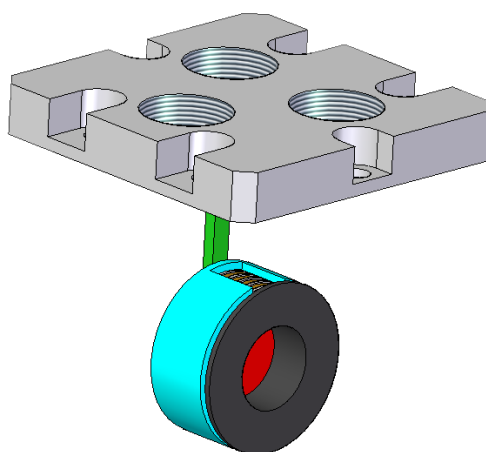
Figure 4.7. Technical drawing of the sample heater. A heating coil is wrapped around the molybdenum sample holder and capped by a steel cover (blue). The sample (red) is glued to the sample holder. Two feeler gauges provide temperature feedback to the pid controller.

4.4.2. Cryogenic Sample Cooling

Some spectroscopic applications, on the other hand, demand sample cooling to cryogenic temperatures. Possible scenarios include the need for larger signals due to lower damping rates as well as phase transitions studies at low temperatures. Such low-temperature applications require a cryogenic apparatus that facilitates the experimental conditions. For this work, a helium bath cryostat (CryoVac) has been employed. Its components are schematically shown in Fig. 4.8. The general cryogenic setup comprises a sample chamber which connects to the liquid helium (LHe) vessel via a heat exchanger. Here, a needle valve allows to finely adjust the flow of cooling fluid from the LHe vessel to the heat exchanger. The LHe vessel contains a volume of ~6.5 L and is enclosed by a liquid nitrogen (LN_2) vessel of approximately ~9 L, serving as a thermal shield. Both cryogenic vessels are surrounded by a high vacuum on the order of 10^{-6} to 10^{-8} mbar.

The sample itself is top-loaded on a sample rod equipped with three motorized manipulators, allowing vertical, polar, and azimuthal alignment of the sample inside the sample chamber. Two silicon diodes—one close to the sample and another at the heat exchanger—provide temperature feedback for a PID controller which regulates the current through two heating wires, also located at the sample mount and the heat exchanger. Optical access to the sample is provided by two Thalliumbromidiodid (KRS-5) and one diamond window at each of three IR access ports. Copper slit apertures at each middle IR window minimize the amount of external heat radiation introduced to the sample chamber.

Generally, the cryostat can be run in two possible modes of operation: as a bath cryostat or as an evaporator, resulting in a combined temperature range of 1.2 K to 325 K:

Bath cryostat In a helium bath cryostat, the sample chamber is flooded with LHe. Thereto, the needle valve is opened and LHe fills up the sample chamber up to the fill level of the LHe vessel. As the sample is entirely surrounded by LHe, the achieved temperature in this operation mode is $T = 4.2$ K. This "single shot" state can be maintained until the LHe in the sample chamber is evaporated or refilled.

In order to achieve lower sample temperatures, $T < 4.2$ K, the sample chamber is, again, flooded with LHe and additionally pumped from the helium exhaust line, resulting in a lower temperature due to the reduced pressure. In this state, temperatures as low as 1.2 K can be reached. Slightly opening the cold valve allows to maintain this state as more LHe is drawn into the sample chamber. In order to set intermediate temperatures 1.2 K $< T < 4.2$ K, a heating current is applied to the sample heater using the PID controller.

Evaporator In an evaporator, the sample chamber is continuously flooded with helium gas. To this end, a heating current is applied to heat exchanger and the cold valve is opened slightly. Thus, LHe from the reservoir evaporates at the heat exchanger and a constant flow of helium gas—finely adjusted by the needle valve—is released into the sample chamber. The sample temperature can then be stabilized to any value $4.2\,\text{K} < T < 325\,\text{K}$ at a precision of $0.1\,\text{K}$, using the PID-controlled sample heater and opening of the needle valve.
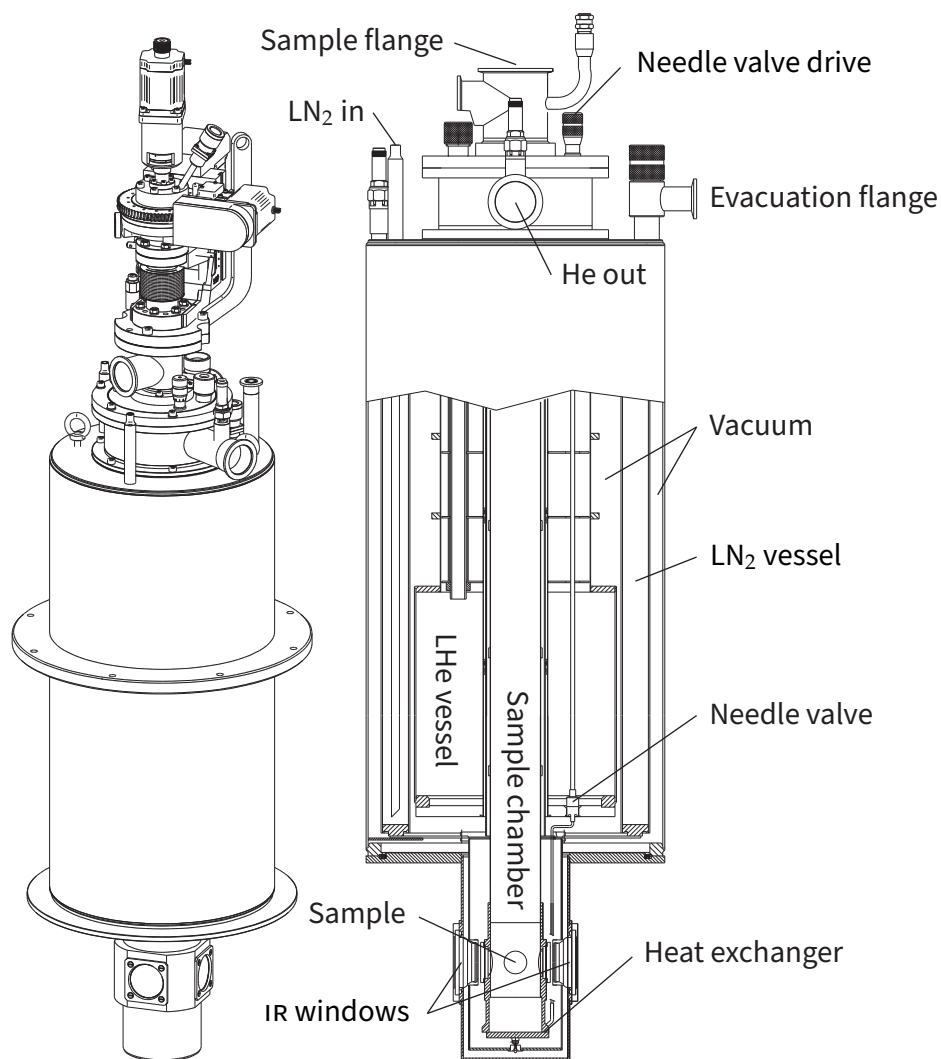
Figure 4.8. Construction drawings of the helium bath cryostat. Helium from the reservoir is fed through the needle valve and the heat exchanger into the sample chamber, either liquid or gaseous. Hence, the cryostat can be operated as either a bath cryostat or as an evaporator. Adapted from Ref. 70.

Chapter 5.

Second-Harmonic Phonon Spectroscopy of α-Quartz

Large parts of this chapter have been published in Refs. 71 and 72. The text strongly draws from these publications.

Raman and linear IR spectroscopies are well-established and the most commonly used techniques for the study of zone-center optical phonons in crystalline solids, providing complementary information on the vibrational modes. However, second-order nonlinear optical techniques provide a promising alternative approach (see Ch. 2). While SHG has been widely applied in the visible spectral region, e.g., for the study of electronic transitions [73, 74], SFG is the most well-established technique in the IR range. In contrast, IR SHG has so far received considerably less attention in the scientific literature [33, 34, 57, 75]. One apparent reason is the scarce availability of intense, tunable, and narrowband IR light sources needed for such experiments. Nevertheless, IR SHG holds several potential advantages over SFG. For instance, the higher symmetry of the nonlinear susceptibility tensor (Sec. 3.1.2) can reduce the number of independent $\chi^{(2)}$ elements and thus simplify symmetry-selective measurements [36]. Moreover, unlike SFG, the SHG process generally includes a doubly resonant excitation and thus a potentially improved phonon enhancement [57]. Finally, SHG's different selection rules grant access to mode symmetries inaccessible by SFG [35].

The work presented in this chapter explores IR SHG as a phonon spectroscopy, making use of the IR FEL at the FHI in Berlin. The goal is to identify the technique's unique capabilities as well as limitations. For this purpose, α-quartz serves as a model system. While the FEL's wide tunability grants access to virtually all of its optic phonon resonances, α-quartz's high-temperature structural phase transition provides an ideal case example for the technique's potential for phase transition studies. The following section summarizes α-quartz's structural and vibrational properties, essential for a comprehensive interpretation of the SHG phonon spectra. Further on, Secs. 5.2, 5.3, and 5.4 discuss the SHG phonon

spectra at room temperature, around quartz's phase transition, and at cryogenic temperatures, respectively.

5.1. Properties of α-Quartz

Quartz has the chemical formula SiO_2 and is a naturally abundant mineral which occurs in Earth's continental crust [76]. To date, its single crystal form, α-quartz, holds great technological importance—mostly due to its useful piezoelectric properties [77]—and has been subject to a large variety of studies. These include SFG [32], Raman [78, 79], and IR spectroscopies [80] as well as neutron [81, 82] and x-ray scattering [83]. Quartz features a broken inversion symmetry, hence supporting even-order nonlinear optical processes as well as numerous vibrational modes. This makes it a well-characterized model system for nonlinear optical techniques and a rich test ground for vibrational spectroscopies. Importantly, its crystalline form undergoes a structural phase transition from trigonal α-quartz to hexagonal β-quartz at a critical temperature of T_c = 846 K. This aspect will be picked up in Sec. 5.3 where high-temperature second-harmonic phonon spectra are analyzed. First, this section provides a brief overview of α-quartz's symmetry and vibrational properties.

Crystal Structure and Symmetry

The crystal lattice of α-quartz is composed of SiO_4 silicon-oxygen tetrahedra where the oxygen atoms are shared with the neighboring tetrahedra's silicon atoms, leading to a net chemical formula of SiO_2. As its crystal structure, shown in Fig. 5.1, is uniaxial, quartz features unique dielectric responses along the
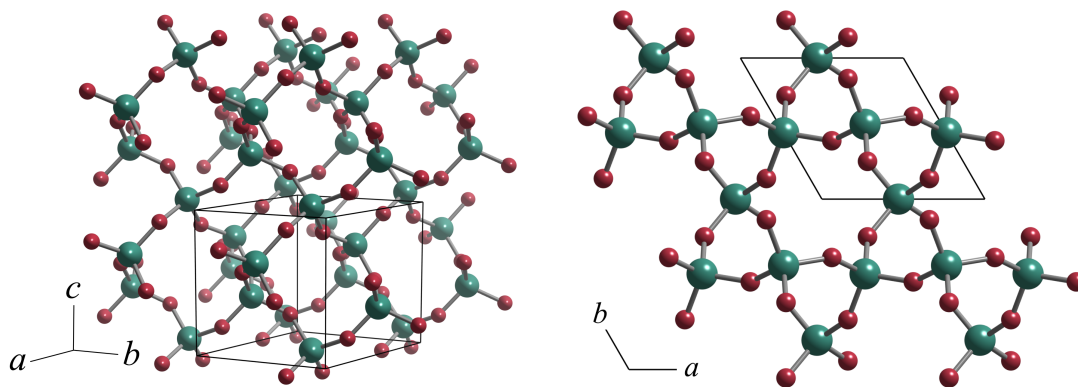
Figure 5.1. **Crystal lattice structure of α-quartz (SiO_2)** with Si atoms (green), O atoms (red) and bonds (gray). The black box marks one unit cell. **Left:** Overview of the crystal structure. **Right:** View along c-axis. Rendered using Ref. 84 with data from Ref. 85.

ordinary *a*- and *b*-axes, and the extraordinary (or optic) *c*-axis.[1] The primitive cell of α-quartz comprises 9 atoms, resulting in a total of 27 phonon branches. Applying symmetry selection rules leaves 13 nondegenerate phonon branches along the ordinary axes and 9 branches along the extraordinary axis. Phonon dispersion curves have been determined using neutron scattering [82] and are shown in Fig. 5.2. In the following section, we focus on α-quartz's IR-active vibrational modes and their properties.
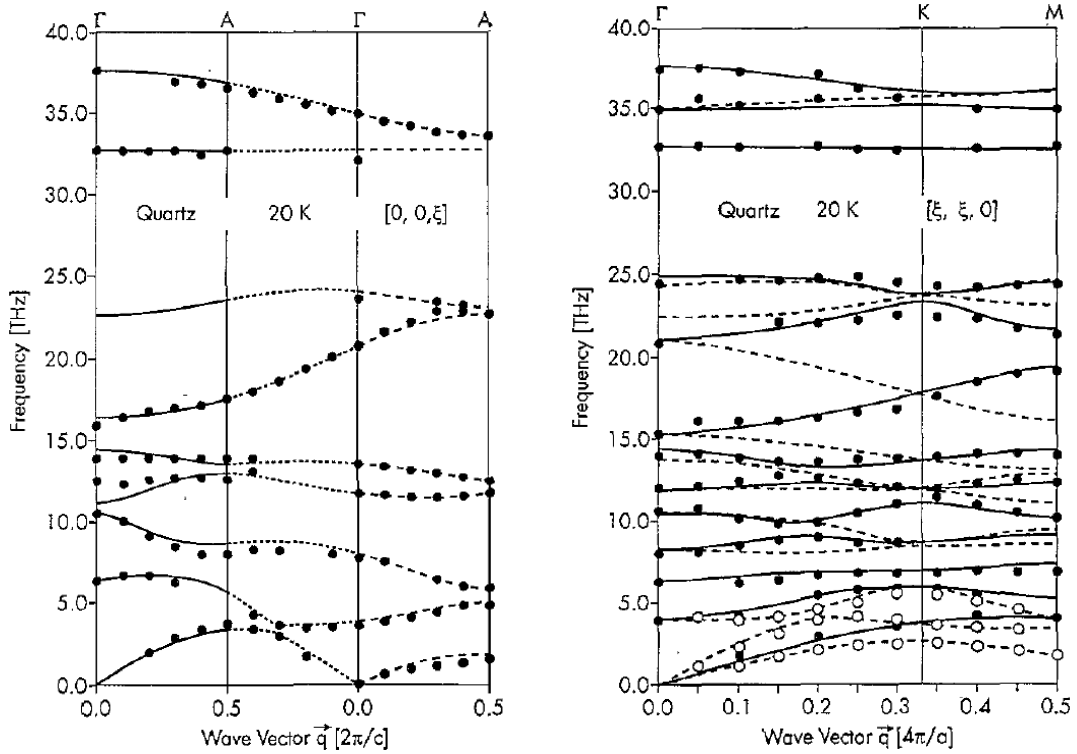

Figure 5.2. Phonon dispersion of α-quartz. The dispersion curves have been measured using neutron scattering at *T*=20 K. **Left:** extraordinary phonon modes. **Right:** ordinary phonon modes. Reproduced from Ref. 82.

Infrared-Active Phonon Modes

Quartz features 8 IR-active optic phonon branches along its ordinary axes (*E*-type) and 4 branches along its extraordinary axis (*A*$_2$-type). While the *E*-type modes are both, IR- and Raman-active, *A*$_2$ modes are exclusively IR-active. A particular comprehensive characterization of these modes' properties has been done by Gervais and Piriou [86]. In their work, the authors acquired IR reflectivity spectra at several temperatures ranging from room temperature up to 975 K, thus covering the phase transition at $T_c = 846$ K. The experimental data is shown in Fig. 5.3.

---

1 This anisotropy also causes a distinct hyperbolic response in α-quartz's lower Reststrahlen region which will be closely examined in Sec. 5.5.
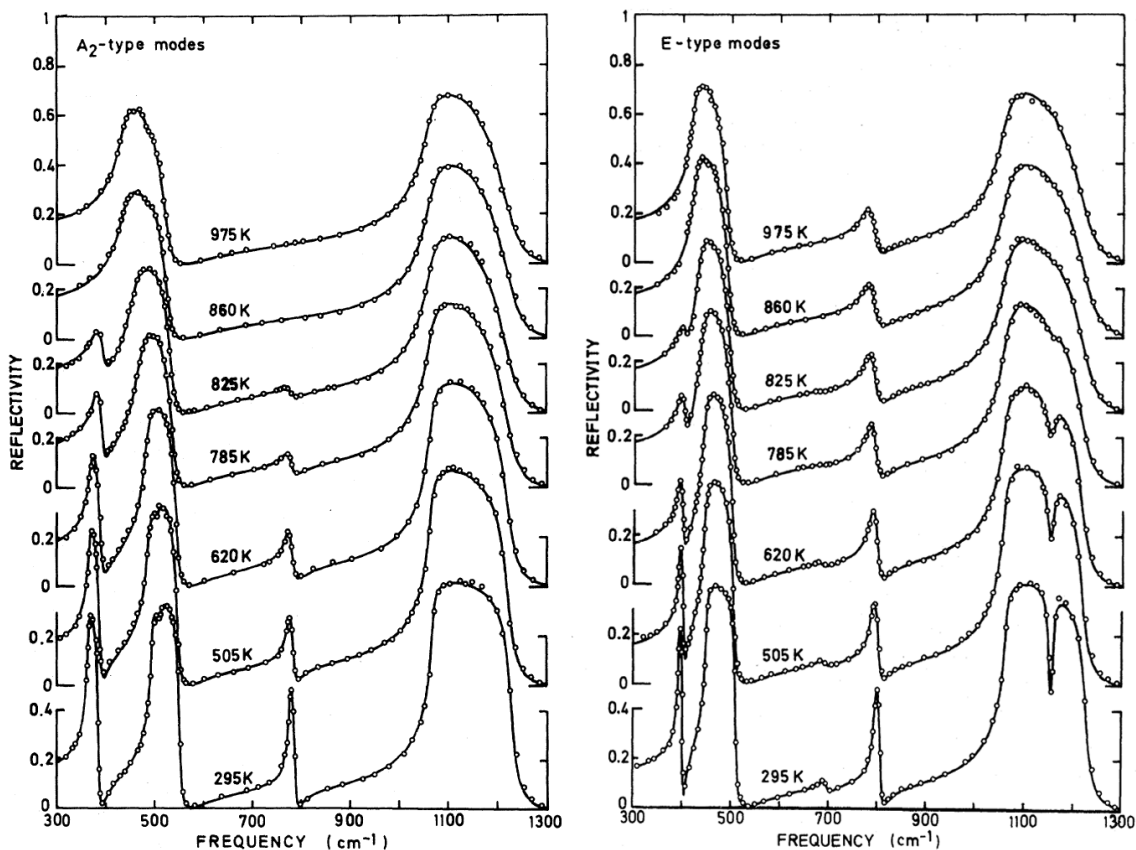
Figure 5.3. **Experimental IR reflectivity spectra** (open circles) at 7 different temperatures and fits according to Eqs. 3.2.10 and 3.2.12 (solid lines). From Ref. 86.

Fitting the normal incidence reflectivity spectra using Eq. 3.2.10 and the FPSQ model for the dielectric response (Eq. 3.2.12) directly yields TO and LO phonon frequencies as well as their respective damping rates as fit parameters. The resulting room temperature phonon properties are summarized in Tab. 5.1 and will be referred to later in this chapter when analyzing α-quartz's IR SHG response at room temperature.

Notably, Gervais' and Piriou's high-temperature data show that upon the α–β phase transition, A_2-type modes labeled $j = 1, 3$ and E-type modes labeled $j = 3, 5, 8$ become IR-forbidden due to the heightened symmetry in the β-phase [86]. As will be demonstrated in Sec. 5.3, this behavior is well-reflected in the temperature-dependent IR SHG spectra.

Second-Order Nonlinear Susceptibility and Second-Harmonic Response

The trigonal crystal structure of α-quartz is classified by the 32 point group (Schoenflies D_3) which generally has four unique, nonvanishing $\chi^{(2)}$ tensor components [36]. For SHG, however—due to its intrinsic symmetry, $\chi^{(2)}_{ijk} = \chi^{(2)}_{ikj}$—these

Table 5.1. A_2- (extraordinary) and E-type (ordinary) phonon mode properties of α-quartz at room temperature. $\Omega_{\text{TO(LO)}j}$ denotes the frequency of the jth TO (LO) phonon and $\gamma_{\text{TO(LO)}j}$ its respective damping rate. E-type modes j=1, 2 are beyond experimental reach of Ref. 86 due to their low resonance frequencies. Data from Ref. 86.

	A_2-type modes					E-type modes			
j	$\Omega_{\text{TO}j}$ [cm^{-1}]	$\Omega_{\text{LO}j}$ [cm^{-1}]	$\gamma_{\text{TO}j}$ [cm^{-1}]	$\gamma_{\text{LO}j}$ [cm^{-1}]	j	$\Omega_{\text{TO}j}$ [cm^{-1}]	$\Omega_{\text{LO}j}$ [cm^{-1}]	$\gamma_{\text{TO}j}$ [cm^{-1}]	$\gamma_{\text{LO}j}$ [cm^{-1}]
1	363.5	386.7	4.8	4.8	3	393.5	402	2.8	2.8
2	495	551.5	5.2	5.8	4	450	510	4.5	4.1
3	777	790	6.7	6.7	5	695	697.6	13	13
4	1071	1229	6.8	12	6	797	810	6.9	6.9
					7	1065	1226	7.2	12.5
(T = 295 K)					8	1158	1155	9.3	9.3

reduce to two (see Sec. 3.1.2):

$$\chi^{(2)}_{aaa} = -\chi^{(2)}_{abb} = -\chi^{(2)}_{bba} = -\chi^{(2)}_{bab},$$
$$\chi^{(2)}_{acb} = -\chi^{(2)}_{bac} = \chi^{(2)}_{abc} = -\chi^{(2)}_{bca}. \tag{5.1.1}$$

These tensor elements determine the crystal's SHG response, in particular its polarization and azimuthal angle dependence. In order to obtain an expression for the latter, a transformation of the $\chi^{(2)}$ tensor from the crystal frame to the laboratory frame is required. The $\chi^{(2)}$ elements in the laboratory frame, (x, y, z), can generally be derived from the contributing $\chi^{(2)}$ tensor elements in terms of crystal coordinates, (a, b, c), using:

$$\chi^{(2)}_{ijk} = \sum_{lmn} \chi^{(2)}_{lmn} \left(\hat{\mathbf{i}} \cdot \hat{\mathbf{l}} \right) \left(\hat{\mathbf{j}} \cdot \hat{\mathbf{m}} \right) \left(\hat{\mathbf{k}} \cdot \hat{\mathbf{n}} \right), \tag{5.1.2}$$

where (i, j, k) and (l, m, n) are the basis vectors of the laboratory and the crystal frame, respectively. Assuming a c-cut α-quartz crystal, the coordinate transformation for a rotation about the c-axis, i.e., surface normal, takes the form: $\hat{\mathbf{a}} = \hat{\mathbf{x}} \cos \varphi + \hat{\mathbf{y}} \sin \varphi$, $\hat{\mathbf{b}} = -\hat{\mathbf{x}} \sin \varphi + \hat{\mathbf{y}} \cos \varphi$, and $\hat{\mathbf{c}} = \hat{\mathbf{z}}$. Applying the crystal to laboratory frame transformation of Eq. 5.1.2 and summing over all $\chi^{(2)}$ elements involved in a given polarization setting then yields the SHG azimuthal angle dependence for that particular measurement. By invoking Eq. 3.2.17, we can obtain the azimuthal angle dependence in terms of the nonlinear polarization with field corrections for SHG, $\mathbf{P}_{\text{SHG}}(2\omega)$, which for α-quartz is nonzero for all polarization combinations. Here, we shall exemplarily show the resulting expressions for the

spp and *ppp* polarization, respectively, as these are relevant to the experimental results presented later in this chapter:

$$
\mathbf{P}_{\mathrm{SHG}}^{spp}(2\omega) \propto \overbrace{\left[L_{zz}(\omega,\alpha_1^{\mathrm{i}})\, L_{xx}(\omega,\alpha_2^{\mathrm{i}}) + L_{xx}(\omega,\alpha_1^{\mathrm{i}})L_{zz}(\omega,\alpha_2^{\mathrm{i}}) \right]}^{\equiv L_{acb}^{\mathrm{eff}}} \chi_{acb}^{(2)}(\omega,\omega)
$$

$$
+ \underbrace{L_{xx}(\omega,\alpha_1^{\mathrm{i}})\, L_{xx}(\omega,\alpha_2^{\mathrm{i}})}_{\equiv L_{aaa}^{\mathrm{eff}}}\, \chi_{aaa}^{(2)}(\omega,\omega)\, \sin(3\varphi),
\tag{5.1.3a}
$$

$$
\mathbf{P}_{\mathrm{SHG}}^{ppp}(2\omega) \propto \underbrace{L_{xx}(\omega,\alpha_1^{\mathrm{i}})\, L_{xx}(\omega,\alpha_2^{\mathrm{i}})}_{= L_{aaa}^{\mathrm{eff}}}\, \chi_{aaa}^{(2)}(\omega,\omega)\, \cos(3\varphi).
\tag{5.1.3b}
$$

Finally, the measured SHG intensity is obtained by projecting the nonlinear polarization onto the electric field direction of the reflected SHG beam, $\hat{\mathbf{e}}_{\mathrm{SHG}}$, and accounting for the transmission of the nonlinear polarization components at 2ω back into air:

$$
I_{\mathrm{SHG}}(2\omega) \propto \left| \left[\tilde{L}_{\mathrm{SHG}}(2\omega)\mathbf{P}_{\mathrm{SHG}}(2\omega) \right] \cdot \hat{\mathbf{e}}_{\mathrm{SHG}} \right|^2 / \Delta k^2,
\tag{5.1.4}
$$

where $\tilde{L}_{\mathrm{SHG}}$ denotes the Fresnel tensor for the reflected SHG beam, coming out of the sample into air. Here $\Delta k^2 = \left| \mathbf{k}_{\mathrm{SHG}}^{\mathrm{t}} - \mathbf{k}_1^{\mathrm{t}} - \mathbf{k}_2^{\mathrm{t}} \right|^2$ accounts for the wave vector mismatch in reflection, with $\mathbf{k}_{1(2)}^{\mathrm{t}}$ being the first (second) transmitted fundamental and $\mathbf{k}_{\mathrm{SHG}}^{\mathrm{r}}$ the reflected SHG wave vector inside the crystal.

Nonlinear Susceptibility Dispersion Model

In Sec. 3.3.2, we have introduced Flytzanis' $\chi^{(2)}(\omega)$ dispersion model for zincblende-type crystals with a single phonon resonance. The multiple phonon modes in α-quartz, however, require a generalized model description. In close analogy to Flytzanis (Eqs. 3.3.7–3.3.8c), the multioscillator expression for the two unique tensor elements relevant for SHG in α-quartz, namely $\chi^{(2)}_{acb}$ and $\chi^{(2)}_{aaa}$, read:

$$\chi^{(2)}_{acb}(2\omega, \omega, \omega) = \chi^{(2)}_{\infty,acb}\left[1 + \sum_{j,k}\left(\frac{C_1^k}{D_k(2\omega)} + \frac{C_1^j}{D_j(\omega)} + \frac{C_1^k}{D_k(\omega)} \right) \right.$$

$$+ \sum_j \sum_k \left(\frac{C_2^{k,j}}{D_k(2\omega)D_j(\omega)} + \frac{C_2^{k,k}}{D_k(2\omega)D_k(\omega)} + \frac{C_2^{j,k}}{D_j(\omega)D_k(\omega)} \right) \quad (5.1.5a)$$

$$\left. + \sum_k \sum_j \sum_{k'} \frac{C_3^{k,j,k'}}{D_k(2\omega)D_j(\omega)D_{k'}(\omega)} \right],$$

$$\chi^{(2)}_{aaa}(2\omega, \omega, \omega) = \chi^{(2)}_{\infty,aaa}\left[1 + \sum_k C_1^k\left(\frac{1}{D_k(2\omega)} + \frac{1}{D_k(\omega)} + \frac{1}{D_k(\omega)} \right) \right.$$

$$+ \sum_k \sum_{k'} C_2^{k,k'}\left(\frac{1}{D_k(2\omega)D_{k'}(\omega)} + \frac{1}{D_k(2\omega)D_{k'}(\omega)} + \frac{1}{D_{k'}(\omega)D_{k'}(\omega)} \right)$$

$$\left. + \sum_k \sum_{k'} \sum_{k''} \frac{C_3^{k,k',k''}}{D_k(2\omega)D_{k'}(\omega)D_{k''}(\omega)} \right].$$

$$(5.1.5b)$$

Here, $D_i(\omega) = 1 - \omega^2/\Omega_{\mathrm{TO}_i}^2 - i\gamma_{\mathrm{TO}_i}\omega/\Omega_{\mathrm{TO}_i}^2$ is the resonant denominator of the ith phonon resonance and indices j and $k^{(',\!'')}$ run through α-quartz's extraordinary and ordinary phonon modes, respectively. Analogous to Flytzanis' single mode model, the resonant amplitudes in this generalized model can be written as (cf. Eqs. 5.1.6a–5.1.6c):

$$C_1^k = \frac{\alpha_{\mathrm{TO}}^k}{2v\chi_\infty^{(2)}}\left(\frac{Z^*}{M\Omega_{\mathrm{TO}}^k} \right), \qquad (5.1.6a)$$

$$C_2^{k,j} = \frac{\mu_{k,j}^{(2)}}{2v\chi_\infty^{(2)}}\left(\frac{Z^*}{M\Omega_{\mathrm{TO}}^k} \right)^2, \qquad (5.1.6b)$$

$$C_3^{k,j,k'} = \frac{\phi_{k,j,k'}^{(3)}}{2v\chi_\infty^{(2)}}\left(\frac{Z^*}{M\Omega_{\mathrm{TO}}^k} \right)^3. \qquad (5.1.6c)$$

The three crucial quantities here are the Raman polarizability, α_{TO}^k, the electrical anharmonicity, $\mu_{k,j}^{(2)}$, and the mechanical anharmonicity, $\phi_{k,j,k'}^{(3)}$. Importantly, SFG spectroscopy solely probes the first-order polarizability, i.e., Raman term [32], due to different selection rules for IR-visible excitation. The latter is *singly* resonant in the IR response and therefore does not probe the anharmonicity of vibrational

potentials. In contrast, IR SHG is *doubly* resonant in its IR response and thus provides access to mechanical and electrical anharmonicities of vibrational modes, lifting the requirement for Raman-type interaction. The latter was argued to be dominant in III-V semiconductors [62] and experimentally shown to be significant for the single-mode polar crystal silicon carbide [57]. For anisotropic multimode systems, these higher-order anharmonicities are of particular importance as they contain information about anharmonic coupling between the multiple phonon modes. In the following, a detailed analysis of α-quartz's IR SHG phonon spectrum is presented.

## 5.2. Second-Harmonic Phonon Spectroscopy at Room Temperature

Experimental Details

The experimental arrangement resembles the one described in Sec. 4.2. The investigated sample is an optically polished single crystal *c*-cut α-quartz window (CRYSTAL), i.e., the optic *c*-axis perpendicular to the surface. For automated azimuthal scans (rotation about the surface normal), the sample was mounted on a motorized rotation stage (Newport). In order to cover the broad Reststrahlen region of α-quartz,[2] different parts of the spectrum were acquired in separate FEL beamtimes and measurement configurations. For the lower spectral region, the FEL electron energy was set to 23.5 MeV, resulting in an FEL tuning range from $350\,\mathrm{cm}^{-1}$ to $850\,\mathrm{cm}^{-1}$. In this setting, 13.5 μm and 9 μm LP filters (LOT) suppress FEL-intrinsic higher harmonics while ZnS/ms (Korth Kristalle) and CaF_2 windows (Thorlabs) act as SP filters to block scattered fundamental light from the MCT detector. For the upper spectral region, from $650\,\mathrm{cm}^{-1}$ to $1400\,\mathrm{cm}^{-1}$, the FEL's electron energy was set to 31 MeV. Here, 9 μm and 7 μm LP filters (LOT) as well as CaF_2, MgF_2 windows (Thorlabs), and a 7 μm SP filter were used. In order to display the acquired data in a single spectrum, multiple overlapping measurements were merged.

Experimental Results

The combined SHG spectrum in the *spp* polarization configuration (denoting *s*-polarized SHG output, and *p*-polarized fundamental inputs) is shown in Fig. 5.4A. The logarithmic plot shows sharp resonances whose amplitudes span approximately three orders of magnitude. These SHG peaks can be largely attributed to α-quartz's *E*-type TO phonon modes (cf. Tab. 5.1) whose spectral positions are

---

2 α-quartz has two optic phonon modes below $350\,\mathrm{cm}^{-1}$ (*E*-type modes $j = 1, 2$) which are not accessible with this experimental setup due to the lack of appropriate filter optics in that wavelength region. Currently, a prism compressor-based filtering unit is in development which would facilitate measurements in that spectral range.
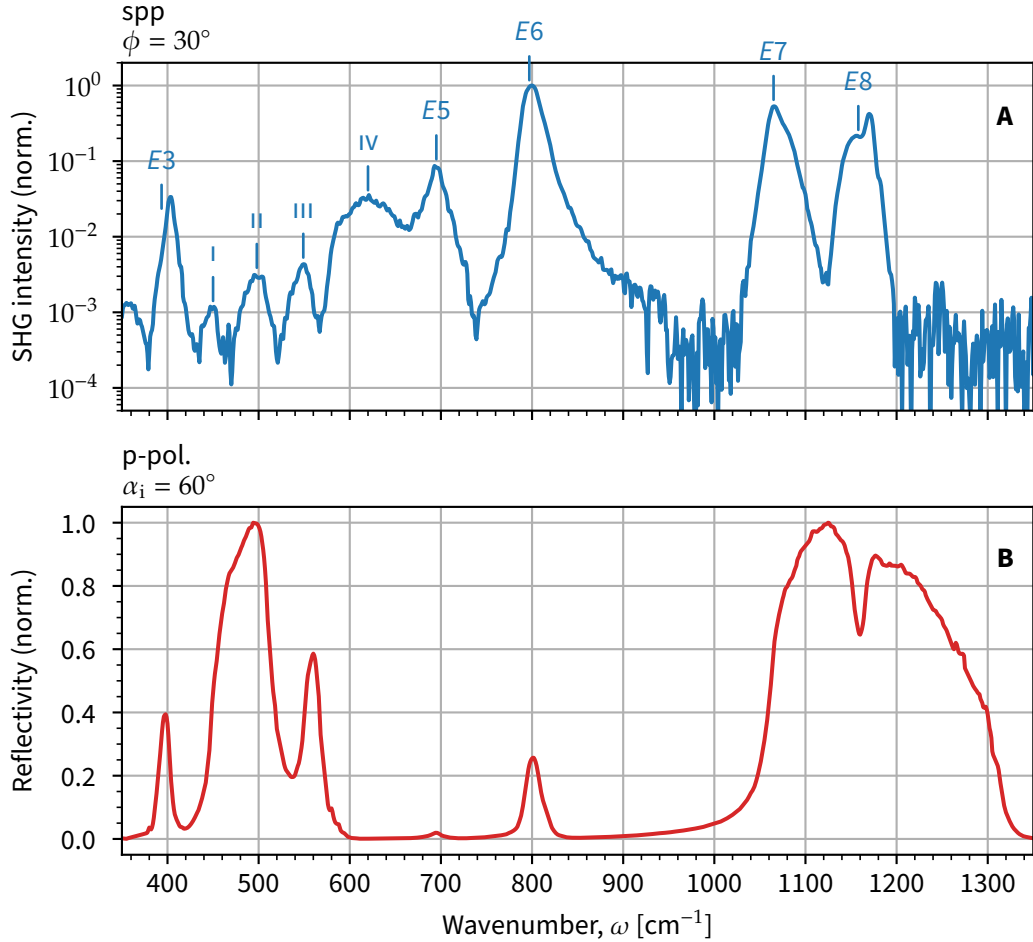
Figure 5.4. Experimental SHG and reflectivity spectra of α-quartz at room temperature. A: Strongly enhanced SHG signals are observed at TO phonon frequencies. **B:** Reflectivity spectrum in *p*-polarization and at an incidence angle $\alpha_i = 60°$. Regions of high reflectivity clearly mark Reststrahlen bands.

indicated by blue markers. These strong enhancements are primarily due to a combination of resonances in the nonlinear susceptibility, $\chi^{(2)}(\omega)$ (Eq. 3.3.7), as well as in the local field amplitudes which enter in form of Fresnel transmission factors, $L(\omega)$ (Sec. 3.2.3), and the wave vector mismatch, $\Delta k(\omega)$ (Eq. 5.1.4). The interplay of these highly dispersive quantities is essential to IR SHG as a phonon spectroscopy and will be discussed in detail later on. Spectral features between $445\,\mathrm{cm}^{-1}$ and $620\,\mathrm{cm}^{-1}$, labeled I–IV, cannot be unambiguously attributed to *E*-type phonon modes due to their very low signal levels and unusual temperature dependence which will be analyzed in Sec. 5.3. Unlike the TO phonon resonances, LO modes cause merely subtle signatures in the SHG response as will be argued below when quantitatively analyzing the SHG spectrum.

Simultaneously, reflectivity spectra were acquired in *p*-polarization at an incidence angle of $\alpha_i = 60°$ as shown in Fig. 5.4B. Here, spectral regions of particularly

Table 5.2. **Fit parameters from all acquired *spp* azimuthal scans.** Quantitative knowledge of the Fresnel transmission coefficients allows extraction of the $\chi^{(2)}$ ratio.

Label	ω [cm^{-1}]	$\left|\chi^{(2)}_{acb}\right|/\left|\chi^{(2)}_{aaa}\right|$
E3	400	0.186±0.014
E5	690	0.22±0.05
E6	795	1.46±0.19
E7	1069	2.6±0.3
E8	1171	0.11±0.08
I	445	0.32±0.05
II	498	30±4
III	545	2.5±1.2
IV	620	0.654±0.014

high reflectivity reveal α-quartz's Reststrahlen bands between corresponding TO and LO phonon frequencies where the real part of the dielectric function takes on negative values, resulting in strongly attenuated evanescent waves (Sec. 3.2.1). Here, modes with small TO–LO frequency splittings, i.e., small oscillator strengths [46], do not form full Reststrahlen bands, but rather peak-like reflectivity features.

Additionally, the SHG anisotropy behavior, i.e., azimuthal dependence, at all resonances marked in Fig. 5.4A has been measured under two polarization conditions: *spp* and *ppp*. Exemplarily, Fig. 5.5 shows the azimuthal scans at spectral positions marked E3, E6, E7, and E8. Here, model fits using Eqs. 5.1.3a and 5.1.3b are in very good agreement with the experimental data. While in the *spp* polarization configuration, the azimuthal scans depend on both uniquely contributing $\chi^{(2)}$ tensor elements, $\chi^{(2)}_{aaa}$ and $\chi^{(2)}_{acb}$, *ppp* scans solely depend on $\chi^{(2)}_{aaa}$. This leads to the observed three- and sixfold azimuthal dependencies, respectively, as expected from theory. Knowledge of α-quartz's Fresnel factors (Sec. 3.2.3) allows the extraction of relative $\chi^{(2)}$ magnitudes, i.e., the ratio $\left|\chi^{(2)}_{acb}\right|/\left|\chi^{(2)}_{aaa}\right|$, from *spp* scans. The fit results are summarized in Tab. 5.2.

Notably, the azimuthal behavior of the E6 mode in *ppp* polarization is highly sensitive to slight misalignment of the detection polarizer which would lead to an interference of the *s*- and *p*-polarized SHG components. Due to the relatively large anisotropic component entering the *spp* signal at this particular phonon resonance ($\propto L^{\text{eff}}_{acb}\chi^{(2)}_{acb}$, cf. Eq. 5.1.3a) and a generally stronger SHG signal for *spp* compared to *ppp*, a small polarization angle offset in detection has a considerable impact on the measured azimuthal dependence. At the E6 resonance, this effect is particularly pronounced because the *spp* signal is nonzero at angles where *ppp* also yields signal. For this reason, particular care had to be taken when adjusting
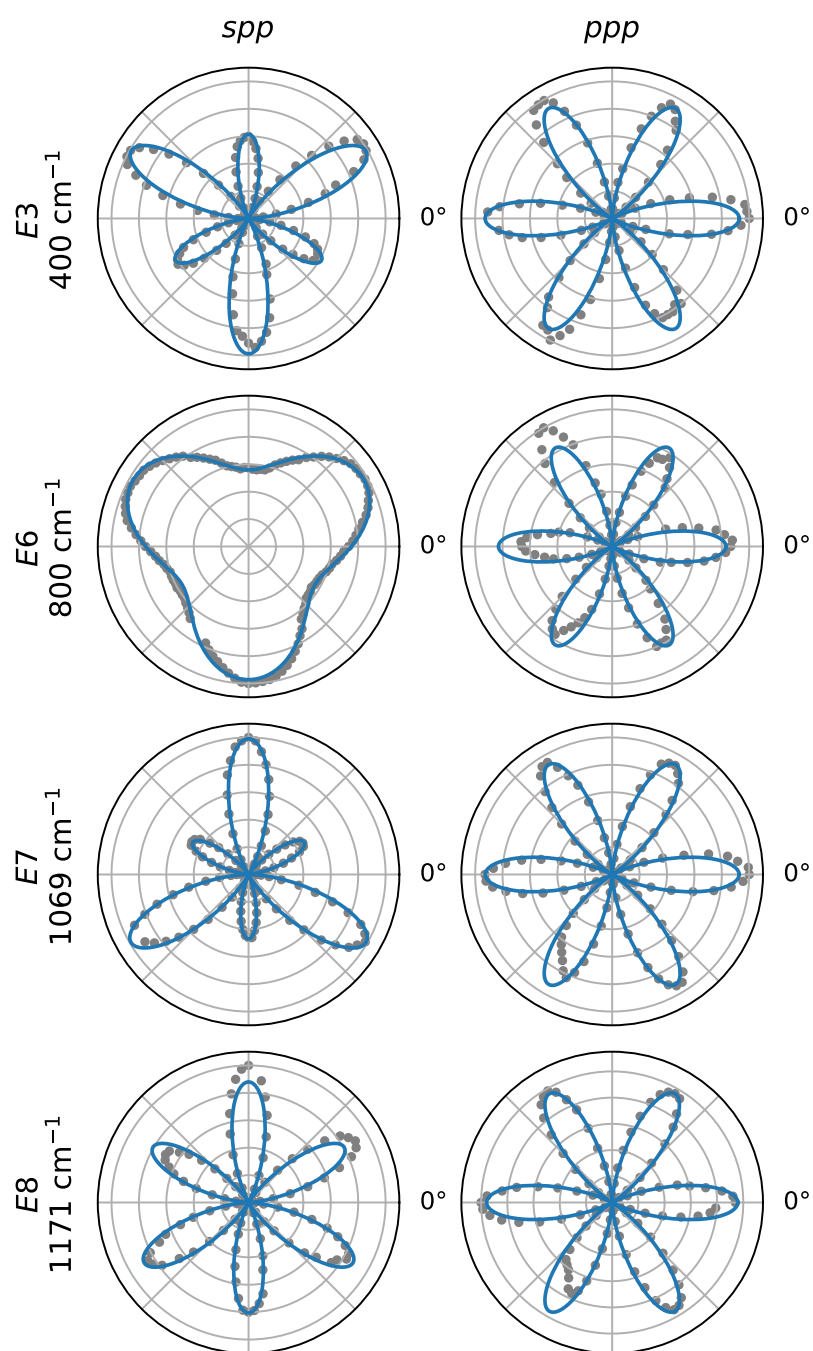
Figure 5.5. **Azimuthal dependence of the SHG intensity at four exemplary TO phonon resonances in *spp* and *ppp* polarization.** Gray dots represent experimental data and solid lines model fits using Eqs. 5.1.3a and 5.1.3b. While *ppp* measurements exhibit a sixfold symmetry, *spp* measurements show a threefold symmetry due to two contributing $\chi^{(2)}$ components.

the polarization of the detected SHG beam. This effect is much less pronounced at the other phonon resonances as *spp* signals are zero where *ppp* signals are strongest.

Quantitative Analysis

The physical origin of the observed SHG enhancements in Fig. 5.4 is threefold. First, the highly dispersive second-order nonlinear susceptibility, $\chi^{(2)}(\omega)$, typically peaks at TO phonon frequencies, causing a strong SHG enhancement over several orders of magnitude [75]. Secondly, the SHG signal is strongly modulated by the dispersing Fresnel factors, $L_{acb}^{\text{eff}}(\omega)$ and $L_{aaa}^{\text{eff}}(\omega)$ (cf. Eq. 5.1.3a). Lastly, the wave vector mismatch, $\Delta k(\omega)$ (see Eq. 5.1.4), is highly dispersive and determines the effective escape depth of the SHG light, $\delta_p = 1/\Delta k$. For nonabsorbing materials in a reflective geometry, δ_p is typically on the order of half the SHG wavelength and thus largely nondispersive. Here however, Δk^2 is highly dispersive due to the strong absorption of TO phonons which causes a large imaginary part of $\mathbf{k}_{1,2}^{\text{t}}$, dominating Δk^2.

Considering α-quartz's numerous phonon modes, the generalized model of Flytzanis (Eqs. 5.1.5a and 5.1.5b) results in a very large number of free fit parameters, $C_{1,2,3}^{j,k}$, making a quantitative analysis of the SHG spectra a challenging task. In order to achieve a feasible fit routine, we simplify the generalized model to include only C_1 terms as well as cross-terms in C_3 which contain spectrally proximate phonon resonances, assuming those to be the main contributors to the $\chi^{(2)}(\omega)$ function. This leaves a reduced number of 19 independent C_1 and C_3 coefficients as free fit parameters. This strongly simplified model, applied to Eqs. 5.1.3a and 5.1.4, while lacking quantitative accuracy, reproduces nearly every feature observed in the SHG spectrum qualitatively as shown in Fig. 5.6A. Moreover, from this analysis it is possible to extract the essential spectral shapes of the two contributing $\chi^{(2)}(\omega)$ functions which are plotted in Fig. 5.6B.

Fig. 5.6 illustrates the interplay of all dispersing contributions to the SHG signal, including the Fresnel factors (Fig. 5.6C) as well as the wave vector mismatch (Fig. 5.6D). Taking the *E7* mode as an example, it becomes clear how compensating enhancement and suppression effects are at play: Fresnel contributions and wave vector mismatch cause a significant suppression of the SHG signal of about 10^{-3} and 10^{-1}, respectively. Meanwhile, the $\chi^{(2)}$ enhancement at Ω_7^{TO} of about 10^6 counters these effects, resulting in a measurable SHG resonance. Notably, the Fresnel factors can cause a spectral shift of the SHG peak position with respect to the actual phonon frequency. This is observed in *E3* where a Fresnel suppression acts on the SHG signal at Ω_3^{TO}. At the same time, both, Fresnel factors and wave vector mismatch enhance the signal at a slightly higher frequency, effectively causing a spectral offset between observed SHG peak position and actual phonon
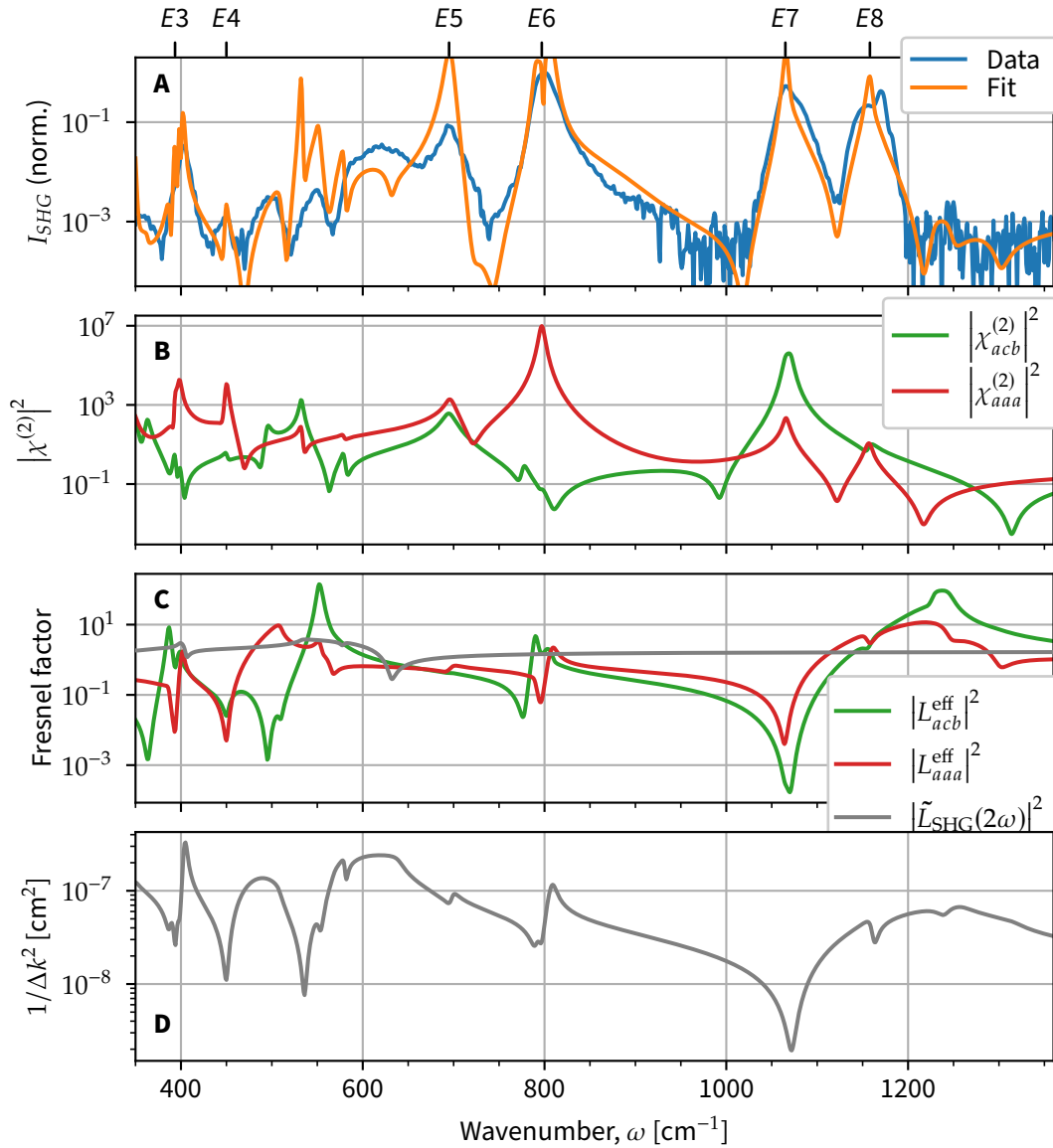
Figure 5.6. **Decomposition of the experimental SHG spectrum.** The highly dispersive $\chi^{(2)}$ tensor elements **(B)**, the Fresnel factors **(C)**, and the inverse squared wave vector mismatch **(D)** enter the fit to the experimental SHG data **(A)**. Note the logarithmic scales in all graphs.

frequency. This shows that an adequate interpretation of the SHG spectra requires a thorough treatment of the *linear* optical effects.

As mentioned above, only subtle signatures of LO phonon resonances are observed in the spectral SHG response. This stands in contrast to previous work on single-mode silicon carbide [75] and owes to a combination of effects. First, weaker modes, such as E-types $j = 5, 8$, reside on the tails of strong mode resonances in the dielectric function which strongly suppresses their Fresnel resonances at their LO frequencies. Secondly, out-of-plane Fresnel resonances (here, L_{zz}) are generally found to be stronger than in-plane resonances (here, L_{xx} and L_{yy}) as also seen in Fig. 5.6c. As we are largely sensitive to L_{xx} and L_{yy} for trigonal α-quartz (cf. Eqs. 5.1.3a and 5.1.3b), Fresnel resonance effects around LO phonon frequencies are reduced as compared to, e.g., hexagonal silicon carbide [75]. Nevertheless, peaks labeled $E3$, II, and $E6$ are—at least in part—likely to originate in LO phonon resonances.

5.3. High-Temperature SHG Spectra and Phase Transition

So far, we have analyzed the SHG phonon spectrum of α-quartz at room temperature. Due to its sensitivity to symmetry and vibrational resonances—carrying symmetry information themselves—SHG spectroscopy holds great potential for the study of order-to-order phase transitions. In this section, we will explore the temperature-dependence of α-quartz's SHG response, particularly in view of its high-temperature α–β phase transition. To this end, the sample was mounted onto a heating stage (Sec. 4.4.1). During this displacive phase transition at nominally $T_c = 846\,\text{K}$, quartz changes from the trigonal crystal symmetry to a hexagonal one (point group 622, Schoenflies D_6) [86]. Interestingly, E-type phonon modes labeled $j = 3, 5, 8$ become IR-forbidden in the β-phase due to structural changes in the crystal [87].

Experimental Results

Figs. 5.7a and c show SHG phonon spectra measured in the spp polarization configuration at temperatures 300 K, 500 K, 700 K, 875 K, and 950 K. Notably, the modes' different azimuthal behaviors (Fig. 5.5) would limit the dynamic range of some features in the SHG spectrum, e.g., $E3$ or $E7$, if taken at a single azimuthal angle. For this reason, SHG data were acquired in two parts: at $\varphi = 30°$ in the low-frequency region from $350\,\text{cm}^{-1}$ to $850\,\text{cm}^{-1}$ (Fig. 5.7a), and at $\varphi = 90°$ in the high-frequency range from $750\,\text{cm}^{-1}$ to $1350\,\text{cm}^{-1}$ (Fig. 5.7c).
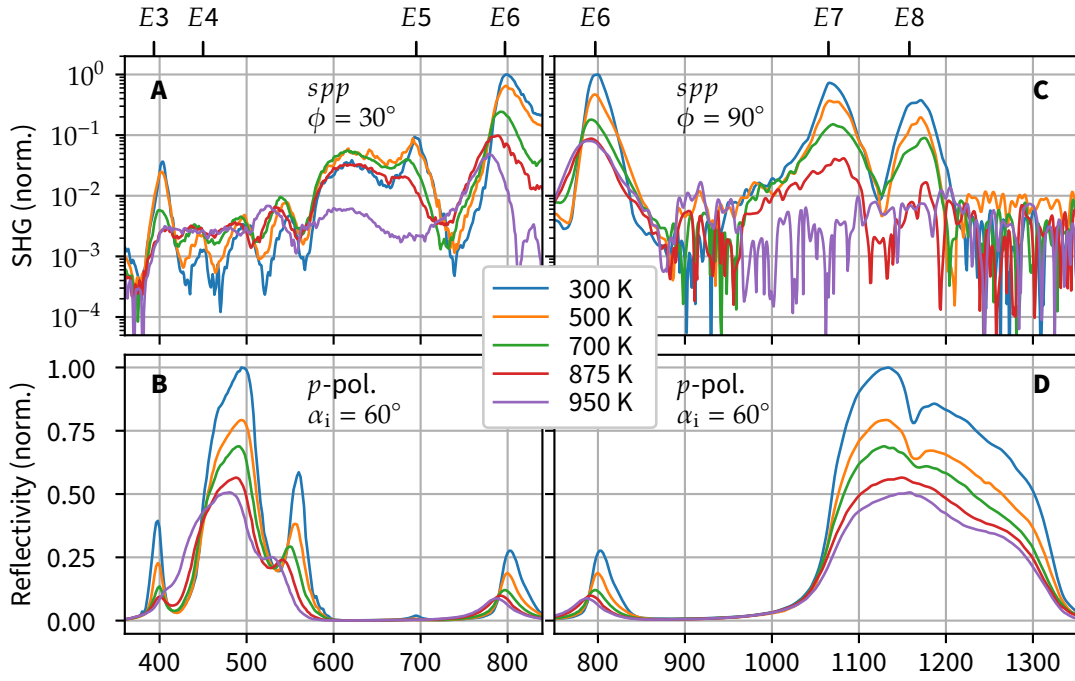
Figure 5.7. **Temperature-dependent SHG and reflectivity spectra of α-quartz.** Due to the different SHG azimuthal behaviors in the *spp* polarization configuration, these data were taken at φ = 30° in the low-frequency region **(A, B)** and at φ = 90° in the high-frequency region **(C, D)**. The SHG resonances decrease and broaden while center frequencies shift as temperature increases. Reflectivity spectra were taken at an incidence angle α_i = 60° and in *p*-polarization. Note the logarithmic scale in **A** and **C**.

The temperature-dependent spectra reveal two immediate observations. First, a clear decrease of the resonant amplitudes, in terms of SHG peak heights, as well as increased damping rates, in terms of peak widths, are observed at higher temperatures. Secondly, SHG peak positions shift with temperature. This behavior originates from temperature-dependent changes of the phonon damping rates and frequencies. Remarkably, some TO phonon resonances exhibit a particularly sudden drop in SHG intensity close to the phase transition temperature T_c = 846 K, most prominently *E*5. Other resonant features, in contrast, show a gradual decrease up to the highest measured temperature—*E*6 for instance—or until the SHG signal drops below the detection limit, such as *E*7. This behavior is most likely due to the α–β phase transition where phonon modes associated with *E*3, *E*5, and *E*8 become IR-forbidden while *E*6 and *E*7 remain IR-active [86].

The simultaneously measured reflectivity spectra are shown in Figs. 5.7B and D. In accordance with the SHG peaks, Reststrahlen edges and peaks in the reflectivity soften and shift spectrally with increasing temperature. Close to the phase transition temperature, peak-like features associated with *E*-type modes $j = 3, 5$ disappear almost entirely, as does the dip-like feature in the upper Reststrahlen band associated with the $j = 8$ mode, thereby being consistent with the SHG data.

Note that the reflectivity data are displayed on a linear scale whereas SHG spectra are plotted logarithmically to cover the large dynamic range in these signals. This visual representation masks the fact that SHG peaks are much more sensitive to phonon damping than any of the reflectivity features.

Notably, SHG peaks labeled I–IV in Fig. 5.4 even intensify with increasing temperature. Here, the plateau-like feature labeled IV shows a peculiar behavior with a pronounced signal drop above the phase transition temperature. These observations are interesting and not entirely understood at this point. It should be noted, however, that during the measurements a signal contribution due to black-body radiation by FEL-induced sample heating has been observed. This effect gets more pronounced at elevated temperatures and has been accounted for by subtracting background spectra, acquired at a large time delay between the pulses in both excitation arms. Nevertheless, owing to the low signal levels in this frequency range, the possibility of a thermal contribution to the SHG signal cannot be ruled out entirely.

Analysis

For a quantitative analysis of the observed spectral features—especially at high temperatures—the observed SHG peak positions and widths are compared to temperature-dependent phonon data acquired through IR reflectivity measurements by Gervais and Piriou [86]. To this end, resonant features in the SHG spectra have been fitted with a Lorentzian function, yielding center frequencies and linewidths, ω^{SHG} and Γ^{SHG}, respectively, as well as amplitudes. Here, Γ^{SHG} is defined as the half width at half maximum (HWHM). These fit results are plotted in Fig. 5.8 together with the phonon data from Ref. 86.

The comparison shows how the TO phonon frequencies and damping rates relate to the observed peak characteristics in the SHG spectrum. In fact, the SHG peak positions mimic the temperature-dependent trends of their corresponding TO phonon frequencies considerably well, although offsets of up to $10\,\text{cm}^{-1}$ are observed, owing to the influence of Fresnel factors and the wave vector mismatch as discussed in Sec. 5.2. This is also true for the SHG peak labeled $E6$ which was measured at two azimuthal angles, $\varphi = 30°$ and $90°$, displayed as closed and open dots, respectively. Here, the two relevant Fresnel components, L_{acb}^{eff} and L_{aaa}^{eff}, each exhibiting different temperature dependencies, contribute differently to the SHG signal.

Remarkably, phonon damping rates are well represented by the SHG peak widths—in large parts even in good quantitative agreement with Γ^{SHG}. This is nontrivial as the SHG spectra are considerably modulated by the dispersing Fresnel factors, especially at phonon resonances. Yet, the data in Fig. 5.8A show
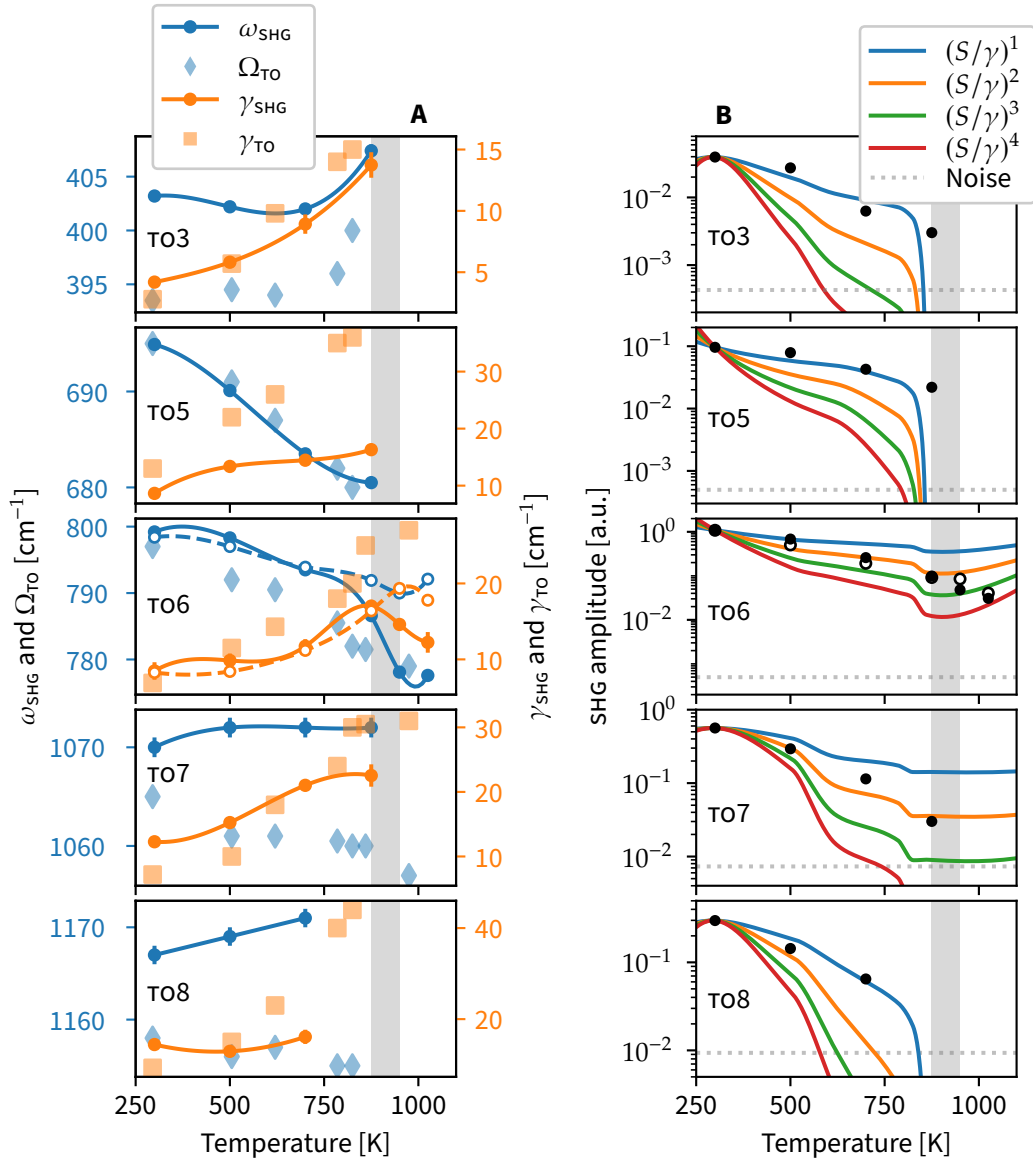
Figure 5.8. Temperature-dependent SHG peak characteristics. A: Fitted peak positions (blue) and damping rates (orange) from the experimental SHG spectrum (dots with error bars) compared to TO phonon frequencies and damping rates as measured in Ref. 86 (diamonds and squares, respectively). Lines are a guide to the eye. Quartz's phase transition presumably takes place in the temperature range indicated by the gray shaded area. **B:** Fitted SHG peak amplitudes at phonon resonances (black dots) with estimations of their temperature-dependent SHG behavior based on oscillator strengths and damping rates. For TO6 in **A** and **B**, closed and open dots correspond to data taken at φ = 30° and φ = 90°, respectively.

that the SHG peak widths provide a reasonable estimate of the phonon damping constants for all modes observed.

Fig. 5.8B shows the fitted SHG amplitudes. Clearly, the data show a continuous decrease of the SHG intensity with higher temperatures for all resonances. Above the phase transition temperature, all resonance amplitudes vanish with the exception of the $E6$ mode which—as its center frequency and linewidth—shows a kink-like behavior at the phase transition instead.

Attempting an estimation of the expected behavior of the resonant SHG amplitudes, the temperature-dependent amplitude of each phonon resonance is evaluated to S/γ where S denotes that phonon mode's oscillator strength (cf. Eq. 3.2.7) and γ its respective damping rate, using data from Ref. 86. As S/γ enters the Fresnel coefficients (Sec. 3.2.3) in terms of resonances in the dielectric function to different orders and, similarly, contributes to $\chi^{(2)}(\omega)$ (Eqs. 5.1.5a and 5.1.5b) both, linearly and quadratically, several powers $(S/\gamma)^N$ with $N = 1...4$ are plotted alongside the experimental data in Fig. 5.8B. Here, $(S/\gamma)^N$ is normalized to the room temperature data.

Below the phase transition temperature, the resonant amplitudes of $E3$, $E5$, and $E8$ follow the linear $N = 1$ curve, whereas $E6$ and $E7$ appear to decay more quickly. Close to the phase transition temperature—expected in the range marked by the gray shade in Fig. 5.8—S/γ rapidly drops to zero for the modes $E3$, $E5$, and $E8$ as these modes become IR-forbidden in the β-phase such that their oscillator strength, S, vanishes. In fact, no SHG signal is observed above T_c for these modes. For $E6$ and $E7$, on the other hand, S/γ predicts appreciable amplitudes above T_c as these modes persist in the β-phase. Experimentally, $E6$ is indeed observed above T_c whereas $E7$ also vanishes—contradicting the expectation. However, a careful examination of detection limits (dotted line in Fig. 5.8B) reveals that the resonant amplitude of $E7$ would, in fact, fall below noise level above T_c if it followed the same trend as $E6$, i.e., dropping more rapidly than the power law prediction in the β-phase. Strikingly, those modes which persist through the phase transition, exhibit a temperature-dependence distinct from the other modes, i.e., closer to $N = 2$, rather than $N = 1$. While this empirical observation is very interesting, it is at this point not possible to isolate a single cause for this effect due to the numerous contributions to the $\chi^{(2)}(\omega)$ lineshape.

Discussion

In general, a quantitative analysis of the SHG spectra turned out to be a challenging task—in particular for two interfering $\chi^{(2)}(\omega)$ contributions with many phonon resonances. This is the case for the data shown in Fig. 5.4A, resulting in such a large number of independent parameters that quantitative fitting is not feasible. With sufficient signal-to-noise, however, a possible solution to this problem could

be reached by utilizing the intrinsic symmetry properties of Eq. 5.1.3a. In Fig. 5.4, data were recorded at an azimuthal angle $\varphi = 30°$, i.e., at the maximum signal for many of the observed resonances (cf. Fig. 5.5). If, instead, SHG spectra could be acquired at $\varphi = 0°$, the contribution of $\chi^{(2)}_{acb}(\omega)$ could be probed exclusively, allowing a division by the linear quantities, L^{eff}_{acb} and Δk, to reveal the actual $\chi^{(2)}_{acb}(\omega)$ lineshape. Similarly, SHG spectra in ppp would grant access to the $\chi^{(2)}_{aaa}(\omega)$ lineshape. At room temperature, insufficient signal levels prohibit measurements in these configurations. However, considering the clear temperature trend of SHG signal levels observed in these experiments, measurements at low temperatures might very well allow such an approach. The following section deals with SHG phonon spectroscopy of α-quartz at cryogenic temperatures.

5.4. Low-Temperature SHG Phonon Spectroscopy

For the low-temperature measurements, the α-quartz sample was mounted inside a helium bath cryostat. Layout and details about the operation procedure of the cryostat are described in Sec. 4.4.2. Here, the c-cut sample was oriented at an azimuthal angle of $\varphi = 0°$ using the cryostat's integrated motorized rotation stage. Importantly, at $\varphi = 0°$, the expressions for the SHG intensity in the spp and ppp configurations (cf. Eqs. 5.1.3a and 5.1.3b), respectively, simplify to:

$$I^{spp}_{\text{SHG}}(2\omega) \propto \underbrace{\left|\tilde{L}_{\text{SHG}}(2\omega)\left[L_{zz}(\omega, \alpha^{\text{i}}_1)\, L_{xx}(\omega, \alpha^{\text{i}}_2) + L_{xx}(\omega, \alpha^{\text{i}}_1)L_{zz}(\omega, \alpha^{\text{i}}_2)\right]}_{\equiv L^{\text{eff}}_{acb}} \chi^{(2)}_{acb}(\omega, \omega)\right|^2/\Delta k^2,$$

$$(5.4.1a)$$

$$I^{ppp}_{\text{SHG}}(2\omega) \propto \underbrace{\left|\tilde{L}_{\text{SHG}}(2\omega)\, L_{xx}(\omega, \alpha^{\text{i}}_1)\, L_{xx}(\omega, \alpha^{\text{i}}_2)}_{\equiv L^{\text{eff}}_{aaa}}\, \chi^{(2)}_{aaa}(\omega, \omega)\right|^2/\Delta k^2. \qquad (5.4.1b)$$

In these expressions, contributions from $\chi^{(2)}_{acb}$ and $\chi^{(2)}_{aaa}$ do not interfere in each of the measurements, allowing for an isolation of the $\chi^{(2)}$ lineshapes through division by the contributing linear quantities, namely the Fresnel coefficients and the wave vector mismatch. Notably, at room temperature, measurements at $\varphi = 0°$ were not feasible due to insufficient signal levels in spp—with one out of two $\chi^{(2)}$ contributions effectively being switched off—and generally poor SHG yield in ppp. At cryogenic temperatures, on the other hand, decreased damping rates and, hence, sharper SHG resonances, may enable these measurements.

Such an approach, however, requires good knowledge of α-quartz's low-temperature dielectric function which fully determines the linear signal contributions. Since at the time of these experiments no study of α-quartz's IR dielectric

function at cryogenic temperatures could be found in the literature,[3] a series of linear reflectivity measurements had to be conducted in order to determine the temperature dependence of $\varepsilon(\omega)$ below room temperature. A comprehensive description of this experiment as well as a thorough analysis and discussion of its results will follow in Sec. 5.5. For now, α-quartz's dielectric function at cryogenic temperatures is assumed to be given.

Experimental Results

The SHG spectra in *spp* and *ppp* polarization at $\varphi = 0°$ and $T = 1.5\,\mathrm{K}$ in the lower and upper Reststrahlen region of α-quartz were acquired in separate FEL beamtimes and are shown in Fig. 5.9A. Clearly, the low-temperature SHG spectra reveal distinct features and resonances, even for these low-signal configurations. Considering the observed noise levels, however, it becomes apparent that the signal magnitudes of some SHG resonances surpass the noise floor by only a relatively narrow margin (less than one order of magnitude). This observation suggests that weaker resonances—despite the decreased damping rates at low temperatures—may still fall below the detection limit.

With the aid of α-quartz's low-temperature dielectric function at $1.5\,\mathrm{K}$ (see Sec. 5.5), the linear contributions to the experimental SHG spectrum can be straightforwardly calculated (see Sec. 3.2.3). The relevant Fresnel factors (cf. Eqs. 5.4.1a and 5.4.1b) as well as the inverse wave vector mismatch for both measurements are shown in Fig. 5.9B and C, respectively. Dividing the experimentally measured SHG signal by these linear quantities finally yields the (absolute squared) lineshapes of α-quartz's uniquely contributing nonlinear susceptibility elements, i.e., $\left|\chi_{acb}^{(2)}(\omega)\right|^2$ and $\left|\chi_{aaa}^{(2)}(\omega)\right|^2$. These are shown in Fig. 5.9D.

Discussion

Upon closer inspection of the interplay between the linear quantities and the extracted nonlinear $\chi^{(2)}$ contributions (Fig. 5.9), it becomes clear that the signal-to-noise ratio encountered in these measurements does not allow for a reliable determination of the $\chi^{(2)}(\omega)$ lineshapes over the entire Reststrahlen region. This is apparent, for instance, in the lower spectral range between $410\,\mathrm{cm}^{-1}$ and $510\,\mathrm{cm}^{-1}$. Here, calculations of both linear contributions, $\left|L^{\mathrm{eff}}\right|^2$ and $1/\left|\Delta k\right|^2$, predict a strong suppression at $454\,\mathrm{cm}^{-1}$, i.e., the $j = 4$ E-type phonon frequency, for both polarization configurations. As a consequence, the extracted $\chi^{(2)}(\omega)$ lineshapes reveal a considerable enhancement at Ω_{TO_4}, although no resonant information is present

---

3 The only reported low-temperature study of α-quartz's dielectric function was limited to terahertz frequencies [88].
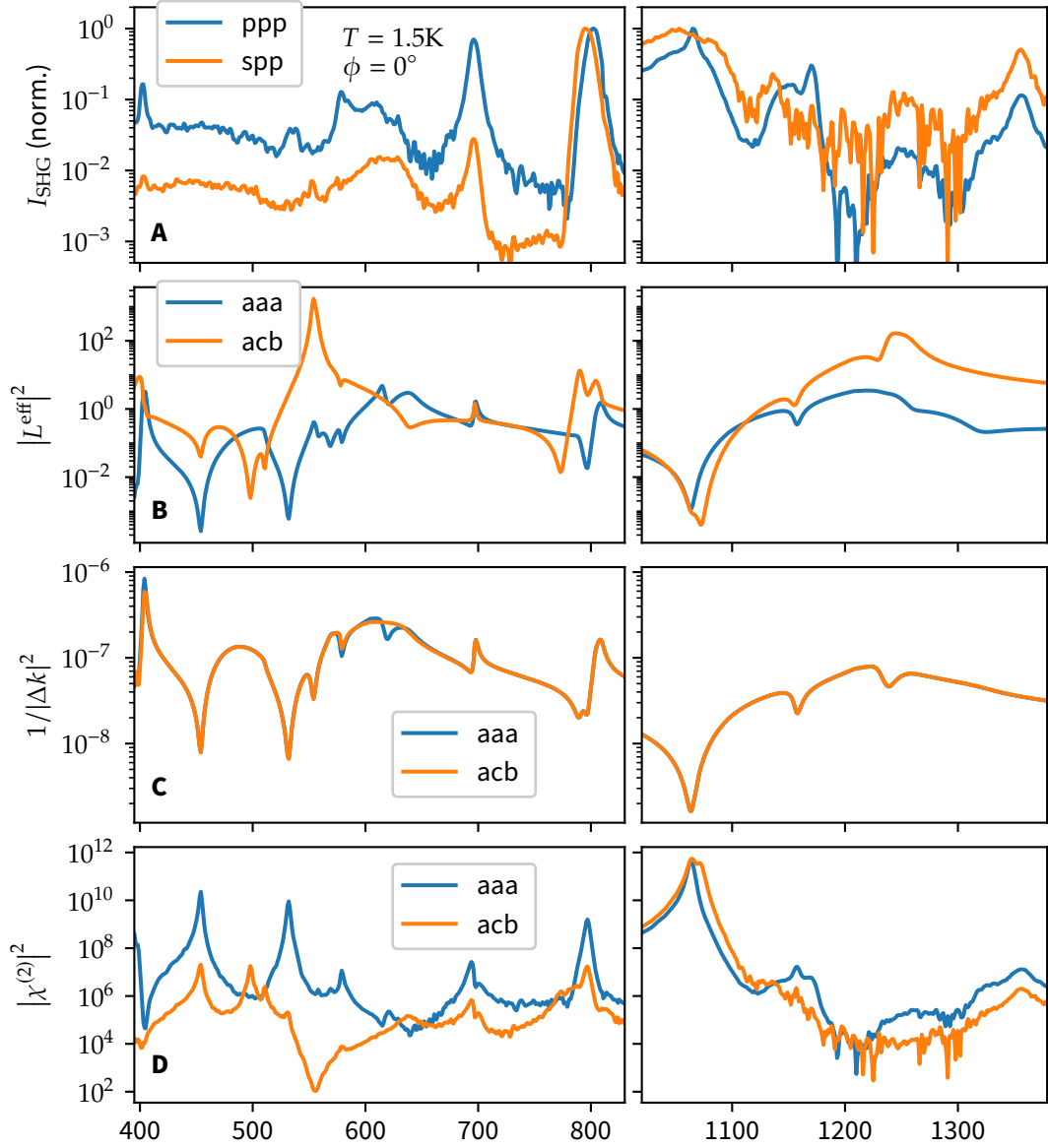
Figure 5.9. **Composition of α-quartz's low-temperature SHG spectra.** SHG spectra in *spp* and *ppp* polarization conditions at φ = 0° and T = 1.5 K **(A)**. These measurement configurations allow to isolate the two unique $\chi^{(2)}$ contributions. Division by the effective Fresnel coefficients **(B)** and the wave vector mismatch **(C)** allows to extract the respective $\chi^{(2)}(\omega)$ lineshapes **(D)**.

in the experimental data which, at that frequency, simply shows noise. Thus, the extracted enhancement in $\chi^{(2)}$ is an artifact of the relatively high noise floor.

Possible reasons for the insufficient signal levels—despite the sharper resonances at low temperatures—are twofold. One obvious experimental reason are the multiple additional transmissive optics introduced to the beam path by the cryostat. The two IR excitation beams each have to pass two KRS-5 and one diamond window, totaling in a reduced transmission of about a factor of 3. Roughly the same intensity loss is inflicted on the generated second-harmonic beam before reaching the detector. This effect can be partly compensated by making use of the full FEL power which—thanks to the extremely effective LHe-cooling—does not provoke sample damage.

A second possible reason for the relatively weak SHG response at resonance may, however, be of physical nature and intrinsic to the decreased damping rates at low temperatures. While low damping rates cause sharper and more intense resonant enhancements in $\chi^{(2)}(\omega)$, likewise resonances in the dielectric function, $\varepsilon(\omega)$, are amplified. These, in turn, directly increase the effect of the linear signal contributions, in particular the Fresnel factors which typically cause a suppression of the SHG signal on resonance—as observed in the room temperature data (cf. Fig. 5.6). This circumstance diminishes the effective signal-to-noise advantage gained by the lowered damping rates.

In conclusion, the attempt to employ SHG phonon spectroscopy at low temperatures in order to determine isolated $\chi^{(2)}(\omega)$ lineshapes—inaccessible at room temperature—was partially successful. Stronger SHG resonances produce appreciable signal, allowing for an estimation of $\left|\chi^{(2)}\right|$ magnitudes on these resonances. However, insufficient signal levels prevent detection of weaker resonances and therefore a full extraction of the $\chi^{(2)}(\omega)$ lineshapes over the entire Reststrahlen region. The latter would then enable a line fit using the generalized Flytzanis model (Eqs. 5.1.5a and 5.1.5b) and—due to the greatly simplified fit procedure—possibly even an extraction of anharmonic phonon mode coupling parameters (see Sec. 5.1). A conceivable route to improve the sensitivity in this setup may be the use of a LHe-cooled bolometer in place of the current MCT detector [89].

Apart from α-quartz's nonlinear properties, such as lattice anharmonicities which are, in principle, accessible through SHG phonon spectroscopy, its *linear* optical properties are of prevailing relevance as well—not least because a thorough analysis of nonlinear spectra requires detailed knowledge of the system's linear optical behavior, as clearly seen in this section.

A material's linear properties might be of considerable scientific interest in their own right. This is particularly true for α-quartz. In this regard, the following section deals with α-quartz's dielectric properties at low temperatures which have

already been used in this section, and explores a particularly interesting material property which has not been discussed so far: its natural hyperbolicity.

## 5.5. Low-Temperature Dielectric Function of Hyperbolic α-Quartz

The Reststrahlen region of the uniaxial crystal α-quartz naturally features hyperbolicity, i.e., its diagonal permittivity tensor has both, positive and negative principal components, such that $\mathrm{Re}(\varepsilon_\parallel)\,\mathrm{Re}(\varepsilon_\perp) < 0$ [90, 91] (see Sec. 3.2.2). The resulting isofrequency surfaces in momentum space resemble open hyperboloids—as opposed to, e.g., closed spheres for isotropic media—and thus support high-k waves [53, 92–95]. These states of light, thanks to their high spatial frequency, can be utilized in nanophotonic devices for, e.g., subdiffractional imaging or nano-lithography using so-called *hyperlenses* [96, 97]. Moreover, α-quartz exhibits both, type I and type II hyperbolic bands in close spectral proximity, adding to its design flexibility for nanophotonic applications.

Despite these intriguing properties, low-temperature studies of α-quartz's dielectric function have been limited to the terahertz range [88] prior to this work. Above room temperature, Gervais and Piriou performed an extensive IR reflectivity study on α-quartz which allowed a determination of the high-temperature dielectric function and served as reference in Secs. 5.2 and 5.3. In the following, an experimental study of α-quartz's IR dielectric function at low temperatures is presented, ranging from 1.5 K to 200 K, with a particular focus on its pronounced hyperbolicity.

5.5.1. Low-Temperature Dielectric Function

For an experimental determination of the dielectric function, we follow Gervais' and Piriou's approach by acquiring a series of IR reflectivity spectra. For this purpose, we utilize the autocorrelator geometry of the SHG setup (Sec. 4.2) where, instead of the second-harmonic beam, *both* reflected fundamental beams, incident at 30° and 60°, are detected by two pyroelectric photodetectors.

The sample studied here is an optically polished α-quartz y-cut single crystal (MaTecK), i.e., with the optic c-axis parallel to the surface plane. This arrangement allows both, the ordinary E-type and the extraordinary A_2-type IR-active phonon modes to be probed either exclusively or simultaneously—depending on the orientation of the c-axis which can be adjusted via the sample's azimuthal angle and the FEL beam polarization. Sample cooling is achieved using the helium bath cryostat described in Sec. 4.4.2.
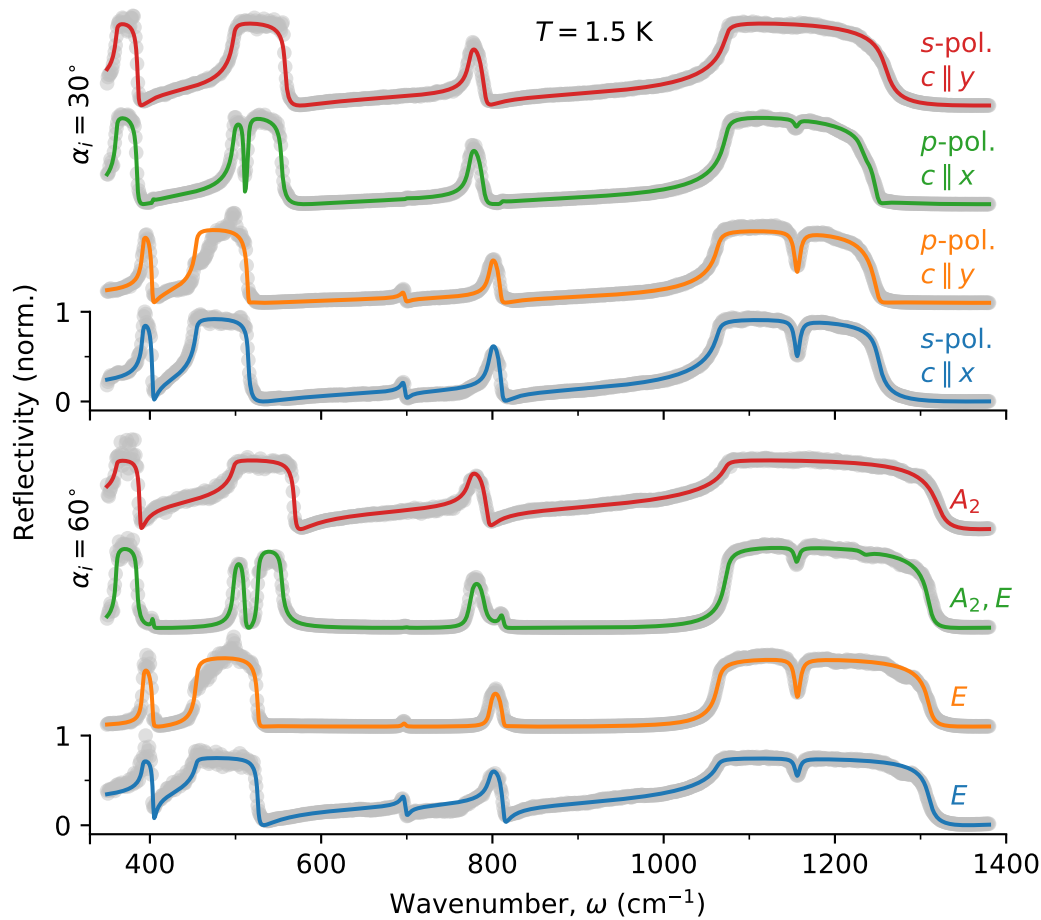
Figure 5.10. **Experimental reflectivity spectra of α-quartz at 1.5 K.** Model fits (solid curves) are in good agreement with the experimental data (gray dots). Depending on the configuration, the measurements are either exclusively sensitive to ordinary E-type modes (blue and orange), the extraordinary A_2-type modes (red), or both (green).

Experimental Results

In this measurement series, spectra in all possible combinations of the sample's c-axis orientation (vertical and horizontal), the FEL beam polarization (p and s), and the incidence angle (30° and 60°) were acquired at four temperatures: 1.5 K, 20 K, 100 K, and 200 K. Exemplarily, Fig. 5.10 shows the experimental reflectivity data for all geometries and both incidence angles at T = 1.5 K. As in Fig. 5.4, Reststrahlen bands are very pronounced, especially for phonon modes with large TO–LO splittings, i.e., high oscillator strengths [46]. Each measurement configuration, i.e., p- or s-polarization with horizontal or vertical c-axis orientation, results in a specific direction of the IR electric fields with respect to the principal crystal axes and thus probes either one of the two unique dielectric tensor elements, $\varepsilon_\perp$ and $\varepsilon_\parallel$, exclusively, or both simultaneously. For instance, s-polarized reflectivity,

with $c \parallel x$ as well as p-polarized reflectivity with $c \parallel y$ (blue and orange curves in Fig. 5.10, respectively) are exclusively sensitive to the ordinary E-type modes and hence solely probe $\varepsilon_\perp$. Similarly, s-polarized reflectivity with $c \parallel y$ (red curve) probes the extraordinary A_2-type modes, thus $\varepsilon_\parallel$. Comparing these spectra of exclusive sensitivity to $\varepsilon_\perp$ and $\varepsilon_\parallel$ (e.g., blue and red curves in Fig. 5.10, respectively) reveals α-quartz's pronounced uniaxial anisotropy as a result of different numbers of IR-active modes and significant frequency shifts among its principal axes. On the other hand, p-polarized reflectivity with $c \parallel x$ (green curve) is sensitive to *both* principal components. This becomes apparent as the reflectivity spectra show features attributable to both, E- and A_2-type modes, the former being more pronounced for the rather grazing 60° incidence angle, i.e., for a larger incoming out-of-plane field component.

Data Fitting

For a theoretical description of the acquired data, we can readily invoke the Fresnel reflection coefficients derived in Sec. 3.2.3 (see Tab. 3.1). Here, all dispersive quantities are ultimately dependent on the dielectric tensor elements, $\varepsilon_\perp(\omega)$ and $\varepsilon_\parallel(\omega)$, which themselves are well-described by the FPSQ model (see Eq. 3.2.12). Finally, the p- and s-polarized reflected light intensities are, respectively, given by:

$$I_p = |R_{xx} E_i \cos \alpha_i|^2 + |R_{zz} E_i \sin \alpha_i|^2 \,, \tag{5.5.1}$$

$$I_s = \left|R_{yy} E_i\right|^2 \,, \tag{5.5.2}$$

where R_{xx}, R_{yy}, and R_{zz} denote the Fresnel reflection tensor elements (Tab. 3.1) and E_i the incident electric field. This leaves the TO and LO phonon frequencies, Ω_{TO_j} and Ω_{LO_j}, their respective damping rates, γ_{TO_j} and γ_{LO_j}, as well as the high-frequency contributions, $\varepsilon_{\infty_\perp}$ and $\varepsilon_{\infty_\parallel}$, as the only independent variables entering the model through the FPSQ equation (Eq. 3.2.12). The experimental data have been fitted using this model with a nonlinear least squares regression procedure applied globally to the entire data set for each temperature, yielding the frequencies and damping rates of both, E- and A_2-type phonon modes, as well as the high-frequency contributions, $\varepsilon_{\infty_\perp}$ and $\varepsilon_{\infty_\parallel}$, as fit results.

It should be noted that the FPSQ model can result in the imaginary part of the dielectric function, $\mathrm{Im}(\varepsilon)$, taking on negative values in case of large differences of the LO and TO phonon damping rates, $\Delta\gamma_j = \gamma_{\mathrm{LO}_j} - \gamma_{\mathrm{TO}_j}$ [43]. In order to avoid this unphysical regime of the model, a penalty to negative $\mathrm{Im}(\varepsilon)$ values is applied during the least-squares fitting routine.

The fits are in good agreement with the experimental spectra across the entire data set. Noticeable deviations can be observed in the lower frequency region

from $450\,\text{cm}^{-1}$ to $550\,\text{cm}^{-1}$ which are suspected to originate from two parasitic spectral contributions. First, the cryostat windows, although being wedged, cause a Fabry-Pérot-like spectral modulation on top of the measured raw data. This modulation happens to be particularly pronounced at the lower Reststrahlen region at $\alpha_i = 60°$ and becomes more prominent where signal levels are constantly high, i.e., in Reststrahlen bands. Secondly, CO_2 bending modes in air cause strong IR absorption peaks in this spectral region which is minimized by flooding the optical setup with N_2 gas. Both of these unwanted effects are being corrected for by measuring reference spectra in s- and p-polarization using a bare gold mirror as a nominally perfect IR-reflector in place of the sample and dividing the raw reflectivity spectra by their corresponding reference. Nevertheless, a certain spectral contribution remains and is observable in the corrected spectra. The modulations, however, do not have a strong influence on the fit procedure as positions and widths of Reststrahlen edges remain largely unaffected.

The resulting fit parameters from all measurements, i.e., E- and A_2-type phonon frequencies and damping rates, are summarized in Tab. 5.3. Here, damping rates falling below the FEL linewidth of $\Delta\omega \geq 2\,\text{cm}^{-1}$ are indicated as "<2.0". Values for $\varepsilon_{\infty\perp}$ and $\varepsilon_{\infty\parallel}$ are averages over all four measured temperatures as the values do not show any significant temperature dependence.

Discussion

The temperature dependence of the fit results specified in Tab. 5.3 is plotted in Figs. 5.11 and 5.12 together with the values determined by Gervais and Piriou who studied the dielectric properties of α-quartz at high temperatures [86]. Overall the low-temperature data from Tab. 5.3 are largely consistent with Gervais' and Piriou's previous work as the extension of the low-temperature results to the high-temperature values from Ref. 86 is rather gradual. Notably, the majority of modes still experience a significant decrease in damping rates below 295 K. In particular, the spectrally lower E-type $j = 3, 4$ and A_2-type $j = 1, 2$ modes which cause α-quartz's pronounced hyperbolicity, experience a reduced damping rate by nearly a factor of 2 as compared to room temperature.

In order to describe the temperature dependence of both, phonon frequencies and damping rates, we here employ a power law fit with the vertex at $T_c = 846\,\text{K}$ [98] to the entire temperature range, including Gervais' and Piriou's high-temperature data:

$$y_j(T) = \left| y_j(0\,\text{K}) + k\sqrt{T_c - T} \right|, \tag{5.5.3}$$

where, y_j denotes either the phonon frequency, Ω_j, or the damping rate, γ_j of the jth mode. The fitted curves are also plotted in Figs. 5.11 and 5.12 as solid

Table 5.3. Results for the low-temperature phonon mode frequencies and damping rates used as free parameters to fit the experimental reflectivity spectra. Values for ε_∞ have been averaged over all temperatures.

j	$T\,[\mathrm{K}]$	A_2-type modes				E-type modes			
		Ω_{TO_j}	γ_{TO_j}	Ω_{LO_j}	γ_{LO_j}	Ω_{TO_j}	γ_{TO_j}	Ω_{LO_j}	γ_{LO_j}
			$[\mathrm{cm}^{-1}]$				$[\mathrm{cm}^{-1}]$		
1	1.5	360.7	<2.0	384.8	<2.0				
	20	360.1	<2.0	384.8	<2.0		−		
	100	360.9	<2.0	384.3	<2.0				
	200	361.2	2.1	385.2	<2.0				
2	1.5	497.9	3.1	553.6	2.8				
	20	498.4	3.6	554.4	3.3		−		
	100	498.0	3.2	553.1	3.1				
	200	496.8	4.7	552.2	4.0				
3	1.5	773.7	5.4	789.9	6.3	391.5	<2.0	403.0	<2.0
	20	774.4	5.6	789.9	6.5	392.1	<2.0	402.8	<2.0
	100	774.1	5.8	789.9	7.1	391.9	<2.0	403.0	<2.0
	200	775.3	5.9	788.8	6.8	392.4	<2.0	402.8	2.6
4	1.5	1073.0	6.2	1238.7	12.4	454.0	2.6	510.5	<2.0
	20	1072.7	3.5	1241.2	11.2	452.4	3.4	510.4	2.3
	100	1072.8	4.9	1239.2	11.1	453.6	2.2	510.0	2.1
	200	1070.9	5.3	1239.6	11.5	451.2	4.0	508.8	2.8
5	1.5					695.9	4.9	698.4	4.0
	20			−		695.8	4.9	698.5	4.5
	100					696.0	4.2	698.1	3.9
	200					695.3	5.6	697.7	5.0
6	1.5					797.2	4.8	810.0	4.3
	20			−		797.2	4.4	810.2	5.0
	100					796.9	5.1	809.9	4.1
	200					796.5	6.0	809.1	5.2
7	1.5					1063.7	6.1	1230.7	8.2
	20			−		1062.9	6.3	1231.9	10.9
	100					1063.9	6.8	1231.2	12.0
	200					1063.0	7.1	1230.0	12.1
8	1.5					1157.2	6.2	1154.9	6.1
	20			−		1156.9	6.9	1154.4	6.2
	100					1157.0	6.2	1154.9	6.0
	200					1157.0	7.2	1154.8	6.3
			$\varepsilon_{\infty_\parallel} = 2.334$				$\varepsilon_{\infty_\perp} = 2.296$		
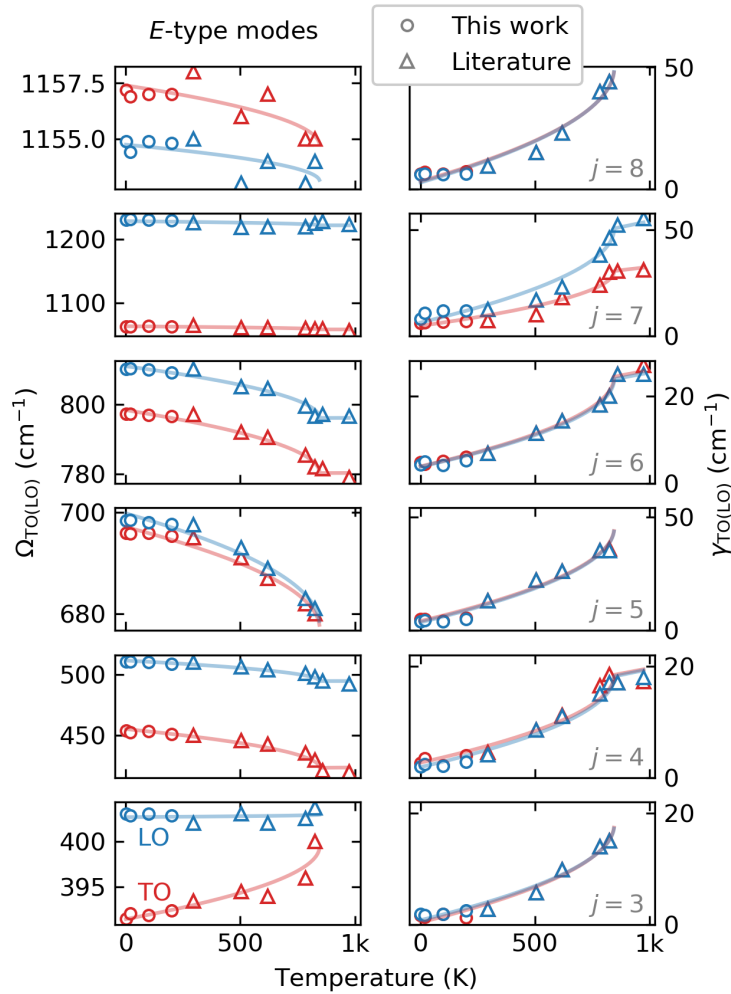
Figure 5.11. Thermal evolution of *E*-type phonon frequencies and damping rates.
Left: Phonon frequencies and **Right:** damping rates of the ordinary *E*-type phonon modes. Curve fits are indicated by solid lines. Literature values are taken from Ref. 86.

lines which describe the temperature-dependent behavior of $\Omega_j(T)$ and $\gamma_j(T)$ with good accuracy.

Having knowledge of the temperature-dependent phonon frequencies and damping rates, the dielectric functions, $\varepsilon_\perp(\omega)$ and $\varepsilon_\parallel(\omega)$ can now be straightforwardly calculated with the aid of the FPSQ model (Eq. 3.2.12). A fully parametrized and temperature-dependent dielectric tensor based on the power law fits to the data acquired in this work as well as Gervais' and Piriou's high-temperature data can be calculated using the Python Jupyter Notebook or MATLAB script supplied in Ref. 99. Notably, the validity of these scripts is restricted to the wavelength range studied here ($350\,\mathrm{cm}^{-1}$ to $1380\,\mathrm{cm}^{-1}$) as well as quartz's α-phase where the power law fits describe the data with high accuracy. This simple model, however, fails to describe the resonant behavior of damping rates at T_c and leads to instabilities of the FPSQ model above T_c.
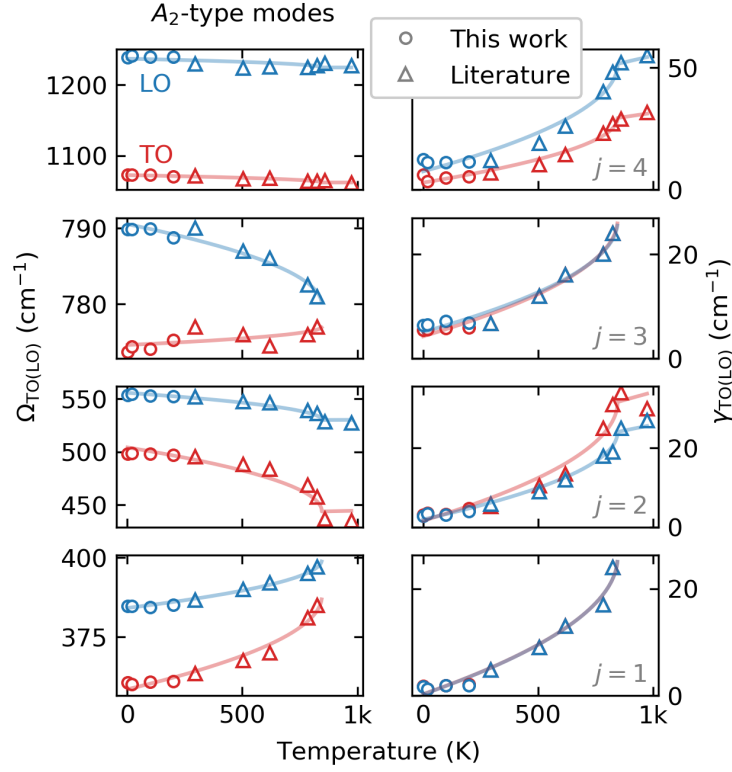
Figure 5.12. Thermal evolution of A_2-type phonon frequencies and damping rates.
Left: Phonon frequencies and **Right:** damping rates of the ordinary A_2-type phonon modes. Curve fits are indicated by solid lines. Literature values are taken from Ref. 86.

Exemplarily, the real and imaginary parts of $\varepsilon_\perp(\omega)$ and $\varepsilon_\parallel(\omega)$ are plotted at $T = 20\,\mathrm{K}$ in Fig. 5.13. Here, light and dark gray shades mark type I and type II hyperbolic bands, respectively. Especially in the lower spectral region, between $360\,\mathrm{cm}^{-1}$ and $550\,\mathrm{cm}^{-1}$, pronounced hyperbolic bands of both types emerge.

5.5.2. Natural Hyperbolicity in α-Quartz

In order to assess the suitability of these hyperbolic bands for nanophotonic applications, such as hyperlens designs, the quality factor, Q, is introduced as a figure of merit (FOM). It reads [100, 101]:

$$Q = \frac{\omega \frac{\mathrm{d}\,\mathrm{Re}(\varepsilon)}{\mathrm{d}\omega}}{2\,\mathrm{Im}(\varepsilon)}\Bigg|_{\varepsilon=-2.} \qquad (5.5.4)$$

For comparability, Q is determined in all hyperbolic bands in the lower spectral region between $361\,\mathrm{cm}^{-1}$ and $554\,\mathrm{cm}^{-1}$ at $\mathrm{Re}(\varepsilon) = -2$. This is in accordance with the common practice in the field of plasmonics where $\mathrm{Re}(\varepsilon) = -2$ marks the peak of the absorption in air due to a localized surface plasmon resonance [101]. Another important property of hyperbolic materials is the ratio $\varepsilon_\perp/\varepsilon_\parallel$ as it defines
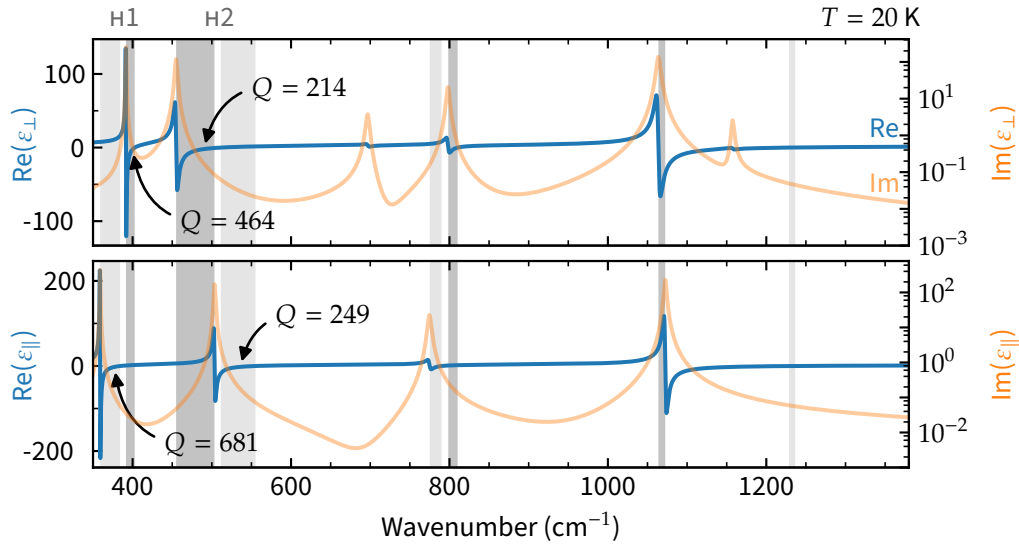
Figure 5.13. **Dielectric functions of α-quartz at 20 K.** Left axes (blue) indicate the real part of the dielectric functions while the right axes (orange) indicate their imaginary parts (on a logarithmic scale). Shaded areas mark type I (light gray) and type II (dark gray) hyperbolic bands. H1 and H2 refer to the two pronounced pairs of hyperbolic bands in α-quartz's lower spectral region. Q-factors are marked where Re(ε)=-2.

the rigid propagation direction of hyperbolic polaritons in the given material (see Eq. 3.2.16) and plays a crucial role in the design of, e.g., hyperlenses [93]. For this reason, Re($\varepsilon_{\perp(\parallel)}$) at Re($\varepsilon_{\parallel(\perp)}$) = −2 is evaluated alongside Q. Both FOMs are given in Tab. 5.4 for α-quartz (SiO$_2$) at 20 K and 300 K as well as hexagonal boron nitride (h-BN) for comparison. Hexagonal boron nitride has recently been subject to various studies, making use of its natural hyperbolicity and excellent Q-factors [93, 94, 101–104]. Here, we refer to h-BN as a benchmark system to evaluate α-quartz's potential for nanophotonic device applications.

The comparison shows that α-quartz offers very good Q-factors at low temperatures, surpassing those reported for h-BN at room temperature (see Tab. 5.4). It shall be noted, however, that reflectivity-based methods only offer limited sensitivity to the small off-resonance imaginary part of the dielectric function. Hence, Q-factors should be understood as estimates and a precise determination of the polariton performance requires a more direct measurement. The analysis also shows that α-quartz enables the high-k states characteristic for hyperbolic materials in a distinctly different spectral range, i.e., between 361 cm^{-1} and 554 cm^{-1}—as opposed to h-BN which exhibits type I hyperbolicity from 760 cm^{-1} to 825 cm^{-1} and type II hyperbolicity from 1360 cm^{-1} to 1614 cm^{-1}. Furthermore, α-quartz sustains both, type I and type II hyperbolic bands in close spectral proximity, opening up additional design opportunities for nanophotonic devices. Also in view of the hyperbolic polaritons' propagation directions—defined by the ratio

Table 5.4. Comparison of α-quartz's hyperbolic regions, H1 and H2, at 20 K and 300 K, with the naturally hyperbolic hexagonal boron nitride, comprising the parametrized TO and LO phonon frequencies, Q-factors at $\mathrm{Re}(\varepsilon) = -2$, and $\mathrm{Re}(\varepsilon_{\perp(\parallel)})$ where $\mathrm{Re}(\varepsilon_{\parallel(\perp)}) = -2$ for both principal crystal axes, based on the power law fits.

Material	α-quartz				h-BN [93]
	H1		H2		
T	20 K	300 K [86]	20 K	300 K [86]	300 K
$\Omega_\perp$ (cm^{-1}) TO	391.6	393.1	454.8	449.0	1360
LO	402.7	402.7	511.3	508.2	1614
$\Omega_\parallel$ (cm^{-1}) TO	358.9	364.3	503.4	492.2	760
LO	384.4	387.2	555.3	550.6	825
$Q_\perp$	464	87	214	91	221
$Q_\parallel$	681	69	249	76	399
$\mathrm{Re}(\varepsilon_\perp)\|_{\mathrm{Re}(\varepsilon_\parallel)=-2}$	11.0	11.9	1.1	0.9	8.0
$\mathrm{Re}(\varepsilon_\parallel)\|_{\mathrm{Re}(\varepsilon_\perp)=-2}$	2.2	2.2	15.0	23.9	2.8

$\varepsilon_\perp/\varepsilon_\parallel$—α-quartz offers additional flexibility as its lower pair of hyperbolic bands (indicated as "H1" in Fig. 5.13 and Tab. 5.4) exhibits similar properties as h-BN whereas band "H2" provides significantly different values while being in very close spectral proximity to H1. While the latter is also true at room temperature, Q-factors of hyperbolic polaritons experience a substantial improvement by at least a factor of 2 as compared to room temperature, promising superior performance of nanophotonic devices utilizing α-quartz's hyperbolicity at cryogenic temperatures.

5.6. Summary and Conclusion

This chapter introduced second-harmonic phonon spectroscopy as a highly sensitive tool for the study of phonon resonances in noncentrosymmetric polar crystals. Using α-quartz as a model system, it has been demonstrated that the crystal's IR-active TO phonon resonances cause steep enhancements in the SHG signal which can be detected across several orders of magnitude. The technique is facilitated by an IR FEL which provides the high peak fields and spectral sharpness required for such an approach. Unlike linear spectroscopies—such as the simultaneously acquired IR reflectivity—the nonlinear nature of IR SHG opens up additional experimental degrees of freedom which can be exploited through polarization control in order to selectively access symmetry-related information about the sample at hand. This becomes particularly apparent when investigating the SHG signal's

azimuthal behavior. Depending on the applied polarization configuration, either a six- or threefold symmetry is observed as either one or two interfering second-order nonlinear susceptibility tensor elements are probed, respectively.

Moreover, second-harmonic phonon spectroscopy is shown to be highly temperature-sensitive. As the sample temperature increases, phonon resonances shift spectrally and soften due to increased damping rates. Both of these effects are well-reproduced in the SHG phonon spectra in terms of peak positions and widths—largely in appreciable agreement with literature values. This is of particular interest in view of quartz's structural α–β phase transition where certain phonon modes become IR-inactive due to the heightened symmetry of the hexagonal β-phase. In fact, a sudden drop of SHG intensity is observed for these modes whereas one β-allowed mode shows a peculiar temperature dependence around T_c. This indicates a change in the crystal structure and promotes the technique's potential for the study of order-to-order phase transitions in general. This aspect will be picked up in Ch. 7 of this thesis.

While careful analysis of the SHG phonon peaks allows a largely accurate estimation of phonon frequencies and damping rates, a quantitative analysis of the spectral lineshapes turned out to be challenging. Here, a combination of both, linear quantities—determining the local fields—as well as the nonlinear susceptibility tensor elements—carrying information about, e.g., anharmonic mode coupling—determine the detected SHG intensity. Especially the latter introduces a plethora of free parameters due to the numerous resonances in α-quartz, rendering a quantitatively accurate fit procedure unfeasible. Additionally, the strongly temperature-dependent damping rates cause a rapid drop in SHG intensity at high-temperatures, further impeding a quantitative assessment above room temperature.

Attempting to overcome these limitations, experiments at cryogenic temperatures have been implemented and performed. Taking advantage of the lowered damping rates, it was possible to employ measurement configurations which involve only one $\chi^{(2)}$ tensor element and would not yield appreciable SHG signal at room temperature, e.g., ppp or spp at $\varphi = 0°$. Due to the relative simplicity of these spectra, it is in principle possible to extract $\chi^{(2)}(\omega)$ lineshapes by dividing out the linear spectral contributions. While this approach allows to estimate $\chi^{(2)}$ magnitudes on stronger resonances, the experimental setup still lacks the sensitivity required for a complete determination of their lineshapes across the entire spectral range.

In general, a careful quantitative analysis of the SHG phonon spectra requires good knowledge of the linear signal contributions, determined by the sample's dielectric IR response. While α-quartz's dielectric properties are well-studied at room-temperature and above, at the time these experiments were performed no

report of its low-temperature dielectric ɪʀ response was found in the literature. For this reason, and to enable an interpretation of the low-temperature sʜɢ phonon spectra, a series of ɪʀ reflectivity spectra were acquired. A global fit procedure of the experimental data allowed an extraction of α-quartz's phonon properties and thus its in-plane and out-of-plane dielectric functions between 1.5 K and 200 K. Here, a careful analysis of the strongly anisotropic dielectric response revealed multiple spectral bands of pronounced hyperbolicity. It is shown that at low temperatures, these hyperbolic bands exhibit remarkably high quality factors, presenting α-quartz as a promising naturally hyperbolic material and a viable candidate for nanophotonic applications.

While naturally hyperbolic materials, such as α-quartz, provide a straightforward way to sustain hyperbolicity, they often lack flexibility, e.g., in the applicable wavelength range since phonon frequencies and, hence, their ɪʀ dielectric response are material properties and as such hardly tunable. In this regard, metamaterial approaches offer a welcome alternative as these allow to purposefully alter the dielectric properties, for instance by varying geometrical parameters of the system or the constituent materials themselves [96]. The following chapter discusses the use of atomic-scale superlattices composed of polar semiconductors as a platform for tunable ɪʀ nanophotonic materials.

Chapter 6.

Controlling the Infrared Dielectric Function through Atomic-Scale Heterostructures

Large parts of this chapter have been published in Ref. 105. The text strongly draws from this publication.

The field of nanophotonics focuses on the confinement and manipulation of light at the nanoscale. While in the visible spectral range, this can for instance be achieved using polaritons supported in noble metals [106], nanoscale confinement in the IR is more challenging due to the much longer free-space wavelengths [52, 107]. In return, however, IR nanophotonics offers a multitude of potential technological advancements, including super-resolution imaging [108], enhanced IR spectroscopy [109], and free-space signaling and communications [110]. One promising approach towards realizing such technologies is through the use of surface phonon polaritons (SPhPs)—the surface-bound electromagnetic modes of a polar material, resulting from the coupling of light with optical phonons [101]. One significant benefit of SPhPs is that they exhibit substantially lower losses than their well-studied metal-based counterparts, surface plasmon polaritons (SPPs), due to the much longer scattering times of optic phonons compared to those of electrons in metals [111]. In this sense, low-loss SPhPs constitute an attractive alternative to SPPs whose intrinsic losses have so far limited their broad usage in many practical applications [101].

SPhPs, however, are only supported in the relatively narrow Reststrahlen bands of polar dielectrics, such that, once a particular material system is chosen, the spectral characteristics of the SPhPs it supports are fixed. Fig. 6.1 shows an exemplary SPhP dispersion in the Reststrahlen band of a generic polar semiconductor. Although a large number of polar materials exist in nature which *combined* cover almost the entire MIR to terahertz spectral range [112], any one given material only supports SPhPs in its own specific narrow band.

In this chapter, an approach towards modifying and broadening the spectral range for SPhPs is demonstrated both, experimentally and theoretically, by employing atomic-scale superlattices (SLs) composed of commercially available
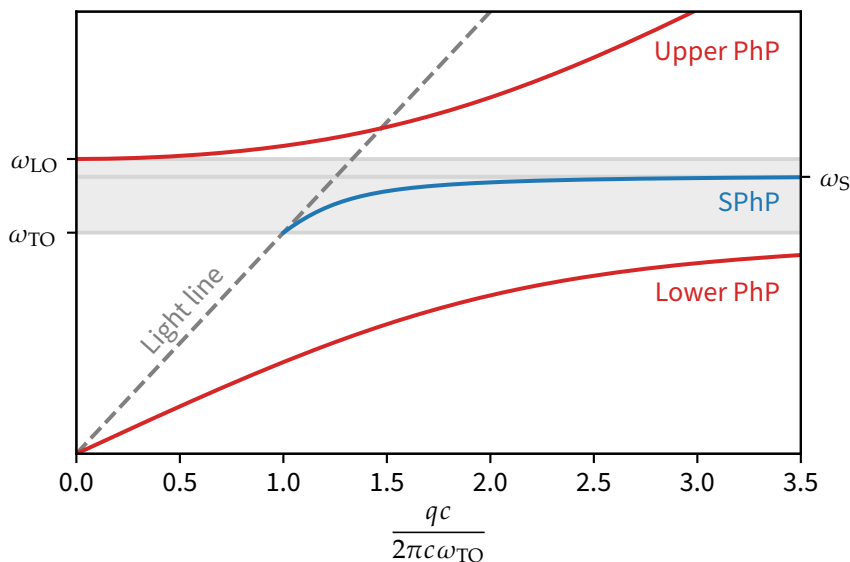
Figure 6.1.   **Dispersion relation of bulk and surface phonon polaritons.** While bulk phonon polaritons develop upper and lower polariton branches outside of the highly reflective Reststrahlen band, SPhPs are exclusively limited to frequencies between the TO phonon frequency and the cutoff frequency, ω_S, *within* the Reststrahlen band.

III-V semiconductors.[1] Combining two materials to form a SL strongly affects the chemical bonding, electrostatic, and lattice constants at and around the interfaces, leading to modified vibrational modes [114, 115]. Moreover, confinement effects can occur, giving rise to phonon modes which oscillate predominantly in one material [114], or new vibrational states which span both materials. Also, interface phonon modes may be supported whose vibration is localized to the interfaces between the individual layers [116].

As the SL layer thicknesses approach the length scale of only a few atomic monolayers, chemical bonding at the numerous interfaces plays an increasingly prominent role in the formation of phonon modes in the SL. These, in turn, directly impact the dielectric response of the SL. In the following, such atomic-scale SL structures will be referred to as crystalline hybrids (XHS) as their dielectric response deviates significantly from those of its constituent materials [117, 118].

A detailed description of the specific XH structures studied here will be given in Sec. 6.1. Sec. 6.2 then deals with the characterization of the unique vibrational modes emerging in such SLs using second-harmonic phonon spectroscopy and demonstrates their strong dependence on the atomic-scale layer thicknesses. These *hybrid* modes give rise to a distinct dielectric response which is investigated experimentally and theoretically in Sec. 6.3. Most notably, the XH structures stud-

---

1 The III-V's refer to a class of semiconducting compounds of group III (mostly Al, Ga, In) and group V elements (mostly N, P, As, Sb). They are commonly used in light-emitting diodes (LEDs), diode lasers, photodetectors, and solar cells [113].

ied here feature pronounced hyperbolic bands which are discussed in Sec. 6.4 with regard to the hyperbolic polariton modes they support. Finally, a conclusion is given in Sec. 6.5.

6.1. Crystalline Hybrids

The concept of xHs is demonstrated by employing multiple atomic-scale AlN/GaN SL structures, grown along their optic c-axis using molecular beam epitaxy (MBE), on semi-insulating SiC substrates.[2] Both, AlN and GaN, have the hexagonal wurtzite crystal structure and are anisotropic with A_1-type and E_1-type phonon modes, oscillating parallel and perpendicular to the crystal's c-axis, respectively. Their bulk phonon frequencies are summarized in Tab. 6.1, along with those of the SiC substrate. As bulk compounds the three materials have similar IR responses with overlapping Reststrahlen bands. These are shown in Fig. 6.2b as calculations based on the values in Tab. 6.1.

Table 6.1. A_1 (extraordinary) and E_1 (ordinary) phonon frequencies and high-frequency permittivities of bulk AlN, GaN, and the SiC substrate. Values are taken from Refs. 119–121.

Material	Out-of-plane			In-plane		
	ω_{TO}	ω_{LO}	$\varepsilon_{\infty,\parallel}$	ω_{TO}	ω_{LO}	$\varepsilon_{\infty,\perp}$
	[cm^{-1}]			[cm^{-1}]		
AlN [119]	614	893	4.0	673	916	4.3
GaN [120]	533	735	5.3	561	743	5.3
SiC [121]	783	964	6.7	798	966	6.5

Two representative xH structures were grown for the experiments presented in this chapter which in the following will be referred to as samples A and B:

Sample A This xH structure consists of 50 alternating AlN and GaN layers with a ~50 nm thick AlN buffer layer between the xH and the SiC substrate. Notably, this sample was deliberately not rotated during the MBE growth process, such that a gradient in the Al- and Ga-flux caused a significant variation in the corresponding layer thicknesses across the SiC wafer surface. As a result, AlN and GaN layer thickness values range from ~2 to 3 nm, depending on the position on the sample. A cross-sectional scanning transmission electron microscope (STEM) image of sample A is shown in Fig. 6.2c. At the particular position shown in the STEM image, each layer is ~2 nm thick.

---

2 Sample growth and preparation has been performed by D. Scott Katzer at the US Naval Research Laboratory in Washington, D.C. (USA).
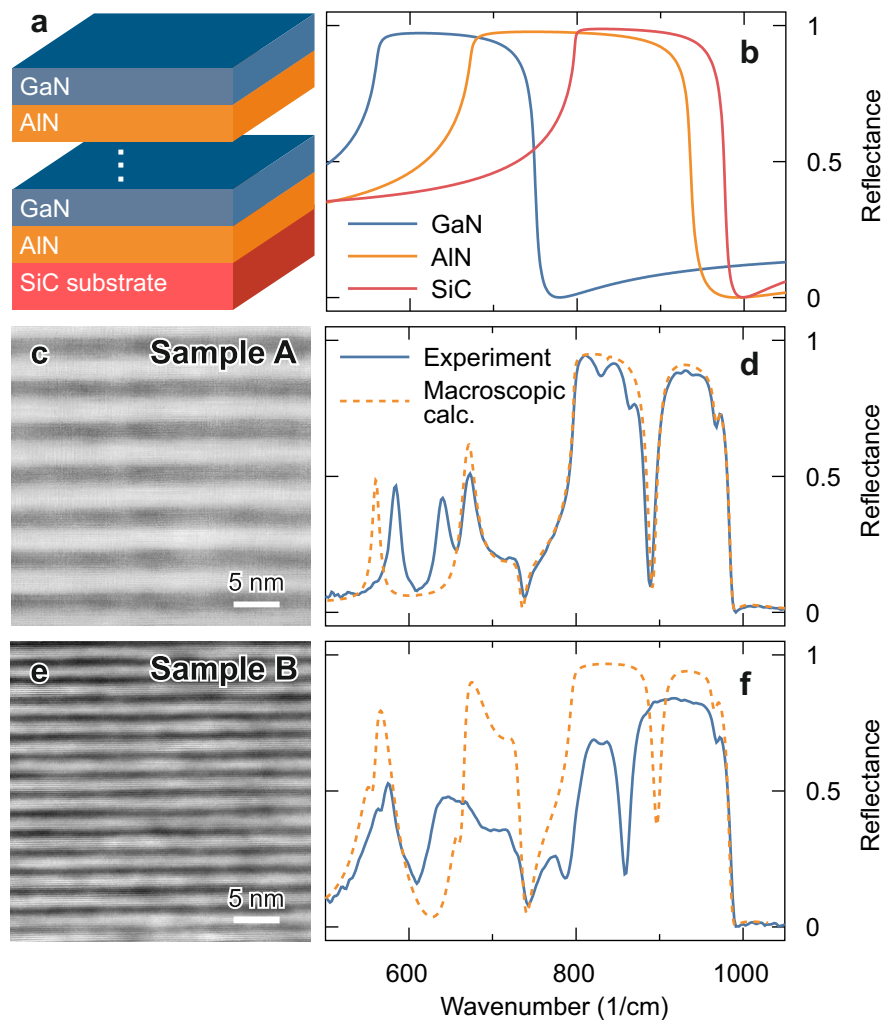
Figure 6.2. **STEM images and IR reflectance spectra of AlN/GaN atomic-scale super-lattices. a:** Illustration of the AlN/GaN superlattices on a SiC substrate. **b:** Calculated IR reflectance spectra of bulk AlN, GaN, and SiC at normal incidence. **c** and **e:** Cross-sectional high-angle annular dark-field STEM images of samples A and B, respectively. Here, AlN and GaN layers appear as dark- and light-gray bands, respectively. **d** and **f:** Experimental IR reflectance spectra (blue) incident at 65° and macroscopic calculations (dashed orange) based on the bulk properties of AlN and GaN. Reproduced from Ref. 105.

Sample B The second xʜ structure consists of 500 atomically thin, alternating layers of AlN and GaN with thicknesses of ~1.2 nm and 1.4 nm, corresponding to about 4 and 5 atomic monolayers, respectively. As this sample was rotated during growth, the layer thickness distribution across the sample surface can be assumed to be uniform. Both, sᴛᴇᴍ (Fig. 6.2e) and x-ray diffraction (xʀᴅ) measurements imply chemical intermixing at the interfaces, but a generally high degree of chemical segregation.

The optic phonon modes in sʟ structures composed of polar materials [122]—and, more specifically, ɪɪɪ-nitride materials [123–128]—have been extensively studied and described by both, microscopic and macroscopic models [116]. For layer thicknesses well above atomic length scales, the sʟ ɪʀ response is generally assumed to be adequately described by macroscopic electromagnetic models as, for example, the transfer-matrix method, based on the layers' bulk dielectric functions [91]. If, in addition, the sʟ layer thicknesses are much smaller than the wavelength of the applied light, a particular simple macroscopic description applies, known as the effective medium approximation.

If, however, the layer thicknesses of the sʟ are reduced to only a few atomic monolayers, macroscopic models no longer describe the sʟ's phonon modes accurately as the atomic-scale interactions in such xʜs modify the phonon modes in a fundamental way. For instance, the now prominent effects of the interfacial bonds impose different boundary conditions and the lattice constants of the epitaxially grown layers deviate significantly from their bulk values.

This point is illustrated by the experimental ɪʀ reflectance curves of both samples, ᴀ and ʙ, shown in Figs. 6.2d and f, respectively, along with the calculated reflectance of the sʟs using the macroscopic transfer-matrix approach based on the bulk dielectric properties of AlN and GaN. The comparison clearly exposes the macroscopic model's inability to describe the xʜ's ɪʀ response accurately. The discrepancy is even more pronounced for sample ʙ which features thinner and a higher number of layers and hence more prominent interface and confinement effects.

These results constitute an initial demonstration of the xʜ concept, highlighting the qualitatively different ɪʀ response of *atomic-scale* sʟ structures as opposed to sʟs with *mesoscopic* layer thicknesses which are well-described by conventional approaches, such as the transfer-matrix formalism or the effective medium theory. In order to gain a more quantitative picture of the xʜ's ɪʀ response, the following section discusses the structure's optic phonon modes which determine the poles and zeros of its ɪʀ dielectric function as well as the spectral extent of its Reststrahlen bands.

6.2. Optic Phonon Modes and Tunability

A quantitative determination of the optic phonon modes in the XH using linear IR techniques, e.g., Fourier-transform infrared (FTIR) spectroscopy, is challenging due to the highly reflective nature of the SiC subtrate's Reststrahlen band as well as the multiple Reststrahlen bands of the XH itself. Here, second-harmonic phonon spectroscopy constitutes a suitable tool as it allows to aptly determine and identify phonon modes in multimode systems on a nominally flat background as demonstrated in Ch. 5 for α-quartz. While for α-quartz, the IR SHG spectra showed primarily peaks at TO phonon frequencies with large contrast [71], in the XH system also LO modes produce pronounced SHG peaks. This is due to so-called Berreman modes emerging in thin dielectric films close to zero-crossings of the dielectric function (epsilon-near-zero condition), e.g., at LO phonon frequencies [129–131]. These modes exhibit extreme subwavelength confinement and strong field enhancements, causing pronounced peaks in the SHG spectra [132].

The IR SHG and reflectance spectra taken at three representative locations on sample A with varying AlN and GaN layer thicknesses are shown in Fig. 6.3. The SHG spectra show, in addition to phonon resonances of the XH itself, also peaks corresponding to the SiC substrate as well as the AlN buffer layer (blue and orange shades in Fig. 6.3, respectively). These resonances, however, are easily identified as they occur at the bulk phonon frequencies of SiC and AlN and are invariant against the changing layer thicknesses at different positions on the sample. In contrast, phonon peaks originating from the XH structure vary strongly in their spectral position. Specifically, the XH is observed to support two E_1-type TO phonon modes around ~575 cm^{-1} and ~630 cm^{-1} as well as three A_1-type LO modes, one around ~735 cm^{-1} and two between 840 cm^{-1} and 880 cm^{-1} (green shade in Fig. 6.3). Remarkably, these modes show significant frequency shifts of more than 10 cm^{-1} even for these small layer thickness variations on the Ångström-scale.

One possible reason for the strong layer thickness dependence of the phonon frequencies in the XH is the development of significant strain across the sample. In fact, it has been reported in the literature that lattice strain may cause phonon frequency shifts in AlN/GaN SLS [123, 133]. For the XH structure at hand, a quantitative determination of the in-plane-strain using XRD reciprocal space mapping[3] showed that the observed phonon frequency shifts are mostly consistent with the measured in-plane-strain [105]. This would provide a direct means to tune phonon frequencies in the XH via lattice strain, depending on the AlN/GaN layer thickness ratio. Apart from lattice strain, however, layer thicknesses can also potentially influence phonon frequencies through modified interface bonding and

---

[3] The XRD characterization and reciprocal space mapping were performed by Neeraj Nepal and Matthew T. Hardy at the US Naval Research Laboratory in Washington, D.C. (USA).
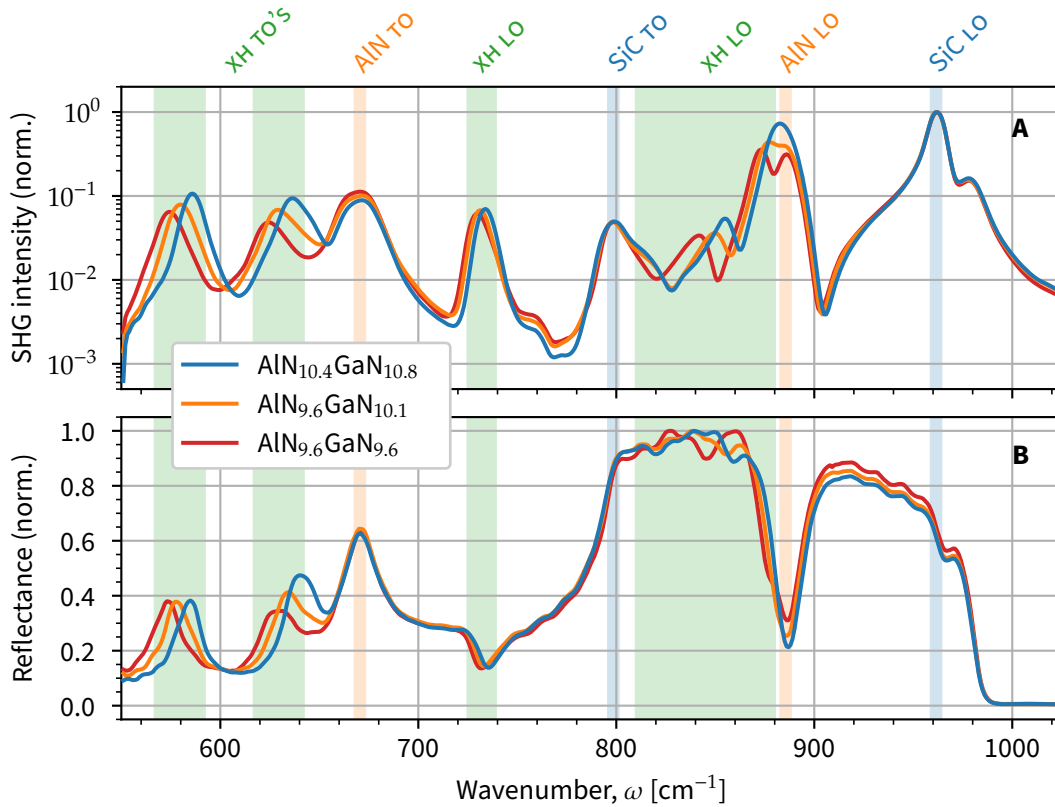
Figure 6.3.   Modification of optic phonon modes in XHS. A: Experimental SHG spectra at three representative positions on sample A. SHG peaks mark optic phonon resonances in the SL structure. While resonances associated with bulk SiC (blue shade) and AlN (orange shade)—originating in the substrate and the buffer layer, respectively—do not shift spectrally with varying layer thicknesses, the XH modes (green shade) show significant frequency shifts, demonstrating the tunability of the XH's IR response. **B:** Corresponding reflectance spectra show the formation of multiple Reststrahlen bands, consistent with the SHG features. Subscripts in the legend denote the average number of atomic monolayers. Please note the logarithmic scale in **A**.

abruptness, and phonon confinement. The impact of these additional parameters is still to be determined in future research.

Nevertheless, a description of the modified dielectric function solely based on strain-induced phonon frequency shifts is incomplete as it does not explain the *additional* phonon modes observed in both xh samples. In order to further investigate the effects of modified chemical bonding at the interfaces, we now turn to sample b where the layer thicknesses are reduced to just a few atomic monolayers. Here, interface and confinement effects are expected to become even more prominent.

6.3. Infrared Dielectric Response

The induced and modified phonon modes in the xh structures directly impact its ir dielectric response. To account for the interfacial and confinement effects which play a more significant role in few-monolayer xh structures, sample b is treated as a whole and its dielectric response determined for the entire xh film. To this end, the in- and out-of-plane dielectric functions are extracted from ir ellipsometric reflectance spectra.[4] Notably, spectroscopic ellipsometry of the basal-plane-oriented uniaxial xh is insensitive to its A_1-type to phonon mode which, instead, was determined using Raman spectroscopy and fixed at the resulting 552 cm^{-1} in the ellipsometric least-squares fit. The real and imaginary parts of both, $\varepsilon_\perp(\omega)$ and $\varepsilon_\parallel(\omega)$, are shown in Figs. 6.4a and b, respectively. The extracted dielectric response shows that the xh is strongly anisotropic and exhibits multiple Reststrahlen bands along both principal directions as a result of the xh-induced and shifted optic phonon modes.

In order to gain qualitative insight into the vibrational character of the xh's phonon modes, the experimental data are compared to density functional pertubation theory (dfpt) calculations—an ab initio method to incorporate atomistic details, e.g., the effect of interface bonds. In these calculations,[5] the layer thicknesses are set to span 4 atomic monolayers of AlN and 5 monolayers of GaN in each period as this largely conforms to the layer thicknesses determined by stem in sample b (see Fig. 6.2e). Also, the lattice constants are assumed to be fully relaxed. As a result, the dfpt calculations yield a set of phonon frequencies and vibrational patterns, a full list of which can be found in Appx. B. On the basis of these dfpt-derived phonon frequencies, it is now possible to calculate the theoretical ir dielectric response of sample b using the fpsq model described

---

4 The ir ellipsometry measurements and fitting procedures were carried out by Joshua D. Caldwell, Ioannis Chatzakis, Alexander J. Giles, and Daniel C. Ratchford at the us Naval Research Laboratory, Washington, d.c. (usa).

5 dfpt calculations were performed by Pratibha Dev [Howard University, Washington, d.c. (usa)] and Thomas L. Reinecke [us Naval Research Laboratory, Washington, d.c. (usa)].
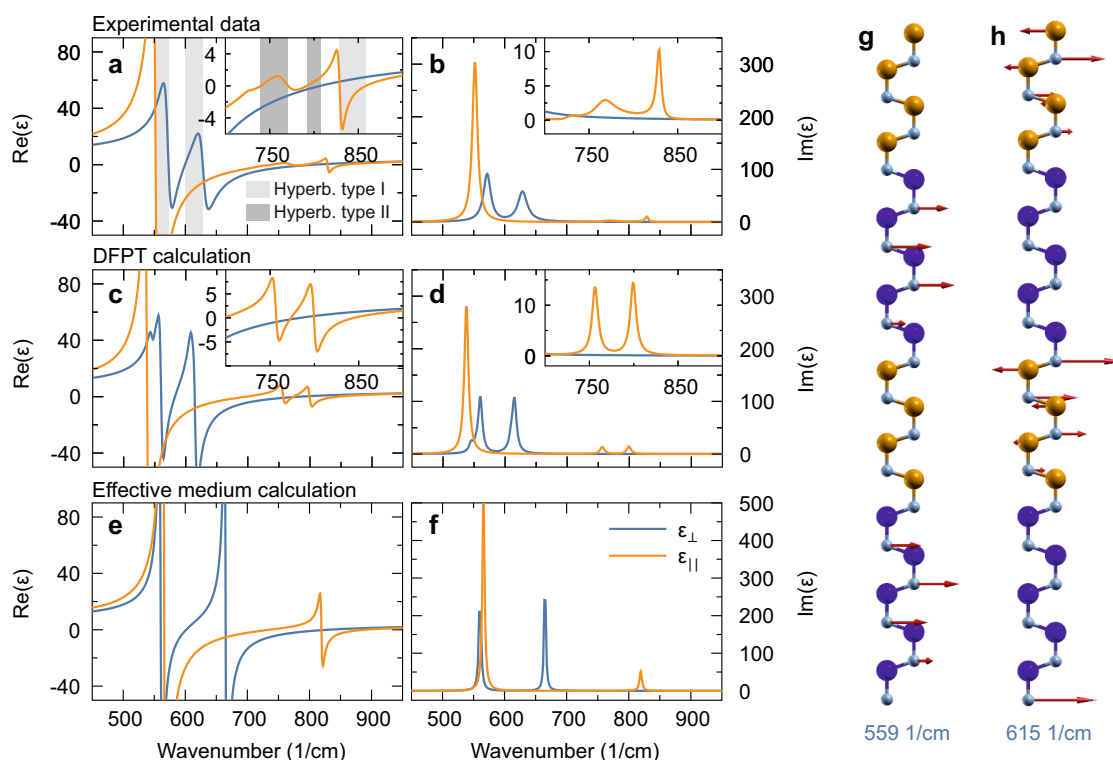
Figure 6.4. **Dielectric function of the XH. a, b:** Real and imaginary parts of the experimentally determined permittivity of sample B using IR ellipsometry. Shaded areas indicate hyperbolic bands of type I (light gray) and type II (dark gray). **c,d:** Theoretical permittivity using DFPT. **e,f:** Theoretical permittivity using an effective medium approach. **g,h:** Phonon vibrational patterns associated with the lower and upper in-plane Reststrahlen bands, respectively. Here, blue, orange, and gray spheres represent Ga, Al, and N atoms, respectively, and red arrows indicate atomic displacement. Reproduced from Ref. 105.

in Sec. 3.2.1 (Eq. 3.2.12). Here, damping rates, γ, of all phonon modes were empirically chosen to be $10\,\text{cm}^{-1}$. The resulting DFPT-based dielectric functions are shown in Figs. 6.4c and d.

In addition, effective medium calculations of the XH's dielectric response are employed. This approach is based on the average of the GaN and AlN bulk dielectric functions, weighted by their relative layer thicknesses in the SL structure. Comparing the effective medium calculations, shown in Figs. 6.4e and f, with the experimental data shows that the macroscopic approach fails to predict several important features of the XH's IR response as atomic-scale interactions remain unaccounted for in this theoretical framework. In contrast, good qualitative agreement with the experimental data is found with the DFPT-derived dielectric function.

Upon closer inspection of the experimental IR response, two distinct Reststrahlen bands are found in the in-plane dielectric function, $\varepsilon_\perp(\omega)$: one narrow region from $572\,\text{cm}^{-1}$ to $599\,\text{cm}^{-1}$ and another from $629\,\text{cm}^{-1}$ to $807\,\text{cm}^{-1}$. Similar Reststrahlen bands are found in the DFPT-derived dielectric function, but with a redshift of $\sim15\,\text{cm}^{-1}$ with respect to the experimental data. This is typical for DFPT calculations and can be attributed to the choice of the exchange-correlation functional [105]. The calculated vibrational pattern associated with the lower Reststrahlen band, illustrated in Fig. 6.4g, closely resembles a GaN-confined mode. The vibrational pattern associated with the upper in-plane Reststrahlen region (Fig. 6.4h), on the other hand, is predominantly confined to the AlN layers, but oscillates most strongly at the AlN/GaN interfaces.

The experimental out-of-plane dielectric function, $\varepsilon_\parallel(\omega)$, is dominated by a broad Reststrahlen band extending from $536\,\text{cm}^{-1}$ to $740\,\text{cm}^{-1}$. The corresponding vibrational pattern from DFPT shows that the phonon mode involves the displacement of nitrogen atoms in both layers. Although the nitrogen atoms' displacement is larger in the GaN layers, the phonon mode exhibits an extended character overall. Two additional minor Reststrahlen bands are observed within $\varepsilon_\parallel(\omega)$: one extending from $769\,\text{cm}^{-1}$ to $791\,\text{cm}^{-1}$ and the other from $828\,\text{cm}^{-1}$ to $859\,\text{cm}^{-1}$. Here, the DFPT-derived vibrational patterns indicate that their associated modes involve atomic movement in both layers, but larger oscillation amplitudes in the AlN layers due to their lighter reduced mass (see Appx. B).

Comparing the in- and out-of-plane IR dielectric functions, it becomes clear that the XH behaves strongly anisotropic and gives rise to both, elliptical and hyperbolic bands [134] due to its multiple Reststrahlen regions. Unlike most hyperbolic systems, however, the XH exhibits a wide spectral range, over which both, positively and negatively valued permittivities are highly dispersive. This also causes extreme birefringence in excess of unity over a large portion of the spectrum. For instance, the birefringence, defined as $\Delta n = n_\parallel - n_\perp$, reaches

a maximum of ~10 at 527 cm^{-1}, but drops rapidly to ~-8 at 566 cm^{-1}. This offers a useful opportunity to engineer hyperbolic spectral bands through careful selection of materials, layer thicknesses, and epitaxial mismatch.

One common concern, when employing SL designs to modify the IR dielectric response, especially at the atomic scale, is the introduction of optical losses as these determine their polariton performance and, ultimately, their applicability. In order to quantify the optical losses, we here consider the damping parameter, γ, of the various XH modes in comparison to those of the bulk constituents, AlN and GaN. While fits to the XH dielectric function yield values in the 10 cm^{-1} to 25 cm^{-1} range, ellipsometry measurements of bulk AlN and GaN films revealed damping rates of ~15 cm^{-1} for AlN and ~5 cm^{-1} for GaN. Therefore, the damping rates in the XH structure can be considered to be on the same order as those of its constituent materials, allowing a modification of its IR response without introducing a dramatic increase in optical losses. For a more direct validation of the modified nanophotonic performance of the atomic-scale SL structure, however, the following section presents a closer investigation of the XH polariton modes themselves.

6.4. Polariton Performance

A more definite test of validity to the extracted dielectric response discussed in the previous section is the ability to make accurate predictions of the XH polariton modes. To this end, transfer-matrix calculations [91], based on the experimentally determined IR dielectric function, have been employed. Specifically, the imaginary part of the reflection coefficient, r_p, has been evaluated which peaks at polariton resonances [103] and thus allows to track their dispersion relations. The results are shown as false color maps in Figs. 6.5a and b. For the small wave vector values, shown in Fig. 6.5a, multiple branches of strongly dispersing surface polaritons are observed.

In order to validate the transfer-matrix calculations, Otto geometry prism-coupling experiments have been performed, providing experimental access to the polariton dispersion for small wave vector values, i.e., close to the light line (cf. Fig. 6.1).[6] Details on the experimental technique can be found in Ref. 135. In short, a high-refractive index prism—here, KRS-5 ($n \approx 2.4$)—in total internal reflection provides the in-plane momenta necessary to couple to SPhPs. Scanning the wavelength of the FHI FEL through the XH's Reststrahlen region while detecting the reflected FEL intensity results in reflectance spectra with distinct dips within Reststrahlen bands at SPhP frequencies. Varying the FEL beam's incidence angle,

---

6 Transfer-matrix calculations and Otto-type prism-coupling experiments have been performed by Nikolai C. Paßler.
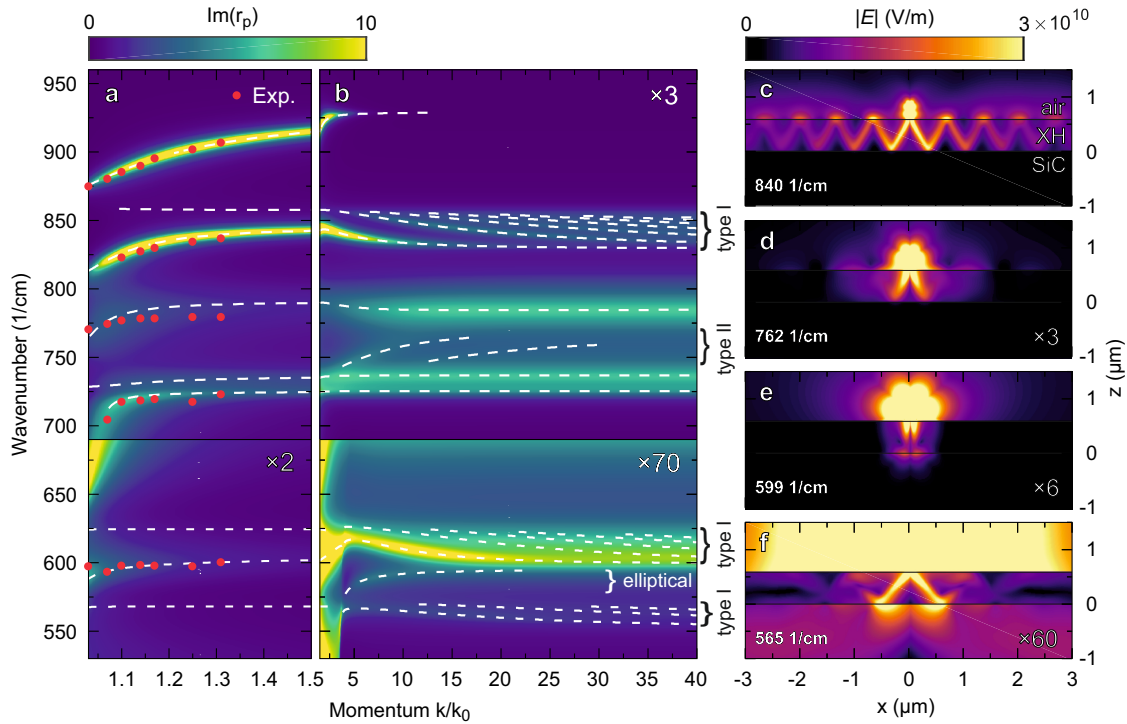
Figure 6.5. **Theoretical polariton dispersion of the xʜ. a, b:** Imaginary part of the Fresnel reflection coefficient for *p*-polarized light, $Im(r_p)$, as a function of the relative in-plane momentum, k/k_0. Dashed lines represent extracted mode dispersions from calculations with reduced damping rates. Red dots in **a** mark SPhP positions from prism-coupling experiments. Volume-confined hyperbolic mode progression is observed in **b** in all four hyperbolic bands as well as one elliptical mode as indicated. **c–f:** Spatial electric field profiles for localized excitation of type ɪ (**c, e, f**) and type ɪɪ (**d**) hyperbolic polariton modes. Reproduced from Ref. 105.

θ_{ext}, and consequently the in-plane momentum, $k = \omega/cn \sin\theta_{ext}$, allows to excite SPhPs along their dispersion. The extracted positions of the reflectance dips in the Otto geometry, marked as red dots in Fig. 6.5a, are in very good agreement with the transfer-matrix-based predictions. This corroborates the validity of the transfer-matrix calculation as well as the experimentally determined ɪʀ dielectric response it is based on.

At larger wave vectors, shown in Fig. 6.5b, strongly confined hyperbolic and elliptical polariton modes emerge in the xʜ film as expected from the hyperbolic and elliptical regions in the xʜ's ɪʀ dielectric response (Fig. 6.4a), respectively. Specifically, three type ɪ hyperbolic bands ($555\,cm^{-1}$ to $571\,cm^{-1}$, $599\,cm^{-1}$ to $625\,cm^{-1}$, and $830\,cm^{-1}$ to $860\,cm^{-1}$) are observed, showing a pronounced mode progression—typical for hyperbolic polariton modes in thin films [103]. Additionally, one type ɪɪ hyperbolic band is found between $740\,cm^{-1}$ and $770\,cm^{-1}$ as well as one elliptical band from $572\,cm^{-1}$ to $599\,cm^{-1}$. Due to the rapid dispersion of the xʜ's highly anisotropic dielectric tensor, the associated polariton modes not

only vary strongly among these different bands, but also *within* each band. This is in stark contrast to most other hyperbolic systems where the positive dielectric component is typically constant [53, 93, 103, 136]. To illustrate this behavior, the optical field profiles of the various polariton branches have been simulated.[7] Four representative examples are shown in Figs. 6.5c–f. Here, it is apparent that the strong dispersion of both dielectric components results in hyperbolic modes whose propagation angle [137–139] and length vary drastically within only small spectral intervals.

Notably, this gives rise to two independent tuning mechanisms of the polaritonic dispersion in xh systems: (i) modification of the optic phonons through the individual atomic-scale layer thicknesses which can alter the positions, widths, and number of the xh polaritonic bands. (ii) The total sl stack thickness, i.e., the number of sl layers which changes the dispersion of the modes within each polaritonic band. Through these mechanisms, the xh concept provides a flexible platform for nanophotonic applications. An additional benefit of the xh approach is that a heterostructure of two materials for a deliberately modified ir response also allows to potentially maintain and combine the mechanical, electrical, or optoelectronic properties of the individual constituents.

6.5. Conclusion

In this chapter, atomic-scale heterostructures composed of well-established semiconductors have been introduced as a promising route towards engineered ir nanophotonic materials, using a AlN/GaN sls as a model system. As the sl layer thicknesses approach the order of a few atomic monolayers, new optic phonon modes emerge in the metamaterial, leading to a distinct ir dielectric response which differs *qualitatively* from those of its bulk constituents. Thus, the resulting hybrid does not behave as an effective medium of two bulk materials, but rather as a new material—featuring its own phonon modes and dielectric properties.

Importantly, the metamaterial approach allows to deliberately modify the ir response by varying the individual atomic-scale layer thicknesses as well as the total xh film thickness. Specifically, it has been demonstrated using shg phonon spectroscopy that marginal changes to the AlN and GaN layer thicknesses lead to significant frequency shifts of the sample's hybrid phonon modes. This provides a control mechanism to manipulate the xh's optical constants, broaden Reststrahlen bands, and, ultimately, tune polariton modes without substantially increasing optical losses. The particular xh system studied here has a unique, strongly anisotropic ir dielectric response, featuring multiple Reststrahlen bands

---

7 Optical field profiles were calculated by Joseph R. Matson and Matthew T. Hardy at the Vanderbilt University in Nashville, Tennessee (usa), using cst Studio Suite and its frequency domain solver.

which give rise to pronounced elliptical and hyperbolic spectral regions. These are highly dispersive and show extreme birefringence with Δn in excess of unity over a wide spectral range, reaching peak values above 10. This may offer opportunities in various application spaces, including on-chip optical elements [140] and polarization control for waveguides [141].

Transfer-matrix calculations of the xʜ's polaritonic response based on its dielectric function predict numerous SPhP branches which are in excellent agreement with experimental probes. Further, for larger wave vectors, the calculations predict multiple volume-confined type ɪ and ɪɪ hyperbolic polariton modes, enabling hyperlens designs for super-resolution imaging and nanolithography [96, 142] with enhanced spectral flexibility thanks to the xʜ approach.

In the following chapter, we will consider another technologically relevant class of functional materials and how second-harmonic phonon spectrocopy can be employed for the characterization of its vibrational and symmetry properties.

Chapter 7.

Nonlinear Infrared Spectroscopy for Phase Transition Studies in Multiferroics

Today's technological landscape presents numerous examples of ferroic materials being used in sensors, actuators, and data storage devices. For instance, large amounts of digital data is stored in ferromagnets while ferroelectrics and ferroelastics are widely used in mechanical and acoustic sensors. In this context, it is not surprising that multiferroics—materials exhibiting multiple ferroic properties in a single phase—offer technological opportunities for multifunctional and miniaturized devices and are of immense research interest.

These multiferroic states of matter are accompanied by structural phase transitions which lead to the joint occurrence of two or more ferroic orderings at a certain temperature and pressure. Many multiferroic materials subjected to current research feature phase transitions which are not yet fully understood due to the lack of suitable characterization techniques. Here, second-harmonic phonon spectroscopy which has been shown to be sensitive to structural phase transitions in Ch. 5, could provide new physical insight into currently studied multiferroic materials. While visible SHG has been successfully applied to probe multiferroic phases and domains [73, 143], no IR SHG studies of multiferroic materials are present in the literature. Its intrinsic sensitivity to symmetry as well as atomic structure through optical phonon resonances—carrying symmetry information themselves—however, could prove to be a valuable tool in the determination of symmetry properties and structural changes at and around multiferroic phase transitions. Moreover, most multiferroic phases emerge at cryogenic temperatures—a measurement regime in which IR SHG is particularly sensitive due to generally decreased phonon damping rates (see Sec. 5.4).

The goal of the work presented in this chapter is to explore the feasibility of IR SHG as a spectroscopic tool for the study of phase transitions in multiferroic materials. The following section gives a brief overview of the multiferroic material class. Sec. 7.2 introduces the specific material system studied here, i.e., $HoMnO_3$ as a member of the orthorhombic manganites. Finally, Sec. 7.3 describes the

experimental setup and presents the results which are then critically discussed in Sec. 7.4.

7.1. A Brief Introduction to Multiferroics

The spontaneous alignment of magnetic moments in a solid is commonly referred to as ferromagnetism (from Latin *ferrum:* iron) and is a well-known phenomenon in physics. Similarly, the spontaneous ordering of electric dipole moments is named ferroelectricity [144]—in close analogy to ferromagnetism as both effects behave much alike, for instance with regard to their hysteretic switching between two stable states under the influence of a conjugate electric or magnetic field, respectively [145]. Typical hysteresis curves of a ferromagnet and a ferroelectric are shown in Fig. 7.1. Ferroism in general describes any spontaneous, switchable internal alignment. Apart from ferromagnetism and -electricity, examples of primary ferroic orderings also include ferroelasticity—describing strain states which are switchable via an external stress field—as well as ferrotoroidicity, i.e., toroidal moments which can be switched by crossed electric and magnetic fields [146]. Today, electric polarization in ferroelectrics and magnetization in ferromagnets are widely used in data storage applications where opposite orientations represent binary data bits, "0" and "1" [147].
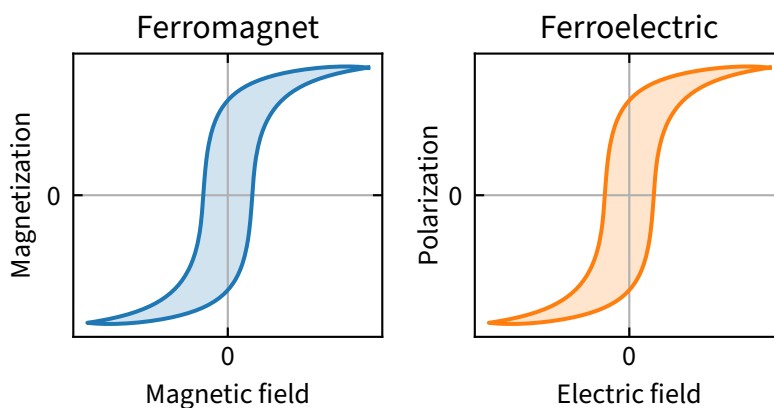
Figure 7.1. Ideal hysteresis curves of a ferromagnet and a ferroelectric. Ferroic materials exhibit a spontaneous internal alignment which can be switched by an external field. The most common ferroics are ferromagnets **(left)** and ferroelectrics **(right)** whose internal magnetization and polarization can be hysteretically switched by external magnetic and electric fields, respectively, as shown here.

Multiferroics are materials which combine two or more ferroic orders. When introduced in 1994 [148], the term multiferroic described materials which combine multiple ferroic orders in the same phase. Today, however, multiferroism

mostly refers to the coexistence of ferroelectricity and ferro-, ferri-, or antiferro-magnetic order in either single- or multiphase materials [145]. If the ferroelectric and magnetic phases emerge independently, the multiferroic is denoted as type I, whereas type II multiferroics indicate the joint occurrence of both ferroic orders. From a technological viewpoint, multiferroics are highly intriguing. For instance, combining a magnetic with an electric bit would allow the design of four-state memory elements [149]. Alternatively, and perhaps more interestingly, a coupling of ferroelectric to magnetic states—so-called magnetoelectric coupling—could lead to novel functionalities. For instance, electric-field control of the ferromagnetic state could lead to smaller, more energy-efficient devices by avoiding electric currents—associated with waste heat and relatively long build-up times—in favor of voltage pulses.

Unfortunately, multiferroics are inherently rare. Phenomenologically, this is not surprising as, in order to sustain an electric polarization, a ferroelectric has to be insulating while magnetic materials, on the other hand, are most often conducting metals [146]. In a conventional ferroelectric material, cations experience a displacement away from the center of their surrounding anions, breaking centrosymmetry and causing the dipole moment. This type of ferroelectricity is energetically favorable if the cation has an empty d^0 shell [150]. By contrast, magnetic materials require unpaired electrons in a partially filled d shell and thereby obstruct such displacive ferroelectricity.

One way to lift this seeming contradiction is provided by complex oxides which constitute the most-actively studied class of multiferroics today. These compounds are comprised of two or more transition-metal ions as well as oxygen. The intermediate ionic–covalent nature of the transition-metal–oxygen bonds cause a strong polarizability while the transition-metal's localized d electrons facilitate magnetic order [146]. Among the complex oxides, a material system that has received particular attention, are the rare-earth manganites. The following section gives a brief overview of this material class and presents details on the manganite samples studied here.

7.2. Orthorhombic Holmium Manganite and Simulations

The rare-earth manganites are compounds with a chemical formula of $R\text{MnO}_3$, where R represents a rare-earth element. They crystallize in either a hexagonal (space group $P6_3cm$) or an orthorhombically distorted perovskite structure (space group $Pnma$), depending on the size of the rare-earth ionic radii. Generally, for radii smaller than that of Dy, i.e., $r_R < r_{\text{Dy}}$ with $R = \text{Y}, \text{Tm}, \text{Yb}, \text{Lu}, \text{Er}$, the manganites are hexagonal, whereas larger r_R lead to the formation of perovskite-like "orthomanganites" [151, 152] whose crystal structure is schematically shown

in Fig. 7.2. Notably, $DyMnO_3$ and $HoMnO_3$, with $r_R \simeq r_{Dy}$, can be synthesized in both crystal structures, depending on the growth conditions [151].
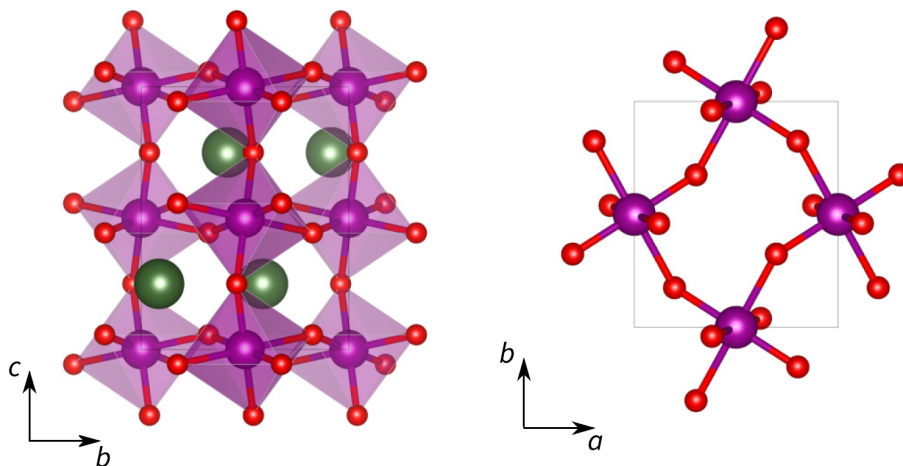

Figure 7.2. **Crystal structure of the orthorhombic manganites, o-$RMnO_3$.** Here, green spheres represent R^{3+} cations, purple spheres Mn^{3+} cations, and red spheres O^{2-} anions, respectively. Views are along the principal a **(left)** and c **(right)** axes. Reproduced from Ref. 153.

The multiferroic samples studied here are orthorhombic holmium manganite (o-$HoMnO_3$) films of varying thicknesses (17.8 nm, 25.0 nm, 52.5 nm, and 100.0 nm), grown on $YAlO_3$ substrates along the biaxial crystals' b axes ([010]).[1] The orthorhombic manganites are known to exhibit pronounced electromagnetic coupling [154–156] and, thus, are of particular research interest. Moreover, these materials exhibit two structural phase transitions, marking the onset of antiferromagnetic and ferroelectric order at $T_{AFM} \approx 39$ K and $T_{FE} \approx 25$ K, respectively [157].

Second-harmonic phonon spectroscopy has been shown to be sensitive to the structural α–β phase transition in the multimode oxide quartz (see Ch. 5). Similarly, the ferroelectric phase transition in rare-earth manganites is accompanied by a breaking of inversion symmetry to which second-harmonic phonon spectroscopy can be highly sensitive. For the interpretation of second-harmonic phonon spectra, however, good knowledge of the sample's linear IR properties has been shown to be most useful (see Ch. 5), but so far no report of the vibrational properties of o-$HoMnO_3$ has been published in the literature. Therefore, we instead turn to the isostructural, but well-studied orthorhombic manganite $TbMnO_3$ for simulations of the manganite's linear optical response, especially in view of the influence of the varying film thicknesses and the substrate's own dielectric response. To this end, calculations for four $TbMnO_3$ film thicknesses—in accordance to the o-$HoMnO_3$ samples—on a $YAlO_3$ substrate as well as the

---

1 The o-$HoMnO_3$ samples were grown by Christoph W. Scheider and Kenta Shimamoto at the Paul Scherrer Institute (PSI) in Zurich (Switzerland).

substrate itself have been performed using a transfer-matrix approach [91]. These calculations are based on experimental phonon data of TbMnO$_3$ [158] and DFPT calculations of the YAlO$_3$ substrate [159].
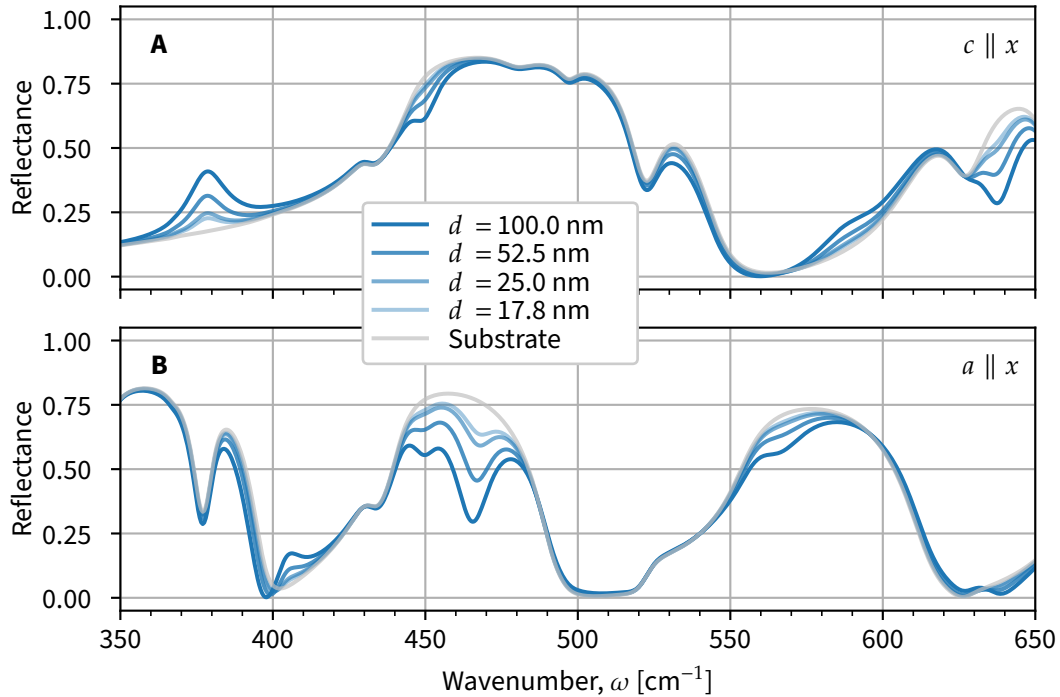
Figure 7.3. **Simulated reflectance spectra for TbMnO$_3$ films on a YAlO$_3$ substrate.** The spectra have been calculated for four different TbMnO$_3$ film thicknesses as well as the bare substrate with the principal c **(A)** and a **(B)** axes aligned horizontally using a transfer-matrix approach [91]. Based on TbMnO$_3$ phonon data from Ref. 158 and YAlO$_3$ DFPT calculations from Ref. 159.

The simulated reflectance spectra are shown in Fig. 7.3A and B for p-polarized light incident at 60° along the crystal's principal c and a axes, respectively. Notably, the reflectance spectra are dominated by the response of the YAlO$_3$ substrate, whereas the TbMnO$_3$ film causes rather subtle variations in form of dips within the YAlO$_3$ Reststrahlen bands or peak-like features in the tails. However, the data clearly show the effect of the TbMnO$_3$ film thickness on the reflectance as both, dips and peaks, become more pronounced as the manganite film thickness increases. This allows a clear distinction between spectral features caused by the TbMnO$_3$ film and the substrate. For the isostructural o-HoMnO$_3$, a comparable behavior is expected, although phonon frequencies are likely to be shifted.

7.3. Experiment

In order to confirm the trends observed in the simulated reflectance spectra, this section discusses the corresponding experiment on o-HoMnO$_3$ films as well as a field-cooled IR SHG experiment.

7.3.1. Thickness-Dependent Reflectance

In order to identify spectral positions of phonon resonances in o-HoMnO$_3$, a series of reflectance spectra has been obtained for varying manganite film thicknesses as well as the bare substrate. They are shown in Fig. 7.4A and B.

Again, as with the simulated spectra of TbMnO$_3$ on YAlO$_3$ shown in Fig. 7.3, the reflectance of o-HoMnO$_3$ is dominated by the substrate's response while the manganite itself causes peak-like features outside and dips within the Reststrahlen bands of YAlO$_3$. Upon inspection of the substrate's reflectance, however, significant discrepancies of the Reststrahlen band positions with respect to the simulated spectra in Fig. 7.3 are noticeable, making a direct comparison of the TbMnO$_3$ simulations with the experimental o-HoMnO$_3$ data difficult. This is likely due to shifted phonon frequencies in the DFPT calculations for the substrate [159] the simulations are based on, which is typical for DFPT calculations of this kind.

In order to resolve this issue and to ensure comparability, another set of transfer-matrix calculations is performed. This time, the FPSQ model (Eq. 3.2.12) is used to fit the experimental reflectance spectra of the bare substrate. For simplicity, an isotropic pseudo-crystal is assumed in each principal direction. Typically, the out-of-plane components of the dielectric tensor only add insignificant features to the reflectance [127]. Consequently, the reflectance is mainly determined by the in-plane dielectric component aligned parallel with the laser polarization. For this reason, a theoretical description of the experimental reflectance spectra with such a simplified model is warranted as the remaining dielectric components are negligible in their contribution to the detected signal. Tab. 7.1 lists the resulting phonon parameters which best describe the substrate's reflectance and the simulation results are plotted in Fig. 7.4C and D.

With the modified description of the substrate's dielectric response, the simulations of TbMnO$_3$ closely resemble the experimental spectra of o-HoMnO$_3$, with minor frequency shifts of the manganite film features, as expected. As with the simulations, modulations on top of the bare substrate's response are clearly identified as signatures of o-HoMnO$_3$'s phonon resonances and are marked accordingly in Fig. 7.4A and B as orange-shaded areas. Specifically, a spectrally narrow o-HoMnO$_3$ feature around $380\,\mathrm{cm^{-1}}$ along the c direction as well as broad features in both sample orientations between $\sim$$550\,\mathrm{cm^{-1}}$ and $\sim$$610\,\mathrm{cm^{-1}}$
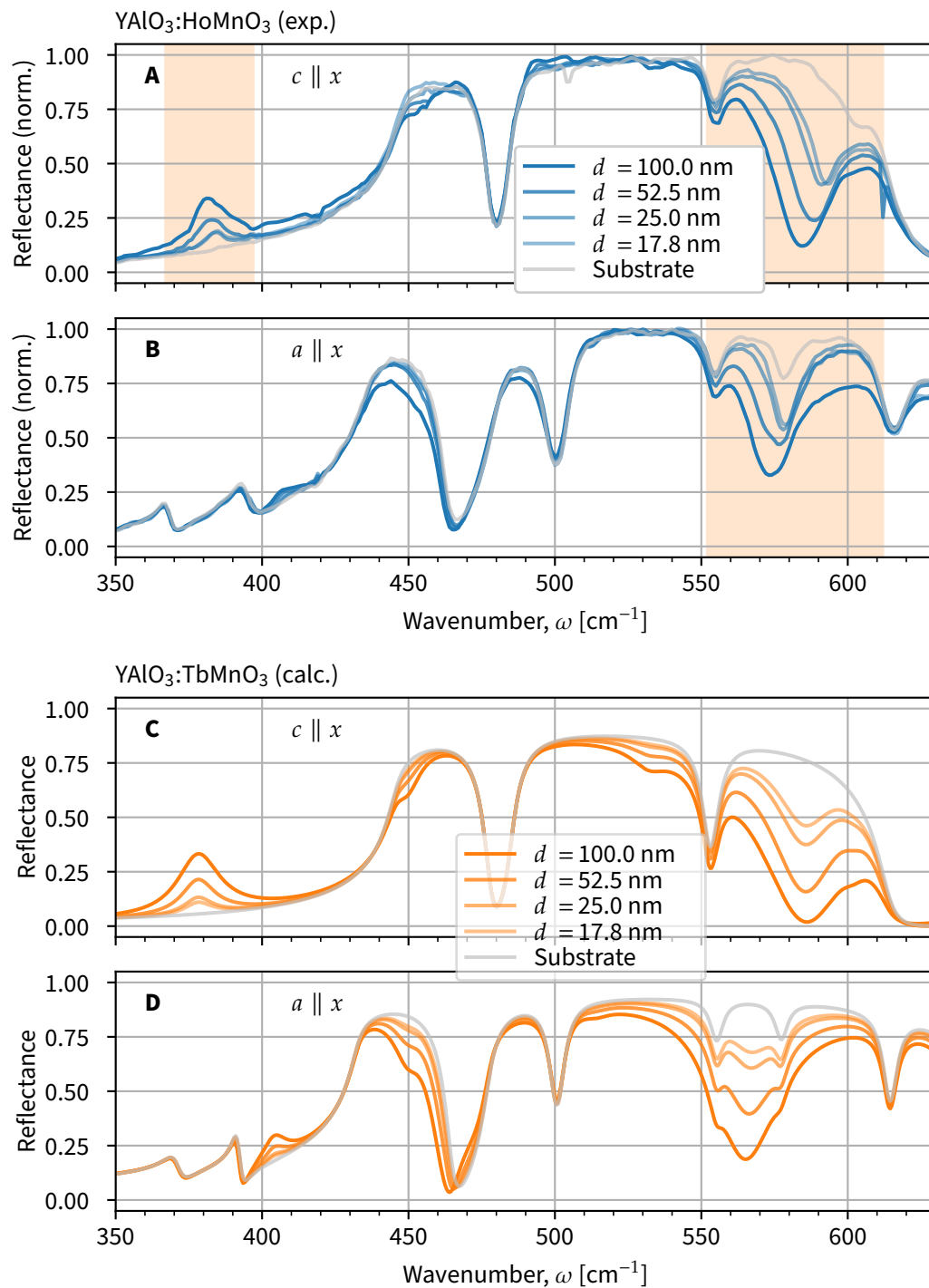
Figure 7.4. **Experimental and simulated reflectance spectra of o-HoMnO$_3$ and TbMnO$_3$ films on YAlO$_3$ substrates, respectively.** The experimental spectra have been obtained for four different o-HoMnO$_3$ film thicknesses as well as the bare substrate. The principal c **(A)** and a **(B)** axes are aligned horizontally at an incidence angle of 60° in p-polarization. Spectral features specific to the o-HoMnO$_3$-film are marked by orange-shaded boxes. Analogous transfer-matrix calculation of TbMnO$_3$ films based on Ref. 158 and the experimental substrate data are show in **C** and **D**.

Table 7.1.   Phonon parameters fitted to describe the experimental reflectance of the YAlO$_3$ substrate assuming a simplified isotropic pseudo-crystal.

Mode	For $c \parallel x$				For $a \parallel x$			
	Ω_{TO_j}	Ω_{LO_j} [cm^{-1}]	γ_{TO_j}	γ_{LO_j}	Ω_{TO_j}	Ω_{LO_j} [cm^{-1}]	γ_{TO_j}	γ_{LO_j}
1	445	478	6	5	370	372	6	6
2	485	580	5	7	391	393	3	3
3	554	552	6	6	432	465	5	5
4		–			477	500	5	5
5		–			502	555	5	5
6		–			555.5	577	5	5
7		–			577.5	610	5	5
8		–			615	620	5	5

are found. For the employment of IR SHG spectroscopy, these signatures give a good indication as to where resonant enhancements of the nonlinear signal can be expected.

7.3.2. Field-Cooling

The general setup of cryogenic IR SHG spectroscopy has been described in Ch. 4. In order to perform IR SHG measurements on o-HoMnO$_3$ in its multiferroic phase, however, a series of technical issues has to be addressed. For instance, upon entering an ordered phase, ferroic materials form domains, i.e., regions of uniform orientation of the ferroic ordering parameter. In the case of o-HoMnO$_3$'s ferroelectric phase, these can have widths on the order of 10s of nanometers [160]. The smallest feasible IR FEL spot size, on the other hand, is on the order of a few hundred micrometers. As ferroelectric polarizations develop in opposite directions in their respective domains, the net SHG yield from the effective SHG source volume would average to zero. One possible way to overcome this limitation posed by the small domain sizes is to employ the practice of field-cooling [157, 161]. This technique involves an external poling voltage, U_{pol}, applied via two electrodes on the sample's surface. The resulting electric field, $\mathbf{E}_{\mathrm{pol}}$, causes a biased domain formation during the phase transition towards a preferential direction along $\mathbf{E}_{\mathrm{pol}}$ and, thus, a nonzero ferroelectric net polarization—detectable via IR SHG. For this purpose, Cr (30 Å)/Au (1500 Å) electrodes were deposited on the 100 nm thick o-HoMnO$_3$ sample along its principal a axis, using vapor

deposition with an electrode distance of $d = 300\,\mu m$.[2] A construction drawing as well as a photograph of the poling setup are shown in Fig. 7.5. Here, d was chosen to maximize the poling field while leaving a sufficiently large area on the sample unobstructed by the electrodes for the IR SHG probe. Another experimental limitation is posed by the cryostat setup. Considering the specification of the electrical feedthroughs to the sample chamber as well as the risk of a short circuit within the sample chamber due to the lowered breakthrough voltage in liquid helium, the poling voltage was limited to $U_{pol} \leq 300\,V$. This results in a poling field of $E_{pol} = 10\,kV\,cm^{-1}$ which—according to literature [157]—is expected to suffice for effective field-cooling of the manganite films at hand.
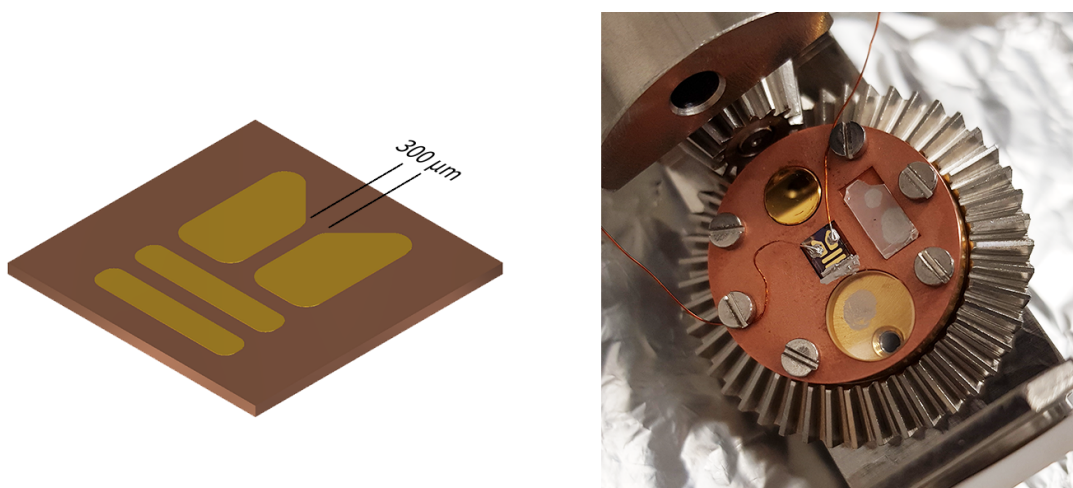
Figure 7.5. **Poling setup of the o-HoMnO$_3$ sample. Left:** Construction drawing of the o-HoMnO$_3$ sample with gold electrodes. **Right:** Photograph of the cryostat head with the mounted o-HoMnO$_3$ sample and connected electrodes. Also, gold and α-quartz samples are mounted for reference measurements as well as the YAlO$_3$ substrate.

7.3.3. Results

For the IR SHG measurements, the 100 nm thick o-HoMnO$_3$ film was mounted in the cryostat and the maximum poling voltage of $U_{pol} = 300\,V$ was applied. Then, the sample was gradually cooled down from 78 K to 1.8 K. Despite these measures to induce a nonzero ferroelectric net polarization, no onset of detectable IR SHG signal was observed. A thorough discussion of the possible reasons will be given in Sec. 7.4. Instead, a series of temperature-dependent reflectance spectra was obtained with either the a- or c-axis aligned horizontally in p-polarization under an incidence angle of 60°—analogous to the spectra shown in Fig. 7.4. The results for 300 K, 78 K, 30 K, and 1.8 K are shown in Fig. 7.6.

---

2 The vapor deposition was carried out by Sven Kubala at the Physical Chemistry Department of the FHI.
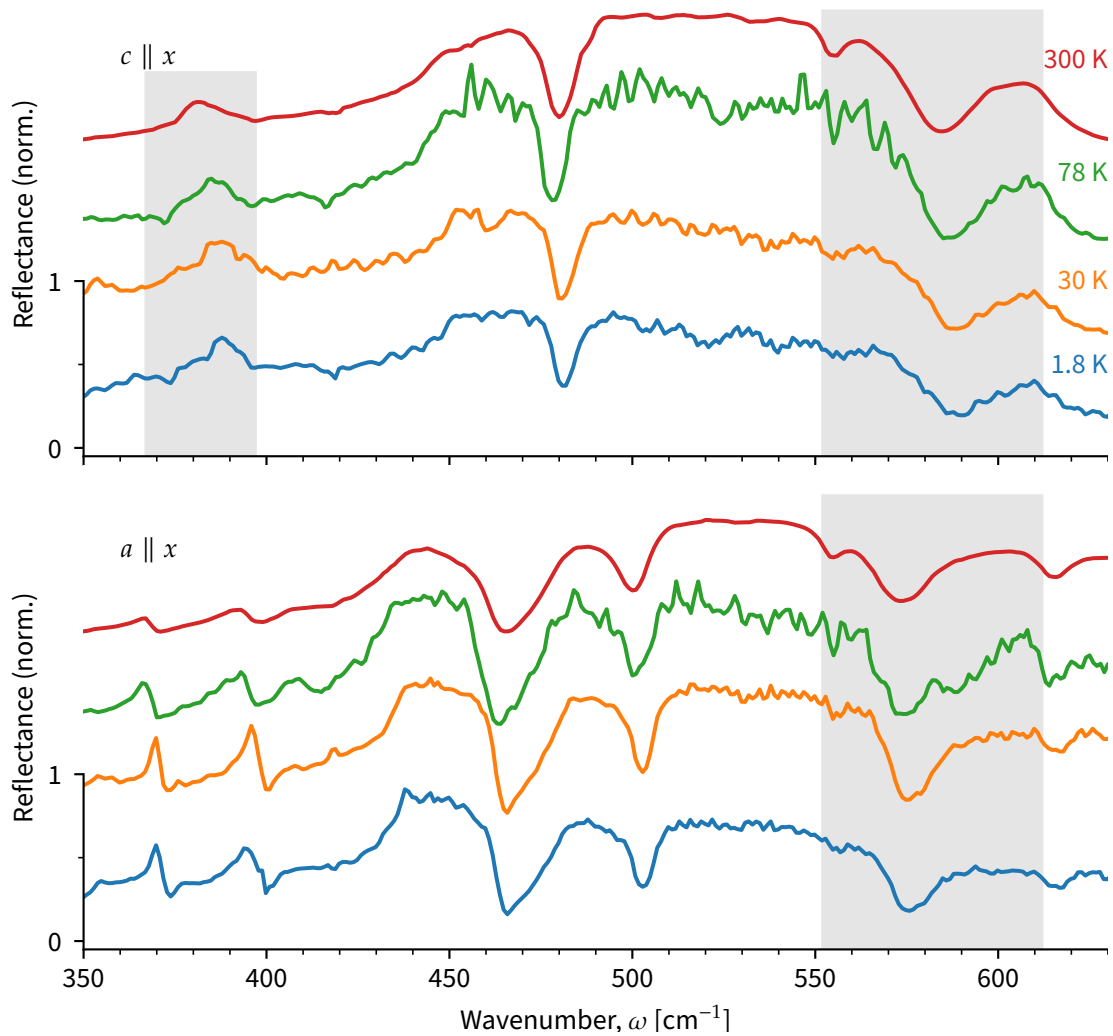
Figure 7.6. **Temperature-dependent reflectance spectra of o-HoMnO$_3$ films on a YAlO$_3$ substrate.** The spectra have been obtained for four different temperatures. The principal a axis is aligned horizontally at an incidence angle of 60° in p-polarization. Spectra are offset for clarity and spectral features specific to the o-HoMnO$_3$ film are marked by gray-shaded boxes.

Both measurement configurations reveal temperature-dependent trends, most prominently seen in the substrate's Reststrahlen bands. Here, frequency shifts as well as broadening and softening of Reststrahlen edges are present—the latter due to the expected increase in phonon damping rates at higher temperatures. The spectral features specific to the o-HoMnO$_3$ film itself which have also been observed in the room temperature spectra in Fig. 7.4, are marked by gray-shaded boxes, namely one peak between $380\,\mathrm{cm}^{-1}$ and $390\,\mathrm{cm}^{-1}$ as well as broad dips in the substrate's Reststrahlen band from $550\,\mathrm{cm}^{-1}$ to $610\,\mathrm{cm}^{-1}$ in both sample orientations. While these features persist through the entire temperature range from $1.8\,\mathrm{K}$ to room temperature, frequency shifts and shape modulations can be observed. It is likely that finer temperature steps than those employed here,

could reveal a critical behavior of the associated phonon frequencies and damping rates around the phase transition temperatures of o-HoMnO$_3$—comparable to Gervais' and Pirou's results [86] on α-quartz (see Sec. 5.5). Even though such a linear approach is expected to be sensitive to structural phase transitions in terms of phonon-related signal *variations*, nonlinear techniques, such as IR SHG, would provide a much more distinct indication in form of a signal *onset* due to the symmetry breaking at the phase transition. Moreover, the signal's characteristics carry information about the crystal symmetries and changes involved. The following section discusses possible causes as to why the IR SHG measurement did not yield any detectable signal as well as possible ways forward to implement a nonlinear IR spectroscopy for the study of phase transitions in multiferroic samples.

7.4. Discussion and Conclusion

The attempt to employ second-harmonic phonon spectroscopy for the study of phase transitions in multiferroics turned out to be very challenging and no discernible SHG signal could be detected. Various aspects need to be considered when discussing the lack of observable SHG. The most fundamental experimental limitation to be named here is the comparatively large spot size of the IR FEL excitation beam which exceeds the extent of typical ferroelectric or multiferroic domains by several orders of magnitude. This, in turn, necessitates the application of a poling field in order to enforce a preferred polarization direction of the ferroelectric domains and thus a gaugeable net polarization.

The poling voltage itself was limited by the experimental environment within the helium bath cryostat, mostly due to the lowered breakthrough voltage in liquid helium. It is possible that a larger poling voltage would lead to a larger net polarization and ultimately push the IR SHG signal above detection level. For instance, by decreasing the electrode distance, a larger poling field could be achieved. This, however, would be at the cost of the effective probing area and, thus, SHG signal. Another experimental parameter which could be further explored is the sample film thickness. For this experiment, the 100 nm thick film was chosen as it provides the largest available SHG source volume and is expected to be in a relaxed strain state which largely sustains bulk-like behavior. For thinner films, on the other hand, it has been shown that below a certain threshold thickness of $\sim$30 nm [157], significant strain develops which can strongly affect the transition temperatures of the multiferroic phase as well as the associated order parameters such as the ferroelectric polarization [162, 163]. In this regard, an increased ferroelectric polarization in a thinner film may compensate for the reduced SHG source volume and possibly lead to a detectable SHG signal.

Overall, however, the experiment presented in this chapter instructively exposed a fundamental limitation of second-harmonic phonon spectroscopy. The long MIR and FIR wavelengths strongly restrict the spatial resolution of any IR SHG measurement and therefore poses significant practical constraints on which sample systems can realistically be studied with this approach. Also, the limited sensitivity of currently available IR detectors can further hinder already challenging experiments as seen in this chapter. One promising route towards lifting these restrictions while maintaining nonlinear optical as well as IR-resonant capabilities, is the implementation of an IR-visible SFG scheme. The following chapter presents a an initial proof-of-principle SFG experiment, using the familiar α-quartz as a model system (see Ch. 5).

Chapter 8.

Sum-Frequency Generation Phonon Spectroscopy of α-Quartz

Despite being closely related to IR second-harmonic spectroscopy, from an experimental point of view, IR-visible SFG spectroscopy distinguishes itself in a few key qualities. In combining IR and visible excitations as well as signal detection in the visible, some of IR SHG's fundamental limitations—as encountered in the previous chapter—can be avoided. Specifically, the spatial resolution of SFG is determined by its visible excitation beam, allowing for substantially tighter focusing compared to IR SHG where IR laser spot sizes have been shown to be a limiting factor when studying micrometer-scale multiferroic domains (see Ch. 7). Secondly, highly sensitive detectors for the visible spectral range are widely available and facilitate single-photon detection, e.g., using PMTs, or even microscopic imaging with a charge-coupled device (CCD) camera.

This chapter exemplifies IR-visible SFG phonon spectroscopy as an alternative approach towards FEL-based nonlinear optical spectroscopy to IR SHG. The goal is to assess its feasibility in a basic proof-of-principle experiment using α-quartz as a model system which has already been well-characterized, particularly in view of its nonlinear IR properties in Ch. 5. Moreover, an outlook will be given on how the capabilities of the currently implemented SFG experiment can be further improved and expanded.

The IR-visible SFG setup used here has been developed and implemented by Riko Kießling [63] with whom these experiments were performed.

8.1. Proof-of-Concept Experiment

The general setup of an FEL-based IR-visible SFG experiment has been described in Sec. 4.3. Here, the studied sample was a c-cut α-quartz crystal. The nonlinear properties of α-quartz have been laid out in Sec. 5.1. The lower intrinsic symmetry of SFG, however, leads to additional unique $\chi^{(2)}$ elements compared to SHG.

Specifically, the contributing elements for SFG read (cf. Eq. 5.1.1) [36]:

$$\chi^{(2)}_{aaa} = -\chi^{(2)}_{abb} = -\chi^{(2)}_{bba} = -\chi^{(2)}_{bab},$$
$$\chi^{(2)}_{abc} = -\chi^{(2)}_{bac},$$
$$\chi^{(2)}_{acb} = -\chi^{(2)}_{bca},$$
$$\chi^{(2)}_{cab} = -\chi^{(2)}_{cba}.$$

$$(8.1.1)$$

In analogy to the calculations carried out in Sec. 5.1 (Eq. 5.1.3), this leads to a nonzero SFG intensity for all polarization combinations of the incoming IR and visible beams as well as the SFG signal. Here, we specifically measure the polarization conditions sss, spp, and psp. They read [32]:

$$I^{sss}_{\text{SFG}} \propto \left| L_{yy}(\omega_{\text{SFG}})\, L_{yy}(\omega_{\text{vis}}, \alpha^{\text{i}}_{\text{vis}})\, L_{yy}(\omega_{\text{IR}}, \alpha^{\text{i}}_{\text{IR}})\, \chi^{(2)}_{aaa}\, \sin(3\varphi) \right|^2 /\Delta k^2, \qquad (8.1.2a)$$

$$
\begin{aligned}
I^{spp}_{\text{SFG}} \propto \Big| & L_{yy}(\omega_{\text{SFG}})\, L_{xx}(\omega_{\text{vis}}, \alpha^{\text{i}}_{\text{vis}})\, L_{xx}(\omega_{\text{IR}}, \alpha^{\text{i}}_{\text{IR}})\, \chi^{(2)}_{aaa}\, \sin(3\varphi) \\
& - L_{yy}(\omega_{\text{SFG}})\, L_{xx}(\omega_{\text{vis}}, \alpha^{\text{i}}_{\text{vis}})\, L_{zz}(\omega_{\text{IR}}, \alpha^{\text{i}}_{\text{IR}})\, \chi^{(2)}_{abc} \\
& + L_{yy}(\omega_{\text{SFG}})\, L_{zz}(\omega_{\text{vis}}, \alpha^{\text{i}}_{\text{vis}})\, L_{xx}(\omega_{\text{IR}}, \alpha^{\text{i}}_{\text{IR}})\, \chi^{(2)}_{bca} \Big|^2 /\Delta k^2,
\end{aligned}
\qquad (8.1.2b)
$$

$$
\begin{aligned}
I^{psp}_{\text{SFG}} \propto \Big| & - L_{xx}(\omega_{\text{SFG}})\, L_{yy}(\omega_{\text{vis}}, \alpha^{\text{i}}_{\text{vis}})\, L_{xx}(\omega_{\text{IR}}, \alpha^{\text{i}}_{\text{IR}})\, \chi^{(2)}_{aaa}\, \sin(3\varphi) \\
& - L_{xx}(\omega_{\text{SFG}})\, L_{yy}(\omega_{\text{vis}}, \alpha^{\text{i}}_{\text{vis}})\, L_{zz}(\omega_{\text{IR}}, \alpha^{\text{i}}_{\text{IR}})\, \chi^{(2)}_{abc} \\
& + L_{zz}(\omega_{\text{SFG}})\, L_{yy}(\omega_{\text{vis}}, \alpha^{\text{i}}_{\text{vis}})\, L_{xx}(\omega_{\text{IR}}, \alpha^{\text{i}}_{\text{IR}})\, \chi^{(2)}_{cba} \Big|^2 /\Delta k^2.
\end{aligned}
\qquad (8.1.2c)
$$

Here, $\omega_{\text{vis(IR)}}$ and $\alpha^{\text{i}}_{\text{vis(IR)}}$ denote the frequency of the visible (IR) excitation beam and ω_{SFG} the sum-frequency. Notably, while the sss configuration involves only one $\chi^{(2)}$ tensor element, namely $\chi^{(2)}_{aaa}$, spp and psp each probe three tensor elements. Combining these three polarization conditions allows to probe all of α-quartz's unique $\chi^{(2)}$ contributions listed in Eq. 8.1.1.

The experimental spectra are shown in Fig. 8.1. In each measurement configuration, the azimuthal angle, φ, was set to yield the maximum SFG signal. All spectra reveal a distinct peak at α-quartz's ordinary $E4$ TO phonon resonance. At the frequency of the $E5$ TO resonance, on the other hand, no enhancement is observed directly. Instead, SFG peaks for psp and sss are observed with a significant blue-shift of ~35 cm^{-1} with respect to the TO phonon frequency. This is likely due to the influence of Fresnel enhancement (see Fig. 3.4) and the wave vector mismatch term associated with the $E5$ mode. Additional SFG peaks are observed

around ~535 cm^{-1} in the *spp* and ~610 cm^{-1} in both, *sss* and *spp*, which are also assumed to originate from the linear signal contributions.
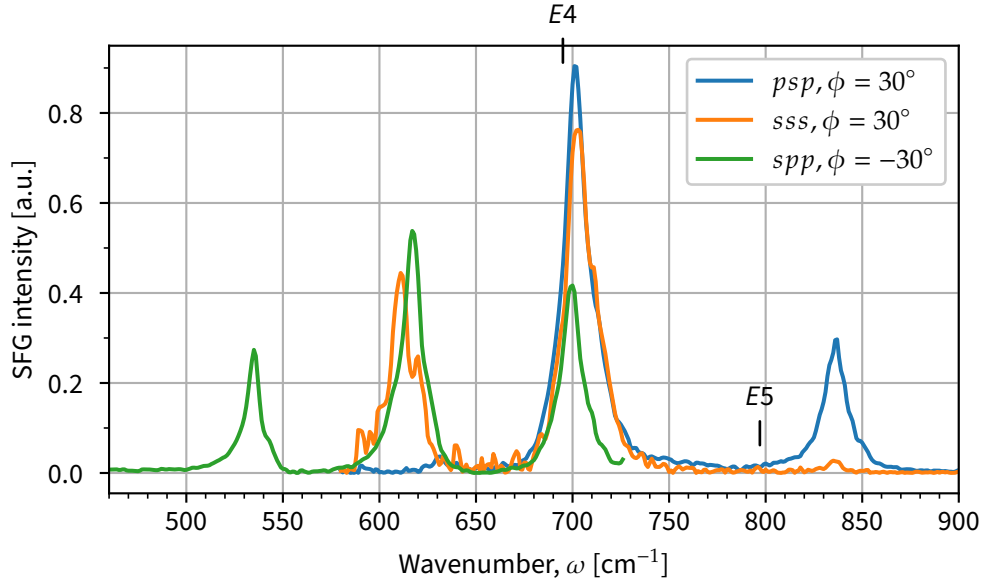
Figure 8.1. ɪʀ-ᴠɪsɪʙʟᴇ ꜱꜰɢ **phonon spectra of α-quartz.** Polarization conditions *psp*, *sss*, and *spp* yield distinct ꜱꜰɢ peaks at α-quartz's ordinary ᴛᴏ phonon resonances or associated Fresnel and wave vector mismatch enhancements. Azimuthal angles, φ, were chosen to maximize the ꜱꜰɢ signal at each measurement configuration.

In order to confirm the pronounced influence of linear optical quantities, we specifically turn to the spectrum measured in the *sss* polarization configuration as its relative simplicity, i.e., involvement of only one $\chi^{(2)}$ component (see Eq. 8.1.2a), allows for a clearer decomposition of linear and nonlinear signal contributions. Invoking Eq. 8.1.2a and the expression for the L_{yy} Fresnel transmission tensor element from Tab. 3.1 as well as the wave vector mismatch leads to the spectral dependence of all linear quantities involved. Here, the $\varepsilon(\omega)$ dispersion at optical wavelengths is assumed to be constant [164]. The ɪʀ-dispersive quantities are plotted in Figs. 8.2c and ᴅ. For the $\chi_{aaa}^{(2)}(\omega)$ dispersion, a simple model based on Eq. 3.3.7 is employed. For ꜱꜰɢ, however, only the C_1 Raman polarizability terms (Eq. 5.1.6a) contribute to the resonant $\chi^{(2)}(\omega)$ behavior. Therefore, we here neglect all C_2 and C_3 terms (Eqs. 5.1.6b and 5.1.6c), connected to higher-order lattice forces to which ɪʀ-visible ꜱꜰɢ is insensitive. A fitting procedure then adjusted the C_1 parameters such that the expression in Eq. 8.1.2a best reproduced the experimental data. This results in the $\chi_{aaa}^{(2)}$ lineshape shown in Fig. 8.2ʙ, contributing to the ꜱꜰɢ spectrum shown in Fig. 8.2ᴀ, together with the experimental data. Here, it shall be noted that the fit procedure is very sensitive to the relative ꜱꜰɢ peak amplitudes and, while generating a qualitatively good description for the comparatively simple *sss* spectrum, it lacks quantitative accuracy. This is especially true when describing the more complex *spp* and *psp* spectra (not shown here).

As a full quantitative description of the experimental data is beyond the scope of this proof-of-principle experiment, we shall in the following rely on the model fit solely for a qualitative analysis of the linear and nonlinear signal contributions.
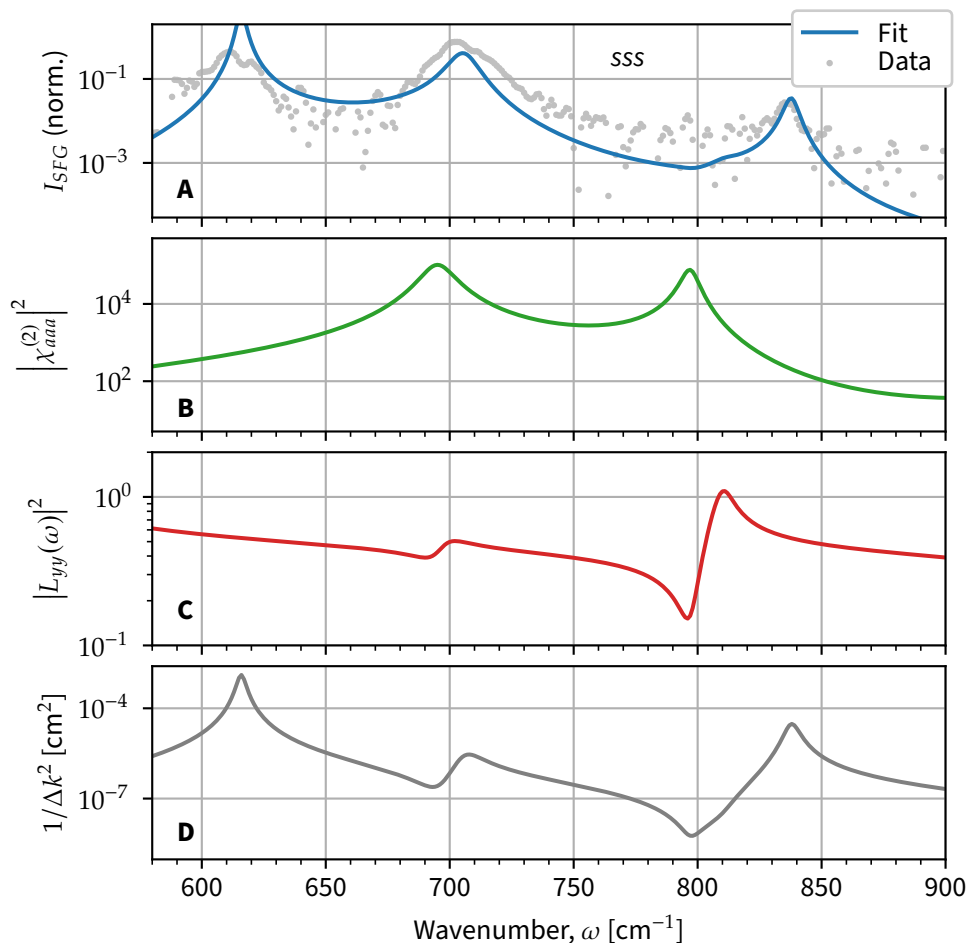
Figure 8.2. **Decomposition of the ɪʀ-visible sғɢ signal of α-quartz.** Only one $\chi^{(2)}$ tensor element **(B)** enters the sғɢ spectrum in *sss* polarization **(A)**. In addition, linear optical quantities, namely the Fresnel transmission factor **(C)** as well as the wave vector mismatch **(D)** strongly affect the appearance of sғɢ peak positions. Note the logarithmic scales in all graphs.

The decomposition of the sss spectrum shows that sғɢ peaks which cannot be assigned to α-quartz's ᴛᴏ phonon frequencies, specifically around $615\,\mathrm{cm}^{-1}$ and $835\,\mathrm{cm}^{-1}$, originate in enhancements in the wave vector mismatch term, $1/\Delta k^2$. Additionally, $\chi^{(2)}$ enhancements close to ᴛᴏ phonon frequencies, for instance at $\sim 705\,\mathrm{cm}^{-1}$, appear slightly blue-shifted due to on-resonance suppression in both, $L_{yy}(\omega)$ as well as $1/\Delta k^2$—an effect that has also been observed in the ɪʀ sʜɢ spectra of α-quartz (see Sec. 5.2).

Generally, the presence of sғɢ resonances caused by the Fresnel factors as well as the wave vector mismatch appears to be rather prominent. A possible reason

is that the detected SFG beam propagated through the α-quartz crystal before being reflected at the sample's backside and then back into air. This results in a prolonged propagation through the crystal and thereby increases the effect of the linear optical quantities in Eqs. 8.1.2a–8.1.2c—primarily Δk. In an alternative detection scheme, aimed to capture the SFG signal generated and reflected at the front face of the sample, $\chi^{(2)}$-induced enhancement effects are likely to become more prominent and thus allow for a more direct probe of the sample's phonon resonances through $\chi^{(2)}$ enhancements.

8.2. Outlook

The experimental results outlined in this chapter demonstrate a successful first proof-of-concept FEL-based SFG experiment. The acquired spectra show clear signatures of α-quartz's E-type TO phonon modes—comparable to the all-IR SHG spectra presented in Ch. 5. It should be noted, however, that the latter can grant access to higher-order lattice anharmonicities (see Eqs. 5.1.6a–5.1.6c) whereas IR-visible SFG—being only singly IR-resonant and having different selection rules—solely probes the Raman polarizability (Eq. 5.1.6a) and consequently requires resonances to be Raman-active. In the particular case of α-quartz, this means that SFG is only sensitive to the E-type vibrational modes which are both, IR- and Raman-active while SHG generally only requires IR-activity and can therefore, in principle, also probe α-quartz's A_2-type modes.

On the other hand, IR-visible SFG spectroscopy enables strongly improved spatial resolution and sensitivity thanks to its visible in- and output beams which considerably widens its application range and may even open up more elaborate detection schemes. In fact, an FEL-based IR-visible SFG wide-field microscope is currently in development [69] (see Fig. 8.3) and has shown promising initial results on SiC nanostructures. Such an approach could allow to revisit investigations of multiferroic domains like those presented in Ch. 7, but also unlock further application spaces, including surface chemistry [165] and even biological systems [166].
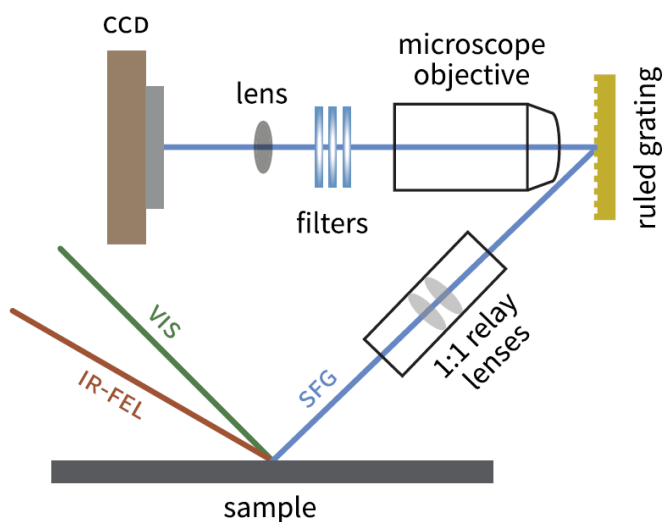
Figure 8.3. Schematic of an FEL-based wide-field microscopy setup. Here, a relay imaging scheme prevents optical distortion under oblique incidence. In addition, soft focusing immensely reduces the risk of inflicting sample damage. Reproduced from Ref. 69.

Chapter 9.

Summary and Conclusion

In this thesis, the potential of IR second-harmonic spectroscopy for the study of vibrational properties of polar dielectrics using an IR FEL has been explored. To this end, a noncollinear autocorrelator-type excitation scheme has been implemented which enables temporally and spatially coherent SHG while geometrically separating the second-harmonic from the fundamental beams. As an initial demonstration of this experimental setup, a comprehensive study of the well-characterized multimode system α-quartz has been performed. The acquired SHG spectra show distinct peaks, primarily at α-quartz's TO phonon frequencies, caused by resonantly enhanced second-order nonlinear susceptibilities, $\chi^{(2)}(\omega)$, which can be detected over several orders of magnitude. A careful analysis of these spectra showed that alongside the *nonlinear* $\chi^{(2)}$ contributions, the *linear* optical quantities—ultimately determined by the highly dispersive IR dielectric function, $\varepsilon(\omega)$—play a major role in the formation of the spectral IR SHG response as well. An accurate interpretation of second-harmonic phonon spectra therefore requires good knowledge of the sample's dielectric properties. Its high sensitivity combined with the narrow linewidth and wide tunability of an IR FEL qualifies IR SHG as a viable alternative technique to already established phonon spectroscopies such as Raman or neutron scattering.

Importantly, the nonlinear nature of SHG opens up additional experimental degrees of freedom which allow to selectively probe symmetry properties of the studied system. Specifically, by measuring the SHG intensity as a function of the sample's azimuthal angle, distinct six- and threefold patterns are observed in different polarization configurations which directly relate to α-quartz's trigonal crystal structure. In principle, the IR SHG approach also grants access to higher-order lattice anharmonicities through contributions to the nonlinear susceptibility—inaccessible by, for example, SFG. These are closely linked to phenomena such as phonon-phonon mode coupling and are thus of scientific interest. In practice, the extraction of these quantities has turned out to be challenging due to the numerous phonon modes in α-quartz which prevent a unique determination of the many free fit parameters. For simpler systems, however, accessing these

anharmonic lattice parameters may very well be feasible as it has already been demonstrated for single-mode systems such as GaAs [34] or SiC [75].

The intrinsic sensitivity to crystal symmetry triggered temperature-dependent follow-up experiments with a particular focus on quartz's α–β phase transition. Here, the temperature-dependent phonon frequencies and damping rates are well-reproduced in the IR SHG spectra and largely in good quantitative agreement with literature values. Around the phase transition temperature of T_c = 846 K, some phonon modes disappear entirely as they become IR-forbidden under the higher hexagonal symmetry in β-quartz while others show a critical behavior. These results present second-harmonic phonon spectroscopy as a potent tool for the study of structural phase transitions, owing to its intrinsic sensitivity to symmetry as well as to phonon resonances which also carry symmetry information.

While quartz's vibrational properties at room and higher temperatures have been extensively studied prior to this work, only few studies at low temperatures have been reported in the literature. Yet, second-harmonic phonon spectroscopy—especially at cryogenic temperatures—benefits from significantly lowered phonon damping rates and therefore generally higher signal levels. This has been experimentally verified by setting up a cryogenic IR SHG experiment using a helium bath cryostat. In fact, liquid helium cooling enabled the acquisition of IR SHG spectra in measurement configurations which probe only a single $\chi^{(2)}$ element and would therefore allow the determination of the respective $\chi^{(2)}(\omega)$ lineshape by dividing out the linear signal contributions. This way, it was possible to determine the $\chi^{(2)}(\omega)$ lineshapes around strong resonances while weaker resonances still fell below detection level due to additional transmissive optics introduced by the cryostat as well as increased Fresnel suppression on-resonance at lower temperatures which partly negate the improved $\chi^{(2)}$ enhancement.

These results, once again, confirmed the importance of the linear IR properties when employing SHG phonon spectroscopy. As no study of α-quartz's low-temperature IR dielectric function was found in the literature prior to this work, a series of IR reflectivity measurements has been conducted. By applying a global fit procedure to these linear spectra, measured in various geometries on a y-cut α-quartz crystal, the low-temperature IR dielectric function was extracted and revealed remarkably low damping rates in α-quartz's naturally hyperbolic spectral bands at cryogenic temperatures. These, in turn, lead to high quality factors, i.e., low optical losses, for so-called hyperbolic polariton modes which have attracted considerable interest in the nanophotonics community as they are able to support subdiffractional imaging and nanolithography applications.

While α-quartz's natural hyperbolicity constitutes an intriguing opportunity for nanophotonic systems and devices, here, an alternative approach has been pursued by studying atomic-scale semiconductor superlattices. These metama-

terials were shown to exhibit a distinct dielectric IR response, qualitatively different from each of the polar semiconductor materials they are composed of. Their unique optical properties originate in the emergence of hybrid phonon modes due to modified chemical bonding at the many layer boundaries as well as phonon confinement effects within each of the atomically thin layers. Here, second-harmonic phonon spectroscopy was able to aptly probe the hybrid phonon modes and quantify their strong dependence on the heterostructure's layer thicknesses. Corroborated by DFPT and transfer-matrix calculations, the crystalline hybrids approach presents itself as a versatile platform for user-designed hyperbolic metamaterials.

In further exploring the potential of FEL-based nonlinear optical spectroscopy for the study of functional materials—especially in view of structural phase transitions—an investigation of the multiferroic material o-$HoMnO_3$ by means of IR SHG has been attempted. This experiment proved very challenging due to the large IR spot sizes with respect to the sub-micrometer multiferroic domain sizes. Despite the applied field-cooling approach, no discernible SHG signal could be observed, revealing a fundamental constraint of the all-IR technique.

One possible way to work around the limitations of IR SHG while maintaining its nonlinear optical and IR-resonant qualities, is to employ IR-visible SFG spectroscopy. Here, the spatial resolution is determined by the visible excitation beam. Additionally, the still visible SFG signal is easily detected using PMT detectors or even imaged by CCD cameras. As a first proof-of-principle experiment, SFG spectra from the well-studied model system α-quartz have been acquired. It has been shown that even though IR-visible SFG does not probe the electrical and mechanical lattice anharmonicities due to different selection rules than IR SHG, it provides very comparable information on the sample's vibrational modes and symmetries. In return, it offers a considerably wider scope of applications, owing to its improved spatial resolution and potential for imaging microscopy.

In perspective, second-harmonic phonon spectroscopy has been shown to be a valuable tool for the study of polar dielectrics as it is highly sensitive to the breaking or change of crystal symmetries and can grant access to lattice parameters which are not easily accessible by other optical techniques. These capabilities are extremely useful when investigating order-to-order phase transitions and are likely to provide valuable physical insight in future research. In the course of the present work, however, fundamental limitations of this technique have been encountered. First and foremost, the all-IR excitation scheme considerably limits its minimal spot size and thus its achievable spatial resolution. Secondly, the inferiority of currently available IR detectors with regard to quantum efficiency compared to detectors in the visible, further hinders a broader application and the development of more sophisticated detection schemes.

Looking forward, the development of an FEL-based IR-visible SFG imaging microscope would open up wide range of applications while harnessing the qualities of IR-resonant nonlinear optics. Furthermore, with the upgrade of the FHI FEL to a two-color-IR operation mode currently under construction, IR-IR SFG experiments with two tunable IR excitation beams become feasible. To the best knowledge of the author, such measurements have not been attempted before and could possibly provide unique insight into, e.g., phonon-phonon coupling mechanisms. In fact, IR-IR SFG can be understood as a variation of IR SHG with lifted excitation beam degeneracy. Therefore, the theoretical framework for IR SHG presented in Ch. 3 as well as the experimental results of Ch. 4 lay the foundation for novel approaches of this kind.

Appendix A.

Derivation of Fresnel Coefficients in Uniaxial Crystals

In Sec. 3.2.3, the Fresnel transmission coefficients for c-cut uniaxial crystals are derived. Supplementary, we will here—in an analog fashion—derive the equivalent transmission coefficients for two particular a-cut geometries as well as the reflection coefficients for all three geometries.

Transmission Coefficients for a-Cut Crystals

For an a-cut anisotropic crystal, we here consider two special cases: (i) The crystal's optic axis, c, is aligned parallel to the x-axis and (ii) to the y-axis (cf. Fig. 3.3). Conveniently, case (i) can be treated analogous to the c-cut geometry: For p-polarized beams, $\varepsilon_\perp$ replaces $\varepsilon_\parallel$ as the out-of-plane component and vice versa for the in-plane-component. For s-polarized beams, on the other hand, the geometry is identical to the c-cut situation where only the in-plane component, i.e., $\varepsilon_\perp$ is interrogated. This leads to the following Fresnel coefficients for case (i) (cf. Eqs. 3.2.23a–A.0.9b and 3.2.27):

$$L_{xx} = \frac{2k_z^{\mathrm{t,e}}}{\varepsilon_\parallel k_z^{\mathrm{i}} + \varepsilon_0 k_z^{\mathrm{t,e}}}, \qquad (A.0.1a)$$

$$L_{zz} = \frac{\varepsilon_\parallel}{\varepsilon_\perp} \frac{2k_z^{\mathrm{i}}}{\varepsilon_\parallel k_z^{\mathrm{i}} + \varepsilon_0 k_z^{\mathrm{t,e}}}, \quad (a\text{-cut},\, c \parallel x) \qquad (A.0.1b)$$

$$L_{yy} = \frac{2k_z^{\mathrm{i}}}{k_z^{\mathrm{t,o}} + k_z^{\mathrm{i}}}. \qquad (A.0.1c)$$

with (cf. Eqs. 3.2.24 and 3.2.28):

$$k_z^{\mathrm{t,e}} = 2\pi\omega\sqrt{\varepsilon_\parallel - \frac{\varepsilon_\parallel}{\varepsilon_\perp}\sin^2\alpha_{\mathrm{i}}}, \qquad (A.0.2a)$$

$$k_z^{\mathrm{t,o}} = 2\pi\omega\sqrt{\varepsilon_\perp - \sin^2\alpha_{\mathrm{i}}}. \quad (a\text{-cut},\, c \parallel x) \qquad (A.0.2b)$$

Using the same approach, we directly find an expression for L_{yy} in case (ii) where $c \parallel y$. Here, an s-polarized beam only sees the in-plane component, namely $\varepsilon_\parallel$—as opposed to $\varepsilon_\perp$ in the c-cut geometry. Therefore (cf. Eq. 3.2.27):

$$L_{yy} = \frac{2k_z^{\mathrm{i}}}{k_z^{\mathrm{t,e}} + k_z^{\mathrm{i}}}, \quad (a\text{-cut}, c \parallel y) \tag{A.0.3}$$

with (cf. Eq. 3.2.28):

$$k_z^{\mathrm{t,e}} = 2\pi\omega\sqrt{\varepsilon_\parallel - \sin^2\alpha_{\mathrm{i}}}. \quad (a\text{-cut}, c \parallel y) \tag{A.0.4}$$

Lastly, we consider a p-polarized beam for case (ii). In this geometry, both, in- and out-of-plane components are described by $\varepsilon_\perp$ and the beam does not interact with the extraordinary $\varepsilon_\parallel$ component at all. Thus, the crystal can effectively be regarded as an isotropic medium ($\zeta = 1$). From these considerations we obtain the following expressions for L_{xx} and L_{zz} which solely depend on $\varepsilon_\perp$ (cf. Eqs. 3.2.23a–A.0.9b):

$$\left.\begin{aligned} L_{xx} &= \frac{2k_z^{\mathrm{t,o}}}{\varepsilon_\perp k_z^{\mathrm{i}} + \varepsilon_0 k_z^{\mathrm{t,o}}}, && \tag{A.0.5a} \\[2ex] L_{zz} &= \frac{2k_z^{\mathrm{i}}}{\varepsilon_\perp k_z^{\mathrm{i}} + \varepsilon_0 k_z^{\mathrm{t,o}}}, && \tag{A.0.5b} \end{aligned}\right\} \quad (a\text{-cut}, c \parallel y)$$

where $k_z^{\mathrm{t,o}}$ reads (cf. Eq. 3.2.24):

$$k_z^{\mathrm{t,o}} = 2\pi\omega\sqrt{\varepsilon_\perp - \sin^2\alpha_{\mathrm{i}}}. \quad (a\text{-cut}, c \parallel y) \tag{A.0.6}$$

Reflection Coefficients

In the same fashion, we can straightforwardly derive the Fresnel factors for reflection—again, starting with a c-cut crystal. As before, for the transmission coefficients, we invoke Maxwell's equations (Eqs. 3.2.18a–3.2.18b) and the boundary conditions for the interface (Eqs. 3.2.19a–3.2.19b). Now solving for H_y^{r} instead of H_y^{t} (Eq. 3.2.20) gives:

$$H_y^{\mathrm{r}} = \underbrace{\frac{\varepsilon_\perp k_z^{\mathrm{i}} - \varepsilon_0 k_z^{\mathrm{t}}}{\varepsilon_\perp k_z^{\mathrm{i}} + \varepsilon_0 k_z^{\mathrm{t}}}}_{\equiv F} H_y^{\mathrm{i}}. \tag{A.0.7}$$

Inserting the above expression into Eq. 3.2.18a yields:

$$E_x^{\mathrm{r}} = \frac{k_z^{\mathrm{r}}}{(2\pi\omega)^2} F\left(k_z^{\mathrm{i}} E_x^{\mathrm{i}} - k_x^{\mathrm{i}} E_z^{\mathrm{i}}\right), \tag{A.0.8a}$$

$$E_z^{\mathrm{r}} = \frac{-k_x^{\mathrm{r}}}{(2\pi\omega)^2} F\left(k_z^{\mathrm{i}} E_x^{\mathrm{i}} - k_x^{\mathrm{i}} E_z^{\mathrm{i}}\right). \tag{A.0.8b}$$

Applying the same geometrical considerations as before ($k_x^{\mathrm{i}} = 2\pi\omega \sin\alpha_{\mathrm{i}}$, $k_z^{\mathrm{i}} = 2\pi\omega \cos\alpha_{\mathrm{i}}$, $E_x^{\mathrm{i}} = E^{\mathrm{i}} \cos\alpha_{\mathrm{i}}$ and $E_z^{\mathrm{i}} = -E^{\mathrm{i}} \sin\alpha_{\mathrm{i}}$, see Fig. 3.3) as well as $k_z^{\mathrm{i}} E^{\mathrm{i}} = 2\pi\omega E_x^{\mathrm{i}}$ and $k_x^{\mathrm{i}} E^{\mathrm{i}} = -2\pi\omega E_z^{\mathrm{i}}$ leads to the following Fresnel reflection coefficients for p-polarized beams:

$$E_x^{\mathrm{r}} = -\underbrace{\frac{\varepsilon_\perp k_z^{\mathrm{i}} - k_z^{\mathrm{t,e}}}{\varepsilon_\perp k_z^{\mathrm{i}} + k_z^{\mathrm{t,e}}}}_{R_{xx}} E_x^{\mathrm{i}}, \tag{A.0.9a}$$

$$E_z^{\mathrm{r}} = \underbrace{\frac{\varepsilon_\perp k_z^{\mathrm{i}} - k_z^{\mathrm{t,e}}}{\varepsilon_\perp k_z^{\mathrm{i}} + k_z^{\mathrm{t,e}}}}_{R_{zz}} E_z^{\mathrm{i}}, \tag{A.0.9b}$$

$(c\text{-cut})$

with $k_z^{\mathrm{t,e}}$ given by Eq. 3.2.24. Analogously, we invoke Eqs. 3.2.25a, 3.2.25b, and 3.2.26a (solved for E_y^{r}) for s-polarized beams to obtain:

$$E_y^{\mathrm{r}} = \underbrace{\frac{k_z^{\mathrm{i}} - k_z^{\mathrm{t,o}}}{k_z^{\mathrm{i}} + k_z^{\mathrm{t,o}}}}_{\equiv R_{yy}} E_y^{\mathrm{i}}. \quad (c\text{-cut}) \tag{A.0.10}$$

Here, $k_z^{\mathrm{t,o}}$ is given by Eq. 3.2.28.

From these expressions, we can once again infer the analogous coefficients for the two special cases in an a-cut geometry that have been discussed earlier for the transmission factors, i.e., $c \parallel x$ and $c \parallel y$. The results are summarized in Tab. 3.1.

Appendix B.

Full Set of DFPT-Derived Phonon Modes of XH Sample B

The DFPT calculations assume an infinite AlN/GaN SL along the [0001] direction with 4 and 5 atomic monolayers of AlN and GaN in each period, respectively— closely approximating the layer thicknesses of sample B. For these numbers of monolayers, the constituent layers have opposite parity. Thus, in order to achieve appropriate bonding at the interfaces, it is necessary for the simulated unit cell to comprise two layers of each material, resulting in $N = 36$ atoms and $3N - 3 = 105$ phonon modes. Among them, 35 are doubly degenerate E-type symmetry modes and 35 A-type modes. The simulation results are listed in Tab. B.1. Here, modes 1–17 represent folded acoustic modes whereas modes 18–35 are optic phonon modes. Notably, numerous modes listed here do not contribute to the IR dielectric function due to their negligible TO–LO splittings, i.e., oscillator strengths.

In addition to the in-plane E-type modes number 27 and 34, shown in Figs. 6.4G and H of Sec. 6.3, respectively, 4 out-of-plane A-symmetry mode patterns with high oscillator strengths are shown in Fig. B.1, namely mode numbers 18, 30, 32, and 34. Here, mode 18 which contributes to the lower Reststrahlen band of $\varepsilon_\parallel(\omega)$, does not show a particular layer-confined character. Above, $\varepsilon_\parallel(\omega)$ exhibits a complex vibrational character originating in a number of different phonon modes. These modes appear to be weakly localized to the AlN layers.

Mode # =	18	30	32	34
ω_{TO} (cm^{-1}) =	537.6	756.47	799.44	816.42
ω_{LO} (cm^{-1}) =	698.87	773.99	816.4	844.91
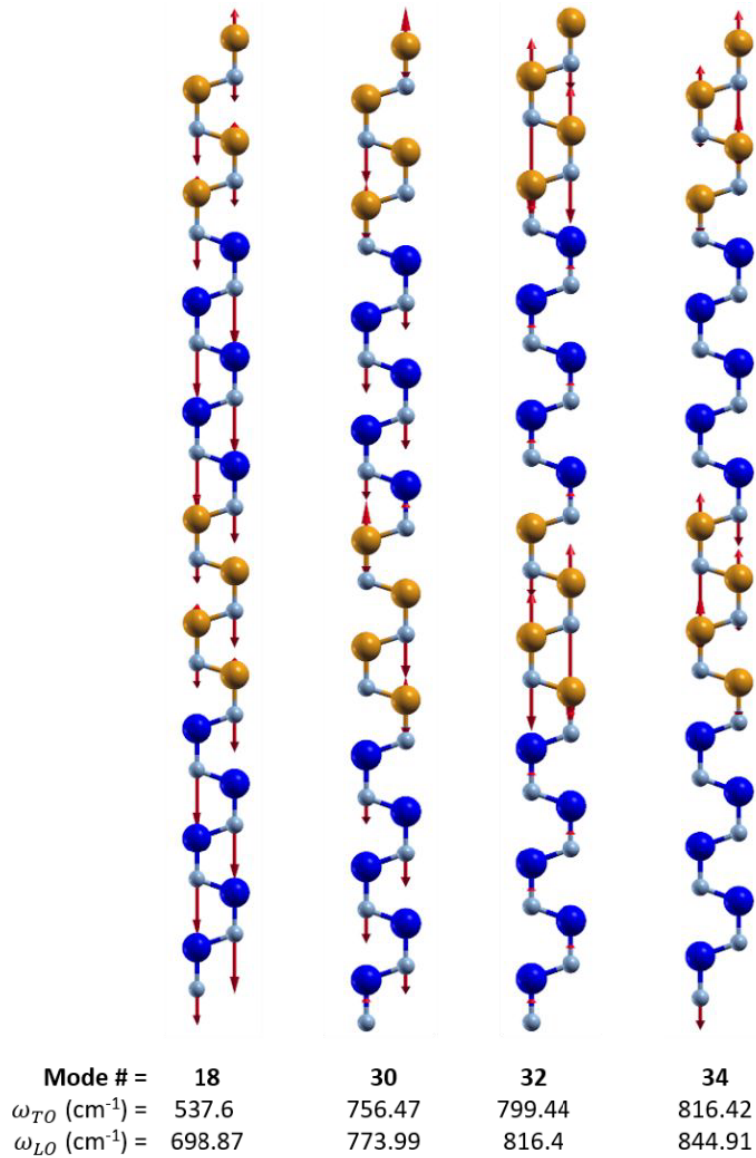
Figure B.1. **Phonon vibrational patterns of the *A*-type out-of-plane modes.** Here, blue, orange, and gray spheres represent Ga, Al, and N atoms respectively, and red arrows indicate atomic displacement. Reproduced from Ref. 105.

Table B.1. Summary of the DFPT-calculated TO and LO phonon frequencies in XH sample B. Modes 1–17 represent folded acoustic modes whereas modes 18–35 are optic phonon modes.

Mode	E-type		A-type	
	ω_{TO}	ω_{LO}	ω_{TO}	ω_{LO}
	[cm^{-1}]		[cm^{-1}]	
1	16.22	16.22	47.07	47.07
2	48.59	48.59	63.95	63.95
3	61.32	61.32	112.97	113.55
4	68.4	68.41	126.53	126.74
5	94.43	94.43	181.27	181.27
6	97.93	97.93	183.75	183.75
7	115.82	115.83	226.06	226.25
8	121.36	121.36	242.84	243.09
9	133.91	133.91	271.08	271.08
10	140.98	140.98	291.13	291.13
11	146.25	146.25	306.54	306.55
12	159.74	159.74	320.59	320.65
13	160.62	160.62	327.04	327.04
14	196.8	196.8	407.39	408.67
15	197.04	197.05	408.88	408.88
16	225.23	225.23	490.68	491.17
17	225.25	225.25	491.15	491.15
18	545.21	546.5	537.6	698.87
19	545.58	545.58	664.9	664.9
20	550.24	550.24	665.47	665.47
21	550.24	550.28	674.37	673.93
22	552.67	552.67	674.85	674.85
23	552.71	553.21	684.14	684.14
24	555.89	555.9	685.66	685.64
25	555.89	555.89	694.32	692.35
26	558.38	558.38	694.63	694.63
27	559.96	582.72	698.67	698.67
28	593	593.13	726.5	726.5
29	593.01	593.01	726.72	726.74
30	601.17	601.17	756.47	773.99
31	601.22	601.39	774.24	774.24
32	609.83	610.86	799.44	816.4
33	610.07	610.07	816.41	816.41
34	615	784.16	816.42	844.91
35	615.36	615.36	845.82	845.82

References

[1] G. S. He and S. H. Liu. *Physics of Nonlinear Optics*. World Scientific (1999). ISBN 9789810233198.

[2] T. H. Maiman. Stimulated Optical Radiation in Ruby. *Nature*, **187**(4736):493–494 (1961). doi:10.1038/187493a0.

[3] A. L. Schawlow and C. H. Townes. Infrared and Optical Masers. *Physical Review*, **112**(6):1940–1949 (1958). doi:10.1103/PhysRev.112.1940.

[4] P. A. Franken, A. E. Hill, C. W. Peters, and G. Weinreich. Generation of Optical Harmonics. *Physical Review Letters*, **7**:118–119 (1961). doi:10.1103/PhysRevLett.7.118.

[5] M. Bass, P. A. Franken, E. Hill, C. W. Peters, and G. Weinreich. Optical Mixing. *Physical Review Letters*, **8**:18–18 (1962). doi:10.1103/PhysRevLett.8.18.

[6] R. W. Terhune, P. D. Maker, and C. M. Savage. Optical Harmonic Generation in Calcite. *Physical Review Letters*, **8**:404–406 (1962). doi:10.1103/PhysRevLett.8.404.

[7] M. Bass, P. A. Franken, J. F. Ward, and G. Weinreich. Optical Rectification. *Physical Review Letters*, **9**(11):446–448 (1962). doi:10.1103/PhysRevLett.9.446.

[8] A. W. Smith and N. Braslau. Observation of an Optical Difference Frequency. *Journal of Applied Physics*, **34**(7):2105–2106 (1963). doi:10.1063/1.1729748.

[9] K. E. Niebuhr. Generation of Laser Axial Mode Difference Frequencies in a Nonlinear Dielectric. *Applied Physics Letters*, **2**(7):136–137 (1963). doi:10.1063/1.1753811.

[10] S. Haroche. Essay: Fifty Years of Atomic, Molecular and Optical Physics in Physical Review Letters. *Physical Review Letters*, **101**(16) (2008). doi:10.1103/PhysRevLett.101.160001.

[11] N. Bloembergen and P. S. Pershan. Light Waves at the Boundary of Nonlinear Media. *Physical Review*, **128**(2):606–622 (1962). doi:10.1103/PhysRev.128.606.

[12] N. Bloembergen. *Nonlinear Optics*. World Scientific (1996). doi:10.1142/3046.

[13] L. E. Hargrove, R. L. Fork, and M. A. Pollack. Locking of He-Ne Laser Modes Induced by Synchronous Intracavity Modulation. *Applied Physics Letters*, **5**(1):4–5 (1964). doi:10.1063/1.1754025.

[14] F. J. McClung and R. W. Hellwarth. Giant Optical Pulsations from Ruby. *Journal of Applied Physics*, **33**(3):828–829 (1962). doi:10.1063/1.1777174.

[15] T. W. Hänsch. Repetitively Pulsed Tunable Dye Laser for High Resolution Spectroscopy. *Applied Optics*, **11**(4):895 (1972). doi:10.1364/ao.11.000895.

[16] Z.-Y. Zhuo, C.-S. Liao, C.-H. Huang, J.-Y. Yu, Y.-Y. Tzeng, W. Lo, C.-Y. Dong, H.-C. Chui, Y.-C. Huang, and H.-M. Lai. Second Harmonic Generation Imaging – a New Method for Unraveling Molecular Information of Starch. *Journal of Structural Biology*, **171**(1):88–94 (2010). doi:10.1016/j.jsb.2010.02.020.

[17] G. Cox. Biological Applications of Second Harmonic Imaging. *Biophysical Reviews*, **3**(3):131–141 (2011). doi:10.1007/s12551-011-0052-9.

[18] W. P. Dempsey, S. E. Fraser, and P. Pantazis. SHG Nanoprobes: Advancing Harmonic Imaging in Biology. *BioEssays*, **34**(5):351–360 (2012). doi:10.1002/bies.201100106.

[19] D. M. P. Hoffmann, K. Kuhnke, and K. Kern. Sum-Frequency Generation Microscope for Opaque and Reflecting Samples. *Review of Scientific Instruments*, **73**(9):3221–3226 (2002). doi:10.1063/1.1499757.

[20] K. A. Cimatu and S. Baldelli. Chemical Microscopy of Surfaces by Sum Frequency Generation Imaging. *The Journal of Physical Chemistry C*, **113**(38):16575–16588 (2009). doi:10.1021/jp904015s.

[21] T. Kampfrath, K. Tanaka, and K. A. Nelson. Resonant and Nonresonant Control Over Matter and Light by Intense Terahertz Transients. *Nature Photonics*, **7**(9):680–690 (2013). doi:10.1038/nphoton.2013.184.

[22] T. Jiang, H. Liu, D. Huang, S. Zhang, Y. Li, X. Gong, Y.-R. Shen, W.-T. Liu, and S. Wu. Valley and Band Structure Engineering of Folded MoS_2 Bilayers. *Nature Nanotechnology*, **9**(10):825–829 (2014). doi:10.1038/nnano.2014.176.

[23] M. Fiebig, D. Fröhlich, K. Kohn, St. Leute, Th. Lottermoser, V. V. Pavlov, and R. V. Pisarev. Determination of the Magnetic Symmetry of Hexagonal Manganites by Second Harmonic Generation. *Physical Review Letters*, **84**(24):5620–5623 (2000). doi:10.1103/PhysRevLett.84.5620.

[24] P. Guyot-Sionnest, R. Superfine, J. H. Hunt, and Y.-R. Shen. Vibrational Spectroscopy of a Silane Monolayer at Air/Solid and Liquid/Solid Interfaces Using Sum-Frequency Generation. *Chemical Physics Letters*, **144**(1):1–5 (1988). doi:10.1016/0009-2614(88)87079-9.

[25] J. H. Hunt, P. Guyot-Sionnest, and Y.-R. Shen. Observation of C—H Stretch Vibrations of Monolayers of Molecules Optical Sum-Frequency Generation. *Chemical Physics Letters*, **133**(3):189–192 (1987). doi:10.1016/0009-2614(87)87049-5.

[26] P. Guyot-Sionnest, J. H. Hunt, and Y.-R. Shen. Sum-Frequency Vibrational Spectroscopy of a Langmuir Film: Study of Molecular Orientation of a Two-Dimensional System. *Physical Review Letters*, **59**(14):1597–1600 (1987). doi:10.1103/PhysRevLett.59.1597.

[27] K. B. Eisenthal. Liquid Interfaces Probed by Second-Harmonic and Sum-Frequency Spectroscopy. *Chemical Reviews*, **96**(4):1343–1360 (1996). doi:10.1021/cr9502211.

[28] M. Flörsheimer, C. Brillert, and H. Fuchs. Chemical Imaging of Interfaces by Sum Frequency Microscopy. *Langmuir*, **15**(17):5437–5439 (1999). doi:10.1021/la9815603.

[29] J. A. McGuire. Ultrafast Vibrational Dynamics at Water Interfaces. *Science*, **313**(5795):1945–1948 (2006). doi:10.1126/science.1131536.

[30] W.-T. Liu and Y.-R. Shen. Surface Vibrational Modes of α-Quartz(0001) Probed by Sum-Frequency Spectroscopy. *Physical Review Letters*, **101**:016101 (2008). doi:10.1103/PhysRevLett.101.016101.

[31] Y. Tong, J. Wirth, H. Kirsch, M. Wolf, P. Saalfrank, and R. K. Campen. Optically Probing Al–O and O–H Vibrations to Characterize Water Adsorption and Surface Reconstruction on α-Alumina: An Experimental and Theoretical Study. *The Journal of Chemical Physics*, **142**(5):054704 (2015). doi:10.1063/1.4906346.

[32] W.-T. Liu and Y.-R. Shen. Sum-Frequency Phonon Spectroscopy on α-Quartz. *Physical Review B*, **78**:024302 (2008). doi:10.1103/PhysRevB.78.024302.

[33] A. Mayer and F. Keilmann. Far-infrared Nonlinear Optics. I. $\chi^{(2)}$ Near Ionic Resonance. *Physical Review B*, **33**(10):6954–6961 (1986). doi:10.1103/PhysRevB.33.6954.

[34] T. Dekorsy, V. A. Yakovlev, W. Seidel, M. Helm, and F. Keilmann. Infrared-Phonon–Polariton Resonance of the Nonlinear Susceptibility in GaAs. *Physical Review Letters*, **90**(5) (2003). doi:10.1103/PhysRevLett.90.055508.

[35] C. Flytzanis. Infrared Dispersion of Second-Order Electric Susceptibilities in Semiconducting Compounds. *Physical Review B*, **6**:1264–1290 (1972). doi:10.1103/PhysRevB.6.1264.

[36] Y.-R. Shen. *The Principles of Nonlinear Optics*. Wiley Classics Library. Wiley-Interscience (2003). ISBN 9780471430803.

[37] C. J. Winta. *Second Harmonic Spectroscopy with an Infrared Free-Electron Laser*. Master's thesis, Freie Universität Berlin (2016). URL http://hdl.handle.net/11858/00-001M-0000-002B-4175-3.

[38] R. L. Sutherland. *Handbook of Nonlinear Optics*. Taylor & Francis Inc. (2003). ISBN 0824742435.

[39] R. W. Boyd. *Nonlinear Optics*. Academic Press (2008). ISBN 9780123694706.

[40] J. C. Maxwell. A Dynamical Theory of the Electromagnetic Field. *Philosophical Transactions of the Royal Society of London*, **155**:459–512 (1865). doi:10.1098/rstl.1865.0008.

[41] N. W. Ashcroft and N. D. Mermin. *Solid State Physics*. Cengage Learning, Inc. (1976). ISBN 0030839939.

[42] H. Kuzmany. *Solid-State Spectroscopy: An Introduction*. Springer (2013). ISBN 978-3-662-03594-8.

[43] F. Gervais and B. Piriou. Anharmonicity in Several-Polar-Mode Crystals: Adjusting Phonon Self-Energy of LO and TO Modes in Al_2O_3 and TiO_2 to Fit Infrared Reflectivity. *Journal of Physics C: Solid State Physics*, **7**(13):2374–2386 (1974). doi:10.1088/0022-3719/7/13/017.

[44] R. H. Lyddane, R. G. Sachs, and E. Teller. On the Polar Vibrations of Alkali Halides. *Physical Review*, **59**(8):673–676 (1941). doi:10.1103/PhysRev.59.673.

[45] H. Rubens and F. Kurlbaum. Anwendung der Methode der Reststrahlen zur Prüfung des Strahlungsgesetzes. *Annalen der Physik*, **309**(4):649–666 (1901). doi:10.1002/andp.19013090402.

[46] S. Adachi. *Optical Properties of Crystalline and Amorphous Semiconductors*. Springer US (1999). doi:10.1007/978-1-4615-5241-3.

[47] F. Gervais and B. Piriou. Temperature Dependence of Transverse- and Longitudinal-Optic Modes in TiO$_2$ (Rutile). *Physical Review B*, **10**(4):1642–1654 (1974). doi:10.1103/PhysRevB.10.1642.

[48] A. S. Barker. Transverse and Longitudinal Optic Mode Study in MgF$_2$ and ZnF$_2$. *Physical Review*, **136**(5A):A1290–A1295 (1964). doi:10.1103/PhysRev.136.a1290.

[49] D. W. Berreman and F. C. Unterwald. Adjusting Poles and Zeros of Dielectric Dispersion to Fit Reststrahlen of PrCl$_3$and LaCl$_3$. *Physical Review*, **174**(3):791–799 (1968). doi:10.1103/PhysRev.174.791.

[50] I. F. Chang, S. S. Mitra, N. Plendl, and L. C. Mansur. Long-Wavelength Longitudinal Phonons of Multi-Mode Crystals. *Physica Status Solidi (b)*, **28**(2):663–673 (1968). doi:10.1002/pssb.19680280224.

[51] R. P. Lowndes. Influence of Lattice Anharmonicity on the Longitudinal Optic Modes of Cubic Ionic Solids. *Physical Review B*, **1**(6):2754–2763 (1970). doi:10.1103/PhysRevB.1.2754.

[52] J. D. Caldwell, I. Aharonovich, G. Cassabois, J. H. Edgar, B. Gil, and D. N. Basov. Photonics with Hexagonal Boron Nitride. *Nature Reviews Materials*, **4**(8):552–567 (2019). doi:10.1038/s41578-019-0124-1.

[53] S. Dai, Q. Ma, T. Andersen, A. S. Mcleod, Z. Fei, M. K. Liu, M. Wagner, K. Watanabe, T. Taniguchi, M. Thiemens, F. Keilmann, P. Jarillo-Herrero, M. M. Fogler, and D. N. Basov. Subdiffractional Focusing and Guiding of Polaritonic Rays in a Natural Hyperbolic Material. *Nature Communications*, **6**(1) (2015). doi:10.1038/ncomms7963.

[54] Z. Jacob. Hyperbolic Phonon–Polaritons. *Nature Materials*, **13**(12):1081–1083 (2014). doi:10.1038/nmat4149.

[55] L. D. Landau, J. S. Bell, M. J. Kearsley, L. P. Pitaevskii, E. M. Lifshitz, and J. B. Sykes. *Electrodynamics of Continuous Media*, volume 8. Elsevier (1984). ISBN 9780750626347.

[56] Y.-R. Shen. Optical Second Harmonic Generation at Interfaces. *Annual Review of Physical Chemistry*, **40**(1):327–350 (1989). doi:10.1146/annurev.pc.40.100189.001551.

[57] A. Paarmann, I. Razdolski, S. Gewinner, W. Schöllkopf, and M. Wolf. Effects of Crystal Anisotropy on Optical Phonon Resonances in Midinfrared Second Harmonic Response of SiC. *Physical Review B*, **94**:134312 (2016). doi:10.1103/PhysRevB.94.134312.

[58] L. P. Mosteller, Jr. and F. Wooten. Optical Properties and Reflectance of Uni-axial Absorbing Crystals. *Journal of the Optical Society of America*, **58**(4):511–518 (1968). doi:10.1364/JOSA.58.000511.

[59] K. Huang M. Born. *Dynamical Theory of Crystal Lattices*. OUP Oxford (1998). ISBN 0198503695. URL https://www.ebook.de/de/product/3659498/max_born_kun_huang_dynamical_theory_of_crystal_lattices.html.

[60] J. A. Armstrong, N. Bloembergen, J. Ducuing, and P. S. Pershan. Interactions between Light Waves in a Nonlinear Dielectric. *Physical Review*, **127**(6):1918–1939 (1962). doi:10.1103/PhysRev.127.1918.

[61] W. L. Faust and Charles H. Henry. Mixing of Visible and Near-Resonance Infrared Light in GaP. *Physical Review Letters*, **17**:1265–1268 (1966). doi:10.1103/PhysRevLett.17.1265.

[62] E. Roman, J. R. Yates, Mm Veithen, D. Vanderbilt, and I. Souza. Ab Initio Study of the Nonlinear Optics of III-V Semiconductors in the Terahertz Regime. *Physical Review B*, **74**:245204 (2006). doi:10.1103/PhysRevB.74.245204.

[63] Riko Kiessling. *Optical Sum-Frequency Response of Lattice Vibrations and Pulse Timing at a Free-Electron Laser*. Ph.D. thesis, Freie Universität Berlin (2020). doi:10.17169/refubium-28042.

[64] W. Schöllkopf, S. Gewinner, H. Junkes, A. Paarmann, G. v. von Helden, H. Bluem, and A. M. M. Todd. The new IR and THz FEL facility at the Fritz Haber Institute in Berlin. *Proc. SPIE*, **9512**:95121L–95121L–13 (2015). doi:10.1117/12.2182284.

[65] O. Svelto. *Principles of Lasers*. Springer US, 5th edition (2010). doi:10.1007/978-1-4419-1302-9.

[66] T. Shiozawa. *Classical Relativistic Electrodynamics—Theory of Light Emission and Application to Free Electron Lasers*. Springer-Verlag Berlin Heidelberg (2004). doi:10.1007/978-3-662-06261-6.

[67] Christopher J. Winta, Sandy Gewinner, Wieland Schöllkopf, Martin Wolf, and Alexander Paarmann. Second harmonic phonon spectroscopy of α-quartz. In *Conference on Lasers and Electro-Optics*. The Optical Society (2016). doi:10.1364/CLEO_QELS.2016.FTu4A.5.

[68] S. Varró, editor. *Free Electron Lasers*. InTech (2012).

[69] R. Kiessling, W. B. Colson, S. Gewinner, W. Schöllkopf, M. Wolf, and A. Paarmann. Femtosecond Single-Shot Timing and Direct Observation of Subpulse Formation in an Infrared Free-Electron Laser. *Physical Review Accelerators and Beams*, **21**(8) (2018). doi:10.1103/PhysRevAccelBeams.21.080702.

[70] CryoVac GmbH & Co KG. KONTI-*Kryostat IT Typ Spektro 3—Operations Manual* (2017).

[71] C. J. Winta, S. Gewinner, W. Schöllkopf, M. Wolf, and A. Paarmann. Second-Harmonic Phonon Spectroscopy of α-Quartz. *Physical Review B*, **97**(9) (2018). doi:10.1103/PhysRevB.97.094108.

[72] C. J. Winta, M. Wolf, and A. Paarmann. Low-Temperature Infrared Dielectric Function of Hyperbolic α-Quartz. *Physical Review B*, **99**(14) (2019). doi:10.1103/PhysRevB.99.144308.

[73] J. Nordlander, G. De Luca, N. Strkalj, M. Fiebig, and M. Trassin. Probing Ferroic States in Oxide Thin Films Using Optical Second Harmonic Generation. *Applied Sciences*, **8**(4):570 (2018). doi:10.3390/app8040570.

[74] L. Zhao, D. Torchinsky, J. H., A. de la Torre, and D. Hsieh. Second Harmonic Generation Spectroscopy of Hidden Phases. pages 207–226 (2018). doi:10.1016/b978-0-12-803581-8.09533-3.

[75] A. Paarmann, I. Razdolski, A. Melnikov, S. Gewinner, W. Schöllkopf, and M. Wolf. Second Harmonic Generation Spectroscopy in the Reststrahl Band of SiC Using an Infrared Free-Electron Laser. *Applied Physics Letters*, **107**(8):081101 (2015). doi:10.1063/1.4929358.

[76] R. S. Anderson and S. P. Anderson. *Geomorphology: The Mechanics and Chemistry of Landscapes*. Cambridge University Press (2010). ISBN 9781139788700.

[77] A. Bosak, M. Krisch, D. Chernyshov, B. Winkler, V. Milman, K. Refson, and C. Schulze-Briese. New insights into the lattice dynamics of α-quartz. *Zeitschrift für Kristallographie*, **227**(2):84–91 (2012). doi:10.1524/zkri.2012.1432.

[78] R. S. Krishnan. Raman Spectrum of Quartz. *Nature*, **155**(3937):452–452 (1945). doi:10.1038/155452a0.

[79] S. Ichikawa, J. Suda, T. Sato, and Y. Suzuki. Lattice Dynamics and Temperature Dependence of the First-Order Raman Spectra for α-SiO$_2$ Crystals. *Journal of Raman Spectroscopy*, **34**(2):135–141 (2003). doi:10.1002/jrs.966.

[80] W. G. Spitzer and D. A. Kleinman. Infrared Lattice Bands of Quartz. *Physical Review*, **121**(5):1324–1335 (1961). doi:10.1103/PhysRev.121.1324.

[81] B. Dorner, H. Grimm, and H. Rzany. Phonon Dispersion Branches in α Quartz. *Journal of Physics C: Solid State Physics*, **13**(36):6607–6613 (1980). doi:10.1088/0022-3719/13/36/014.

[82] D. Strauch and B. Dorner. Lattice Dynamics of α-Quartz. I. Experiment. *Journal of Physics: Condensed Matter*, **5**(34):6149–6154 (1993). doi:10.1088/0953-8984/5/34/003.

[83] K. H. W. Bauer, H. Jagodzinski, B. Dorner, and H. Grimm. The Inelastic Nature of Diffuse X-Ray Scattering near the α-β Transition in Quartz. *Physica Status Solidi (b)*, **48**(1):437–443 (1971). doi:10.1002/pssb.2220480143.

[84] K. Momma and F. Izumi. VESTA3 for Three-Dimensional Visualization of Crystal, Volumetric and Morphology Data. *Journal of Applied Crystallography*, **44**(6):1272–1276 (2011). doi:10.1107/S0021889811038970.

[85] A. F. Wright and M. S. Lehmann. The Structure of Quartz at 25 and 590 °C Determined by Neutron Diffraction. *Journal of Solid State Chemistry*, **36**(3):371 – 380 (1981). doi:10.1016/0022-4596(81)90449-7.

[86] F. Gervais and B. Piriou. Temperature Dependence of Transverse and Longitudinal Optic Modes in the α and β Phases of Quartz. *Physical Review B*, **11**:3944–3950 (1975). doi:10.1103/PhysRevB.11.3944.

[87] J. F. Scott and S. P. S. Porto. Longitudinal and Transverse Optical Lattice Vibrations in Quartz. *Physical Review*, **161**(3):903–910 (1967). doi:10.1103/PhysRev.161.903.

[88] C. L. Davies, J. B. Patel, C. Q. Xia, L. M. Herz, and M. B. Johnston. Temperature-Dependent Refractive Index of Quartz at Terahertz Frequencies. *Journal of Infrared, Millimeter, and Terahertz Waves*, **39**(12):1236–1248 (2018). doi:10.1007/s10762-018-0538-7.

[89] K. Wood. Private communication (2019). QMC Instruments Ltd.

[90] R. E. da Silva, R. Macêdo, T. Dumelow, J. A. P. da Costa, S. B. Honorato, and A. P. Ayala. Far-Infrared Slab Lensing and Subwavelength Imaging in Crystal Quartz. *Physical Review B*, **86**(15) (2012). doi:10.1103/PhysRevB.86.155152.

[91] N. C. Passler and A. Paarmann. Generalized 4 × 4 Matrix Formalism for Light Propagation in Anisotropic Stratified Media: Study of Surface Phonon Polaritons in Polar Dielectric Heterostructures. *Journal of the Optical Society of America B*, **34**(10):2128 (2017). doi:10.1364/JOSAB.34.002128.

[92] Y. Guo, W. Newman, C. L. Cortes, and Z. Jacob. Applications of Hyperbolic Metamaterial Substrates. *Advances in OptoElectronics*, **2012**:1–9 (2012). doi:10.1155/2012/452502.

[93] J. D. Caldwell, A. V. Kretinin, Y. Chen, V. Giannini, M. M. Fogler, Y. Francescato, C. T. Ellis, J. G. Tischler, C. R. Woods, A. J. Giles, M. Hong, K. Watanabe, T. Taniguchi, S. A. Maier, and K. S. Novoselov. Sub-Diffractional Volume-Confined Polaritons in the Natural Hyperbolic Material Hexagonal Boron Nitride. *Nature Communications*, **5**(1) (2014). doi:10.1038/ncomms6221.

[94] P. Li, I. Dolado, F. J. Alfaro-Mozaz, F. Casanova, L. E. Hueso, S. Liu, J. H. Edgar, A. Y. Nikitin, S. Vélez, and R. Hillenbrand. Infrared Hyperbolic Metasurface Based on Nanostructured Van Der Waals Materials. *Science*, **359**(6378):892–896 (2018). doi:10.1126/science.aaq1704.

[95] W. Ma, P. Alonso-González, S. Li, A. Y. Nikitin, J. Yuan, J. Martín-Sánchez, J. Taboada-Gutiérrez, I. Amenabar, P. Li, S. Vélez, C. Tollan, Z. Dai, Y. Zhang, S. Sriram, K. Kalantar-Zadeh, S.-T. Lee, R. Hillenbrand, and Q. Bao. In-Plane Anisotropic and Ultra-Low-Loss Polaritons in a Natural Van Der Waals Crystal. *Nature*, **562**(7728):557–562 (2018). doi:10.1038/s41586-018-0618-9.

[96] Z. Liu, H. Lee, Y. Xiong, C. Sun, and X. Zhang. Far-Field Optical Hyperlens Magnifying Sub-Diffraction-Limited Objects. *Science*, **315**(5819):1686–1686 (2007). doi:10.1126/science.1137368.

[97] Y. Xiong, Z. Liu, and X. Zhang. A Simple Design of Flat Hyperlens for Lithography and Imaging with Half-Pitch Resolution Down to 20 nm. *Applied Physics Letters*, **94**(20):203108 (2009). doi:10.1063/1.3141457.

[98] I. G. Polyakova. *Glass: Selected Properties and Crystallization*. DE GRUYTER (2014). doi:10.1515/9783110298581.

[99] C. J. Winta, Martin Wolf, and Alexander Paarmann. Script for Calculating the Temperature-Dependent Infrared Dielectric Tensor of α-Quartz (2019). doi:10.5281/ZENODO.2560324.

[100] F. Wang and Y.-R. Shen. General Properties of Local Plasmons in Metal Nanostructures. *Physical Review Letters*, **97**(20) (2006). doi:10.1103/PhysRevLett.97.206806.

[101] J. D. Caldwell, L. Lindsay, V. Giannini, I. Vurgaftman, T. L. Reinecke, S. A. Maier, and O. J. Glembocki. Low-Loss, Infrared and Terahertz Nanophotonics Using Surface Phonon Polaritons. *Nanophotonics*, **4**(1):44–68 (2015). doi:10.1515/nanoph-2014-0003.

[102] A. J. Giles, S. Dai, I. Vurgaftman, T. Hoffman, Song Liu, Lucas Lindsay, Chase T. Ellis, Nathanael Assefa, Ioannis Chatzakis, Thomas L. Reinecke, J. G. Tischler, M. M. Fogler, J. H. Edgar, D. N. Basov, and J. D. Caldwell. Ultralow-Loss Polaritons in Isotopically Pure Boron Nitride. *Nature Materials*, **17**(2):134–139 (2018). doi:10.1038/nmat5047.

[103] S. Dai, Z. Fei, Q. Ma, A. S. Rodin, M. Wagner, A. S. McLeod, M. K. Liu, W. Gannett, W. Regan, K. Watanabe, T. Taniguchi, M. Thiemens, G. Dominguez, A. H. C. Neto, A. Zettl, F. Keilmann, P. Jarillo-Herrero, M. M. Fogler, and D. N. Basov. Tunable Phonon Polaritons in Atomically Thin Van Der Waals Crystals of Boron Nitride. *Science*, **343**(6175):1125–1129 (2014). doi:10.1126/science.1246833.

[104] S. Dai, Q. Ma, M. K. Liu, T. Andersen, Z. Fei, M. D. Goldflam, M. Wagner, K. Watanabe, T. Taniguchi, M. Thiemens, F. Keilmann, G. C. A. M. Janssen, S-E. Zhu, P. Jarillo-Herrero, M. M. Fogler, and D. N. Basov. Graphene on Hexagonal Boron Nitride as a Tunable Hyperbolic Metamaterial. *Nature Nanotechnology*, **10**(8):682–686 (2015). doi:10.1038/nnano.2015.131.

[105] D. C. Ratchford, C. J. Winta, I. Chatzakis, C. T. Ellis, N. C. Passler, J. Winterstein, P. Dev, I. Razdolski, J. R. Matson, J. R. Nolen, J. G. Tischler, I. Vurgaftman, M. B. Katz, N. Nepal, M. T. Hardy, J. A. Hachtel, J.-C. Idrobo, T. L. Reinecke, A. J. Giles, D. S. Katzer, N. D. Bassim, R. M. Stroud, M. Wolf, A. Paarmann, and J. D. Caldwell. Controlling the Infrared Dielectric Function through Atomic-Scale Heterostructures. *ACS Nano*, **13**(6):6730–6741 (2019). doi:10.1021/acsnano.9b01275.

[106] A. V. Zayats, I. I. Smolyaninov, and A. A. Maradudin. Nano-Optics of Surface Plasmon Polaritons. *Physics Reports*, **408**(3-4):131–314 (2005). doi:10.1016/j.physrep.2004.11.001.

[107] T. G. Folland, L. Nordin, D. Wasserman, and J. D. Caldwell. Probing Polaritons in the Mid- to Far-Infrared. *Journal of Applied Physics*, **125**(19):191102 (2019). doi:10.1063/1.5090777.

[108] W.-T. Liu and Y.-R. Shen. Sum-Frequency Spectroscopy on Bulk and Surface Phonons of Noncentrosymmetric Crystals. *Annalen der Physik*, **523**(1-2):101–106 (2010). doi:10.1002/andp.201000093.

[109] M. Autore, P. Li, I. Dolado, F. J. Alfaro-Mozaz, R. Esteban, A. Atxabal, F. Casanova, L. E. Hueso, P. Alonso-González, J. Aizpurua, A. Y. Nikitin, S. Vélez, and R. Hillenbrand. Boron Nitride Nanoresonators for Phonon-Enhanced Molecular Vibrational Spectroscopy at the Strong

Coupling Limit. *Light: Science & Applications*, **7**(4):17172–17172 (2017). doi:10.1038/lsa.2017.172.

[110] S. D. Jackson. Towards High-Power Mid-Infrared Emission from a Fibre Laser. *Nature Photonics*, **6**(7):423–431 (2012). doi:10.1038/nphoton.2012.149.

[111] J. B. Khurgin. How to Deal with the Loss in Plasmonics and Metamaterials. *Nature Nanotechnology*, **10**(1):2–6 (2015). doi:10.1038/nnano.2014.310.

[112] T. G. Folland and J. D. Caldwell. Chapter 12: Semiconductor Nanophotonics Using Surface Polaritons. In NATO *Science for Peace and Security Series B: Physics and Biophysics*, pages 235–254. Springer Netherlands (2018). doi:10.1007/978-94-024-1544-5_12.

[113] I. Vurgaftman, J. R. Meyer, and L. R. Ram-Mohan. Band Parameters for III–V Compound Semiconductors and Their Alloys. *Journal of Applied Physics*, **89**(11):5815–5875 (2001). doi:10.1063/1.1368156.

[114] M. Cardona and P. Y. Yu. *Fundamentals of Semiconductors*. Springer (2005).

[115] T. R. Paudel and W. R. L. Lambrecht. Computational Study of Phonon Modes in Short-Period AlN/GaN Superlattices. *Physical Review B*, **80**(10) (2009). doi:10.1103/physrevb.80.104202.

[116] R. Enderlein, D. Suisky, and J. Röseler. Optical Phonons in Superlattices. *physica status solidi (b)*, **165**(1):9–66 (1991). doi:10.1002/pssb.2221650102.

[117] J. D. Caldwell and K S. Novoselov. Mid-Infrared Nanophotonics. *Nature Materials*, **14**(4):364–366 (2015). doi:10.1038/nmat4252.

[118] J. D. Caldwell, I. Vurgaftman, J. G. Tischler, O. J. Glembocki, J. C. Owrutsky, and T. L. Reinecke. Atomic-Scale Photonic Hybrids for Mid-Infrared and Terahertz Nanophotonics. *Nature Nanotechnology*, **11**(1):9–15 (2016). doi:10.1038/nnano.2015.305.

[119] L. E. McNeil, M. Grimsditch, and R. H. French. Vibrational Spectroscopy of Aluminum Nitride. *Journal of the American Ceramic Society*, **76**(5):1132–1136 (1993). doi:10.1111/j.1151-2916.1993.tb03730.x.

[120] T. Azuhata, T. Sota, K. Suzuki, and S. Nakamura. Polarized Raman Spectra in GaN. *Journal of Physics: Condensed Matter*, **7**(10):L129–L133 (1995). doi:10.1088/0953-8984/7/10/002.

[121] H. Harima, S. Nakashima, and T. Uemura. Raman Scattering from Anisotropic LO-Phonon–Plasmon–Coupled Mode in *n*-Type 4H– and 6H–SiC. *Journal of Applied Physics*, **78**(3):1996–2005 (1995). doi:10.1063/1.360174.

[122] M. Cardona, G. Güntherodt, and G. Abstreiter. *Light Scattering in Solids V: Superlattices and Other Microstructures*, volume 66. Springer (1989).

[123] J. Gleize, F. Demangeot, J. Frandon, M. A. Renucci, F. Widmann, and B. Daudin. Phonons in a Strained Hexagonal GaN–AlN Superlattice. *Applied Physics Letters*, **74**(5):703–705 (1999). doi:10.1063/1.122993.

[124] J. Gleize, M. A. Renucci, J. Frandon, and F. Demangeot. Anisotropy Effects on Polar Optical Phonons in Wurtzite GaN/AlN Superlattices. *Physical Review B*, **60**(23):15985–15992 (1999). doi:10.1103/physrevb.60.15985.

[125] M. F. MacMillan, R. P. Devaty, W. J. Choyke, M. A. Khan, and J. Kuznia. Infrared Reflectance of AlN–GaN Short Period Superlattice Films. *Journal of Applied Physics*, **80**(4):2372–2377 (1996). doi:10.1063/1.363072.

[126] M. B. Smirnov. Vibrational Spectra of AlN/GaN Superlattices: Theory and Experiment. *Physics of the Solid State*, **47**(4):742 (2005). doi:10.1134/1.1913991.

[127] M. Schubert. *Infrared Ellipsometry on Semiconductor Layer Structures: Phonons, Plasmons, and Polaritons*, volume 209. Springer Science & Business Media (2004). ISBN 3-540-23249-4.

[128] M. Schubert, T. Hofmann, and Jan Šik. Long-Wavelength Interface Modes in Semiconductor Layer Structures. *Physical Review B*, **71**(3) (2005). doi:10.1103/physrevb.71.035324.

[129] D. W. Berreman. Infrared Absorption at Longitudinal Optic Frequency in Cubic Crystal Films. *Physical Review*, **130**(6):2193–2198 (1963). doi:10.1103/physrev.130.2193.

[130] S. Vassant, J.-P. Hugonin, F. Marquier, and J.-J. Greffet. Berreman Mode and Epsilon Near Zero Mode. *Optics Express*, **20**(21):23971 (2012). doi:10.1364/oe.20.023971.

[131] S. Campione, I. Brener, and F. Marquier. Theory of Epsilon-Near-Zero Modes in Ultrathin Films. *Physical Review B*, **91**(12) (2015). doi:10.1103/physrevb.91.121408.

[132] N. C. Passler, I. Razdolski, D. S. Katzer, D. F. Storm, J. D. Caldwell, M. Wolf, and A. Paarmann. Second Harmonic Generation from Phononic Epsilon-Near-Zero Berreman Modes in Ultrathin Polar Crystal Films. *ACS Photonics*, **6**(6):1365–1371 (2019). doi:10.1021/acsphotonics.9b00290.

[133] V. Darakchieva, E. Valcheva, P. P. Paskov, M. Schubert, T. Paskova, B. Monemar, H. Amano, and I. Akasaki. Phonon Mode Behavior in

Strained wurtziteAlN/GaNsuperlattices. *Physical Review B*, **71**(11) (2005). doi:10.1103/physrevb.71.115329.

[134] A. Poddubny, I. Iorsh, P. Belov, and Y. Kivshar. Hyperbolic Metamaterials. *Nature Photonics*, **7**(12):948–957 (2013). doi:10.1038/nphoton.2013.243.

[135] N. C. Passler, I. Razdolski, S. Gewinner, W. Schöllkopf, M. Wolf, and A. Paarmann. Second-Harmonic Generation from Critically Coupled Surface Phonon Polaritons. *ACS Photonics*, **4**(5):1048–1053 (2017). doi:10.1021/acsphotonics.7b00118.

[136] P. Li, M. Lewin, A. V. Kretinin, J. D. Caldwell, K. S. Novoselov, T. Taniguchi, K. Watanabe, F. Gaussmann, and T. Taubner. Hyperbolic Phonon-Polaritons in Boron Nitride for Near-Field Optical Imaging and Focusing. *Nature Communications*, **6**(1) (2015). doi:10.1038/ncomms8507.

[137] S. Ishii, A. V. Kildishev, E. Narimanov, V. M. Shalaev, and V. P. Drachev. Sub-Wavelength Interference Pattern from Volume Plasmon Polaritons in a Hyperbolic Medium. *Laser & Photonics Reviews*, **7**(2):265–271 (2013). doi:10.1002/lpor.201200095.

[138] A. J. Giles, S. Dai, O. J. Glembocki, A. V. Kretinin, Z. Sun, C. T. Ellis, J. G. Tischler, T. Taniguchi, K. Watanabe, M. M. Fogler, K. S. Novoselov, D. N. Basov, and J. D. Caldwell. Imaging of Anomalous Internal Reflections of Hyperbolic Phonon-Polaritons in Hexagonal Boron Nitride. *Nano Letters*, **16**(6):3858–3865 (2016). doi:10.1021/acs.nanolett.6b01341.

[139] J. D. Caldwell, I. Aharonovich, G. Cassabois, J. H. Edgar, B. Gil, and D. N. Basov. Photonics with Hexagonal Boron Nitride. *Nature Reviews Materials*, **4**(8):552–567 (2019). doi:10.1038/s41578-019-0124-1.

[140] F. Genereux, S. W. Leonard, H. M. van Driel, A. Birner, and U. Gösele. Large Birefringence in Two-Dimensional Silicon Photonic Crystals. *Physical Review B*, **63**(16) (2001). doi:10.1103/physrevb.63.161101.

[141] N. C. Passler, A. Heßler, M. Wuttig, T. Taubner, and A. Paarmann. Surface polariton-like s-polarized waveguide modes in switchable dielectric thin films on polar crystals. *Advanced Optical Materials*, **8**(5):1901056 (2019). doi:10.1002/adom.201901056.

[142] T. Taubner, D. Korobkin, Y. Urzhumov, G. Shvets, and R. Hillenbrand. Near-Field Microscopy Through a SiC Superlens. *Science*, **313**(5793):1595–1595 (2006). doi:10.1126/science.1131025.

[143] M. Fiebig, Victor V. Pavlov, and Roman V. Pisarev. Second-Harmonic Generation as a Tool for Studying Electronic and Magnetic Structures of Crystals: Review. *Journal of the Optical Society of America B*, **22**(1):96 (2005). doi:10.1364/josab.22.000096.

[144] J. Valasek. Piezo-Electric and Allied Phenomena in Rochelle Salt. *Physical Review*, **17**(4):475–481 (1921). doi:10.1103/PhysRev.17.475.

[145] M. Fiebig, T. Lottermoser, D. Meier, and M. Trassin. The Evolution of Multiferroics. *Nature Reviews Materials*, **1**:16046 (2016). doi:10.1038/NatRevMats.2016.46.

[146] N. A. Spaldin. Multiferroics: Past, Present, and Future. *MRS Bulletin*, **42**(05):385–390 (2017). doi:10.1557/mrs.2017.86.

[147] O. Auciello, J. F. Scott, and R. Ramesh. The Physics of Ferroelectric Memories. *Physics Today*, **51**(7):22–27 (1998). doi:10.1063/1.882324.

[148] H. Schmid. Multi-Ferroic Magnetoelectrics. *Ferroelectrics*, **162**(1):317–338 (1994). doi:10.1080/00150199408245120.

[149] M. Bibes and A. Barthélémy. Towards a Magnetoelectric Memory. *Nature Materials*, **7**(6):425–426 (2008). doi:10.1038/nmat2189.

[150] N. A. Hill. Why Are There so Few Magnetic Ferroelectrics? *The Journal of Physical Chemistry B*, **104**(29):6694–6709 (2000). doi:10.1021/jp000114x.

[151] J.-S. Zhou, J. B. Goodenough, J. M. Gallardo-Amores, E. Morán, M. A. Alario-Franco, and R. Caudillo. Hexagonal Versus Perovskite Phase of Manganite $RMnO_3$ (R = Y, Ho, Er, Tm, Yb, Lu). *Physical Review B*, **74**(1) (2006). doi:10.1103/PhysRevB.74.014422.

[152] S. Harikrishnan, S. Rößler, C. M. Naveen Kumar, H. L. Bhat, U. K. Rößler, S. Wirth, F. Steglich, and S. Elizabeth. Phase Transitions and Rare-Earth Magnetism in Hexagonal and Orthorhombic $DyMnO_3$ Single Crystals. *Journal of Physics: Condensed Matter*, **21**(9):096002 (2009). doi:10.1088/0953-8984/21/9/096002.

[153] N. S. Fedorova, Y. W. Windsor, C. Findler, M. Ramakrishnan, A. Bortis, L. Rettig, K. Shimamoto, E. M. Bothschafter, M. Porer, V. Esposito, Y. Hu, A. Alberca, T. Lippert, C. W. Schneider, U. Staub, and N. A. Spaldin. Relationship Between Crystal Structure and Multiferroic Orders in Orthorhombic Perovskite Manganites. *Physical Review Materials*, **2**(10) (2018). doi:10.1103/PhysRevMaterials.2.104414.

[154] H. Katsura, N. Nagaosa, and A. V. Balatsky. Spin Current and Magneto-electric Effect in Noncollinear Magnets. *Physical Review Letters*, **95**(5) (2005). doi:10.1103/PhysRevLett.95.057205.

[155] S. Dong, R. Yu, S. Yunoki, J.-M. Liu, and E. Dagotto. Origin of Multiferroic Spiral Spin Order in the $RMnO_3$ Perovskites. *Physical Review B*, **78**(15) (2008). doi:10.1103/PhysRevB.78.155121.

[156] M. Mochizuki, N. Furukawa, and N. Nagaosa. Theory of Spin-Phonon Coupling in Multiferroic Manganese Perovskites $RMnO_3$. *Physical Review B*, **84**(14) (2011). doi:10.1103/PhysRevB.84.144409.

[157] K. Shimamoto, Y. W. Windsor, Y. Hu, M. Ramakrishnan, A. Alberca, E. M. Bothschafter, L. Rettig, T. Lippert, U. Staub, and C. W. Schneider. Multiferroic Properties of Uniaxially Compressed Orthorhombic $HoMnO_3$ Thin Films. *Applied Physics Letters*, **108**(11):112904 (2016). doi:10.1063/1.4944460.

[158] R. Schleck, R. L. Moreira, H. Sakata, and R. P. S. M. Lobo. Infrared Reflectivity of the Phonon Spectra in Multiferroic $TbMnO_3$. *Physical Review B*, **82**(14) (2010). doi:10.1103/PhysRevB.82.144309.

[159] R. Vali. Vibrational, Dielectric and Scintillation Properties of $YAlO_3$. *Journal of Luminescence*, **127**(2):727–730 (2007). doi:10.1016/j.jlumin.2007.04.009.

[160] S. Matzen and S. Fusil. Domains and Domain Walls in Multiferroics. *Comptes Rendus Physique*, **16**(2):227–240 (2015). doi:10.1016/j.crhy.2015.01.013.

[161] Y. W. Windsor. Private communication (2018). Fritz Haber Institute of the Max Planck Society.

[162] K. J. Choi. Enhancement of Ferroelectricity in Strained $BaTiO_3$ Thin Films. *Science*, **306**(5698):1005–1009 (2004). doi:10.1126/science.1103218.

[163] D. Kan, R. Aso, H. Kurata, and Y. Shimakawa. Epitaxial Strain Effect in Tetragonal $SrRuO_3$ Thin Films. *Journal of Applied Physics*, **113**(17):173912 (2013). doi:10.1063/1.4803869.

[164] G. Ghosh. Dispersion-Equation Coefficients for the Refractive Index and Birefringence of Calcite and Quartz Crystals. *Optics Communications*, **163**(1-3):95–102 (1999). doi:10.1016/S0030-4018(99)00091-7.

[165] G. Ertl. Reactions at Surfaces: From Atoms to Complexity (Nobel Lecture). *Angewandte Chemie International Edition*, **47**(19):3524–3535 (2008). doi:10.1002/anie.200800480.

[166] C. Eggeling, C. Ringemann, R. Medda, G. Schwarzmann, K. Sandhoff, S. Polyakova, V. N. Belov, B. Hein, C. von Middendorff, A. Schönle, and S. W. Hell. Direct Observation of the Nanoscale Dynamics of Membrane Lipids in a Living Cell. *Nature*, **457**(7233):1159–1162 (2008). doi:10.1038/nature07596.

List of Acronyms

BBO	barium borate
C	commercial
CCD	charge-coupled device
DFPT	density functional pertubation theory
FEL	free-electron laser
FHI	Fritz Haber Institute
FIR	far-infrared
FO	fiber oscillator
FOM	figure of merit
FPSQ	four-parameter semiquantum
FTIR	Fourier-transform infrared
h-BN	hexagonal boron nitride
HWHM	half width at half maximum
IR	infrared
KRS-5	Thalliumbromidiodid
LD	low-density
LED	light-emitting diode
LHe	liquid helium
LO	longitudinal optical
LP	long-pass
MBE	molecular beam epitaxy
MCT	mercury cadmium telluride
MIR	mid-infrared
NIR	near-infrared
OTS	octadecyltrichlorosilane
PE	polyethylene
PID	proportional-integral-derivative
PMT	photomultiplier tube
SFG	sum-frequency generation
SHG	second-harmonic generation
SL	superlattice
SP	short-pass
SPhP	surface phonon polariton
SPP	surface plasmon polariton

STEM   scanning transmission electron microscope

TO   transversal optical

UHMW   ultrahigh molecular weight

XH   crystalline hybrid

XRD   x-ray diffraction

Publications

- Christopher J. Winta, Sandy Gewinner, Wieland Schöllkopf, Martin Wolf, Alexander Paarmann.
  Second-Harmonic Phonon Spectroscopy of α-Quartz.
  Phys. Rev. B, **97**:094108, 2018.
  DOI: 10.1103/PhysRevB.97.094108

- Ilya Razdolski, Nikolai C. Passler, Christopher R. Gubbin, Christopher J. Winta, Robert Cernansky, Francesco Martini, Alberto Politi, Stefan A. Maier, Martin Wolf, Alexander Paarmann, Simone De Liberato.
  Second Harmonic Generation from Strongly Coupled Localized and Propagating Phonon-Polariton Modes.
  Phys. Rev. B, **98**:125425, 2018.
  DOI: 10.1103/PhysRevB.98.125425

- Christopher J. Winta, Martin Wolf, Alexander Paarmann.
  Low-Temperature Dielectric Function of Hyperbolic α-Quartz.
  Phys. Rev. B, **99**:144308, 2019 (Editors' Suggestion).
  DOI: 10.1103/PhysRevB.99.144308

- Daniel C. Ratchford*, Christopher J. Winta*, Ioannis Chatzakis, Chase T. Ellis, Nikolai C. Passler, Jonathan Winterstein, Pratibha Dev, Ilya Razdolski, Joseph R. Matson, Joshua R. Nolen, Joseph G. Tischler, Igor Vurgaftman, Michael B. Katz, Neeraj Nepal, Matthew T. Hardy, Jordan A. Hachtel, Juan-Carlos Idrobo, Thomas L. Reinecke, Alexander J. Giles, D. Scott Katzer, Nabil D. Bassim, Rhonda M. Stroud, Martin Wolf, Alexander Paarmann, Joshua D. Caldwell.
  * These authors contributed equally to this work.
  Controlling the Infrared Dielectric Function Through Atomic-Scale Heterostructures.
  ACS Nano, **13**:6730–6741, 2019.
  DOI: 10.1021/acsnano.9b01275

Presentations

- *Seminar, group of Prof. Dr. Wolfgang Kuch*—Freie Universität, Berlin (Germany),
  June 22, 2020
  Invited talk: **Polar Semiconductor Heterostructures as Hyperbolic Metamaterials**.

- *DPG Spring Meeting 2020, Condensed Matter Section*—Dresden (Germany),
  March 15–20, 2020 (cancelled)
  Talk: **Polar Semiconductor Heterostructures as Hyperbolic Metamaterials**.

- *ITQW 2019*—Ojai, California (USA),
  September 15–20, 2019
  Extended talk: **Controlling the Infrared Dielectric Function through Atomic-Scale Heterostructures**.

- *Seminar, group of Prof. Dr. Wolfgang Kuch*—Freie Universität, Berlin (Germany),
  June 24, 2019
  Invited talk: **Low-Temperature Dielectric Function of Hyperbolic α-Quartz**.

- *DPG Spring Meeting 2019, Condensed Matter Section*—Regensburg (Germany),
  March 19–24, 2019
  Talk: **Low-Temperature Dielectric Ffunction of Hyperbolic α-Quartz**.

- *Seminar, group of Prof. Dr. Wolfgang Kuch*—Freie Universität, Berlin (Germany),
  May 29, 2018
  Invited talk: **Phase Transition Studies Using Second-Harmonic Phonon Spectroscopy**.

- *DPG Spring Meeting 2018, Condensed Matter Section*—Berlin (Germany),
  March 11–16, 2018
  Talk: **Phase Transition Studies Using Second-Harmonic Phonon Spectroscopy**.

- *FEL Workshop "Applications of IR Free-Electron Lasers: Latest Developments and Future Directions"*—Ringberg Castle, Kreuth (Germany),
  January 17–20, 2018
  Invited talk: **Atomic-scale Heterostructures Studied with Mid-IR Second-Harmonic Phonon Spectroscopy**.

- *IMF-2017*—San Antonio, Texas (USA),
  September 4–8, 2017
  Talk: **Second-Harmonic Phonon Spectroscopy of the Model Oxide α-Quartz**.

- *Seminar, group of Prof. Dr. Wolfgang Kuch*—Freie Universität, Berlin (Germany),
  April 25, 2017
  Invited talk: **Second-Harmonic Phonon Spectroscopy**.

- *DPG Spring Meeting 2017, Condensed Matter Section*—Dresden (Germany),
  March 19–24, 2017
  Talk: **AlN/GaN Multilayer Interface Phonons Studied with Mid-IR Second-Harmonic Phonon Spectroscopy**.

- *CLEO: QELS_Fundamental Science 2016*—San Jose, California (USA),
  June 5–10, 2016
  Talk: **Second Harmonic Phonon Spectroscopy of α-Quartz**.

- *DPG Spring Meeting 2016, Condensed Matter Section*—Regensburg (Germany),
  March 6–11, 2016
  Talk: **Second Harmonic Phonon Spectroscopy of α-Quartz**.

Acknowledgments

I want to thank the many people who took part in my scientific and/or personal life during the past years and thereby contributed to the development of this thesis in one way or another. Here, I would like to mention a few of them in particular.

First of all, I would like to thank *Martin Wolf* for supervising this work and providing me the opportunity to perform my PhD studies in his Department of Physical Chemistry at the Fritz Haber Institute—a very special place which I have always appreciated not only for its excellent science, but also for its collaborative spirit, and cordial atmosphere.

I also kindly thank *Wolfgang Kuch* from the Free University Berlin for taking over as the second supervisor and for keeping in friendly contact throughout the entire time.

Very importantly, I owe big thanks to *Alexander Paarmann* who, as the leader of the Lattice Dynamics Group, managed to create an immensely positive, open, and fruitful work environment. He has never hesitated to support me in my research efforts, may it be in the form helpful discussions, constructive feedback, or hands-on laboratory work. I am extremely grateful for that.

In this context, I also thank my current and former colleagues in the Lattice Dynamics Group: *Christian, Ilya, Riko, Nikolai, Marcel, Richarda,* and *Sören*. I have always enjoyed the sound combination of collegiality, productivity, and humor in the office. I am looking forward to many more frisbee sessions, piano lessons, and game nights in the future.

Furthermore, I have received a large amount of technical support in my PhD work. I want to greatly thank *Wieland Schöllkopf* and *Sandy Gewinner* for keeping the free-electron laser running (oftentimes late at night), *Sven Kubala* for helping me with the design and construction of various pieces of laboratory equipment, the FHI mechanical workshops, and the E-Lab.

For the the fruitful collaboration on the Crystalline Hybrids project I would like to thank the entire group around *Joshua Caldwell*.

Finally, my most profound gratitude goes to my *parents* for their endless love, support, and faith as well as to my beloved girlfriend *Janola*, for all her kindness, patience, and selflessness.

Declaration of Authorship

I declare to the Freie Universität Berlin that I have completed the submitted dissertation independently and without the use of sources and aids other than those indicated. The present thesis is free of plagiarism. I have marked as such all statements that are taken literally or in content from other writings. This dissertation has not been submitted in the same or similar form in any previous doctoral procedure. I agree to have my thesis examined by a plagiarism examination software.

Berlin, October 12, 2020

_____

Christopher J. Winta